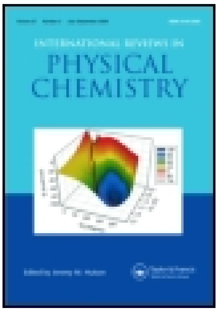

International Reviews in Physical Chemistry
Publication details, including instructions for authors and subscription information:
http://www.tandfonline.com/loi/trpc20

Ultrafast multiple-mode multiple-dimensional vibrational spectroscopy

Hailong Chen [a] , Hongtao Bian [a] , Jiebo Li [a] , Xiewen Wen [a] & Junrong Zheng [a]

[a] Department of Chemistry, Rice University, Houston, TX 77005

Version of record first published: 31 Oct 2012.

To cite this article: Hailong Chen, Hongtao Bian, Jiebo Li, Xiewen Wen & Junrong Zheng (2012): Ultrafast multiple-mode multiple-dimensional vibrational spectroscopy, International Reviews in Physical Chemistry, DOI:10.1080/0144235X.2012.733116

To link to this article: http://dx.doi.org/10.1080/0144235X.2012.733116

International Reviews in Physical Chemistry
2012, 1–97, iFirst

Taylor & Francis
Taylor & Francis Group

Ultrafast multiple-mode multiple-dimensional vibrational spectroscopy

Hailong Chen, Hongtao Bian, Jiebo Li, Xiewen Wen and Junrong Zheng*

Department of Chemistry, Rice University, Houston, TX 77005

(*Received 25 June 2012; final version received 23 August 2012*)

Ultrafast multiple-dimensional vibrational spectroscopy has been extensively applied to studies of molecular structures and dynamics in condensed phases. Along with the developments of new laser sources and new concepts, increasing improvements and applications of this technique have brought the understanding of molecular systems to a new level. In this review, we first briefly introduce the basic concepts, experimental setups and applications of the technique. The most recent progresses in applying vibrational energy transfers to determine intermolecular distances and vibrational couplings to determine three dimensional molecular conformations with our high power multiple-mode multiple-dimensional vibrational spectroscopy are then introduced in more details.

Keywords: multiple-dimensional vibrational spectroscopy; 2D infrared spectroscopy; vibrational energy transfer; ion clustering; mapping molecular conformations

Contents

PAGE
1. **Introduction** 3
2. **Theoretical basis** 3
  2.1. Understanding MDVS 3
  2.2. Nonlinear response function 6
    2.2.1. Density matrix and perturbative expansion 6
    2.2.2. Feynman diagram 10
  2.3. Experimental setup 12
    2.3.1. Numerical transformation methods 13
      2.3.1.1. Photon echo approach 13
      2.3.1.2. Pump/probe and pulse shaper approaches 17
    2.3.2. Instrumental transformation methods 18
      2.3.2.1. The etalon approach 20
      2.3.2.2. The ps/fs hybrid approach 21
  2.4. On the analysis of MDVS spectra 22
    2.4.1. Origins of diagonal and cross peaks 22
    2.4.2. Polarisation selective 2D IR data 35
      2.4.2.1. Anisotropy 35

---

*Corresponding author. Email: junrong@rice.edu

ISSN 0144–235X print/ISSN 1366–591X online

http://dx.doi.org/10.1080/0144235X.2012.733116
http://www.tandfonline.com

2.4.2.2. Molecular rotations and energy transfers 39
2.5. Applications of MDVS 40

3. Mode-specific intermolecular vibrational energy transfer 41
3.1. Phenyl selenocyanate and deuterated chloroform mixture 42
3.1.1. Basis of observing the energy transfer 43
3.1.2. Detailed analyses of 2D IR spectra 43
3.1.3. Kinetic analysis of energy transfer from CD to CN 46
3.2. An analytical equation for the intermolecular vibrational energy transfer 49
3.2.1 Derivation of the energy transfer rate equation 49
3.2.2. Experimental parameters for Equation (3.6) 51
3.3. The energy mismatch dependence of the vibrational energy transfer 52
3.3.1. Nonresonant energy transfer results 53
3.3.2. Resonant energy transfer results 54
3.3.3. Comparison between experimental and predicted values 56
3.4. The coupling strength dependence of energy transfer rates 57
3.4.1. The donor/acceptor number ratio dependence 57
3.4.2. The coupling strength dependence 59

4. Ion clustering in aqueous solution 61
4.1. Ion clustering in aqueous solutions probed with vibrational energy transfer 61
4.1.1. Vibrational energy exchange in a cluster 62
4.1.2. Location-energy-exchange kinetic model 64
4.1.3. Properties of ion clusters 65
4.1.4. Comparisons among aqueous solutions and crystals 68
4.2. Ion association in aqueous solutions 69
4.2.1. Vibrational energy dynamics of the KSCN/H2O (1/10) solution 70
4.2.2. Vibrational energy dynamics of the NH4SCN/H2O (1/10) solution 72
4.3. Ion/protein-building-block molecular interactions in aqueous solutions 74
4.3.1. Interactions between SCN^- and amino acids 75
4.3.2. Interactions between SCN^- and N-H group in the backbone 76

5. Molecular conformations probed with MDVS 78
5.1. Conformation of 1-cyanovinyl acetate in CCl_4 solution 79
5.1.1. Possible conformations 79
5.1.2. Cross angles between different vibrational modes 80
5.1.3. Translation from vibrational angles to molecular conformations 83
5.2. Molecular conformations and dynamics on surfaces of gold nanoparticles 85
5.2.1. Surface non-adiabatic electron/vibration coupling 86
5.2.2. Translation from vibrational angles to molecular conformations 88

6. Concluding remarks and perspectives 91

References 92

1. Introduction

Ultrafast multiple-dimensional vibrational spectroscopy (MDVS) is an ultrafast infrared (IR) analog of the multiple-dimensional nuclear magnetic resonance (NMR) that directly probes the structural degrees of freedom of molecules [1–37]. In a manner somewhat akin to the NMR, the MDVS technique involves an IR pulse sequence that induces and then probes the evolution of excitations (vibrations) of a molecular system. A critical difference between the MDVS and NMR methods is that the IR pulse sequence is sensitive to dynamics at a timescale of 6 to 10 orders of magnitude faster than NMR. Under developing for more than 10 years, the ultrafast MDVS techniques have begun to gain applications in determining reaction mechanisms [4,6,19], peptide and protein dynamics and structures [7,11,20,24,38–46], charge transfer [29,47], vibrational coupling and energy relaxations [27,48–51], water structures and dynamics [23,52–57], hydrogen bond kinetics and thermodynamics [3,14,32,34,58,59], and chemical transformations [33].

With the purpose to benefit more researchers in relative fields to gain a comprehensive understanding of this technology, the basic concepts, experimental setups and applications of the general MDVS technique are introduced in details throughout this review. The most recent progresses in applying vibrational energy transfers to determine intermolecular distances, and vibrational couplings to determine three dimensional molecular conformations with our high power multiple-mode multiple-dimensional vibrational spectroscopy are then introduced in more details. In this review, we use "multiple-dimensional vibrational spectroscopy" instead of "two-dimensional infrared spectroscopy (2D IR)" to describe the technique, because even for the common "2D IR" methods based on the 3rd order nonlinear optical response, the data are three dimensional: two dimensions in frequency and one dimension in time, if the signal intensity is not counted as another dimension.

2. Theoretical basis

Detailed knowledge about general nonlinear optics and optical spectroscopy has been described well in literature [16,60,61]. Excellent summaries of theoretical backgrounds for nonlinear vibrational spectroscopy can also be found [62,63]. Here only a brief discussion is provided to help readers go through the physical picture of the technology.

2.1. *Understanding MDVS*

In most modern chemical laboratories, linear (one dimension) infrared spectroscopy methods, e.g. FTIR, are among the most frequently used techniques for the molecular structure analysis. The infrared methods determine molecular structures through measuring vibration frequencies of the chemical bonds. In a typical one-dimensional infrared spectrum, the x-axis is the frequency axis, and the y-axis is the signal intensity axis. In principle, the molecular structural information from such a spectrum can be obtained from the peak frequencies and intensities, and the molecular dynamic information can be obtained from the peak lineshapes [64]. In reality, the ubiquitous Fermi resonances and inhomogeneous broadening have added many complexities into the interpretations of linear IR spectra in condensed phases [65]. Fermi resonances originate from the anharmonic nature of molecular vibrations. A combination band (a vibrational transition involving two or more normal modes excited simultaneously) or an overtone (a transition from the ground state to an excited state higher than the 1st excited state) of which the origin is generally unknown with a very small transition dipole moment (called "dark mode") can be anharmonically coupled to a normal mode of the same symmetry and a similar frequency (energy) with a much bigger transition dipole moment (called "bright mode"). The vibrational coupling results in two consequences: (1) the high frequency mode shifts to higher frequency and the low frequency mode shifts to lower frequency; (2) the dark mode gains intensity and the bright mode decreases in intensity. The Fermi resonances can not only significantly change vibrational frequencies, but also produce many additional peaks in FTIR spectra. The two factors leads to difficulties in assigning IR peaks. The inhomogeneous broadening typically broadens the vibrational peaks. It originates from the fact that in condensed phases, molecules measured are typically of large quantity and in different local environments because of different solvent configurations. Different local environments lead to different intermolecular interactions, resulting in different frequencies of the same vibrational mode. The frequency broadening caused by the environmental inhomogeneity can be comparable or even larger than the natural frequency width caused by the molecular motions (homogeneous broadening). It is therefore difficult to derive molecular dynamics in condensed phases from linear IR lineshapes if the amplitude of the inhomogeneous broadening is not known. These two problems can be circumvented by expanding the linear techniques into nonlinear multiple-dimensional methods, which will be introduced in the following.

In nature, many equilibrium or nonequilibrium molecular phenomena at room temperature occur at the time scales of femtosecond (fs, 10^{-15} second), picosencond (ps, 10^{-12} second) and sub nanosecond (ns, 10^{-9} second). For instances, water molecules rotate in room temperature liquids with a time constant $2\sim3$ ps [66]. The *trans*-*gauche* isomerisations of simple ethane derivatives rotating along the C-C single bond in room temperature liquids occur in tens of ps [33]. The formation and dissociation of hydrogen bonds also occur in the ps time scale [32,59]. The light induced molecular isomerisations in retina occurs within a few hundred fs to a few ps [67]. Heat transportations at the molecular level also occur in the time scales of fs to ps [68]. Traditional methods have various difficulties in capturing the structural evolutions of these fundamental molecular events. The ultrafast electronic spectroscopic methods are sufficiently fast to catch the dynamics but generally lack of sufficient structural resolutions. NMR methods have sufficient structural resolutions but are lack of temporal resolutions. The typical NMR pulse duration is microseconds, though some dynamics at the time scales of fs or ps can be semi-quantitatively analysed by the NMR methods with many assumptions [69]. Vibrational (IR and Raman) spectroscopic techniques find their unique fits in the studies of these structural dynamics. Both the temporal and structural resolutions of these methods are sufficiently high for this application: (1) One cycle of a typical molecular vibration, e.g. the CN stretch at 2000 cm^{-1}, is 17 fs. The 1st excited state vibrational lifetimes of many vibrational modes in condensed phases at room temperature are hundreds of fs to sub ns [70]. The time scales perfectly matches those of the chemical bond transformations and structural and energetic dynamics associated with the transformations. (2) The vibrational motions are the fluctuations of nuclear distances. One set of vibrational motions of a molecule correspond to one set of atomic coordinate (conformation) of the molecule. Therefore, the structural changes in a molecule can inevitably cause the frequencies of some vibrational modes, or the cross angles among some vibrational modes to change. Such vibrational frequency or cross angle changes can be used to characterise the molecular structural changes. In general, linear vibrational spectroscopic methods have difficulties in resolving these fast dynamic structures, not only because of the Fermi resonances and the inhomogeneous broadening mentioned above, but also because their light sources are continuous which are not time resolved. The ideal approach to monitor the structural dynamics would be to take the real time snapshots of the molecular structures with a temporal resolution faster than the dynamics. For example, if the structural changes of one system have one-to-one correspondence to the frequency changes of one specific mode, the structural evolution can then be determined by monitoring the frequency evolution of this mode. This type of experiments requires three observables: the original frequency of the mode before the structural changes, the frequency of the mode at the end of a delay time after the changes are initiated, and the delay time which is varied in experiments to obtain the time evolution of the frequency.

Most molecules in nature are polyatomic molecules. A nonlinear molecule with N atoms has 3N-6 (or 3N-5 for linear molecule) normal modes of vibrations. The vibrational frequency (0–1 transition) of each normal mode can be given by

$$\nu = \frac{1}{2\pi}\sqrt{\frac{k}{\mu}}, \tag{2.1}$$

with k is the force constant, and μ the reduced mass. Most of the vibrational modes in the condensed phases are not completely independent. They are coupled. In other words, the vibrational behavior, e.g. the vibrational frequency and excitation, of one mode in one molecule is affected by other modes in the same molecule or modes in other molecules nearby. The vibrational couplings are the major reason for vibrational energy to dissipate. Vibrational couplings and consequent energy transfers can be applied to determining molecular structures and distances. The couplings can be measured in a manner similar to the assumed experiment with two dimensions in frequency (the initial and final frequencies) and one dimension in time described above for the structural dynamics: one vibrational mode is excited resonantly at its 0–1 transition frequency (the initial frequency), after a time delay, the signal is detected at another frequency (the final frequency) corresponding to the 0–1 or 1–2 transition of another mode. The effect of the excitation of one mode on the vibration of another mode can be manifested in this way.

Ideas similar to the assumed experiments to determine structural dynamics and vibrational couplings described above by monitoring the vibrational frequency changes to investigate molecular structural and energetic properties have led to the developments of various ultrafast multiple-dimensional vibrational spectroscopic methods (MDVS). As discussed, a MDVS technique must be able to provide information about the two frequencies, and to resolve the signal with a sufficiently fast temporal resolution ($\sim$100 fs). The fast temporal resolution and precise delays are usually achieved by using fs or ps excitation and detection pulses with precise nanopositioners. The two frequencies are generally obtained by the numerical Fourier transformation of interferograms, e.g. the “echo” method with nanopositioners [8] and the pump/probe method with a pulse shaper [22], or the instrumental Fourier transformations, e.g. the etalon method [71] and the grating method [72]. Each approach to obtain frequency has its own advantages and disadvantages. In the following, more detailed discussions are provided.

2.2. *Nonlinear response function*

The first question about MDVS is how molecular properties are correlated to experimental signals so that the frequency and dynamic information can be obtained.

The signal of MDVS is from light/material interactions. According to the Maxwell equations, the material properties are reflected by the optical polarisation P induced by the electric fields of the lights. All electronic and nuclear motions and their relaxations show up in optical measurements through their effects on the optical polarisation. Therefore, the complete knowledge of the optical polarisation is sufficient to interpret any optical spectroscopic measurements [16,63]. In linear optical measurements, e.g. FTIR, the polarisation (P) depends linearly on the incident electric field:

$$P = \varepsilon_0 \chi^{(1)} \cdot E, \tag{2.2}$$

where ε_0 is the vacuum permittivity, and $\chi^{(1)}$ is the linear susceptibility. With the electric field intensity getting higher, the linear relation can be invalid because of nonlinear effects. To count for the nonlinear effects, the polarisation can be expanded by the powers of the electric field E:

$$\begin{aligned} P &= P^{(1)} + P^{(2)} + P^{(3)} + \cdots \\ &= \varepsilon_0(\chi^{(1)} \cdot E + \chi^{(2)} \cdot E \cdot E + \chi^{(3)} \cdot E \cdot E \cdot E + \cdots), \end{aligned} \tag{2.3}$$

where $P^{(n)}$ is the nth order nonlinear polarisation, and $\chi^{(n)}$ is the nth order nonlinear susceptibilities.

In practice, most bulk samples investigated are usually isotropic with the inversion symmetry, which means that even-order susceptibilities, e.g. $\chi^{(2)}$, vanish. Besides, in general, polarisations of higher orders require more intense electric fields to produce sufficiently intense signals, compared to those of lower orders. Therefore, $\chi^{(1)}$ and $\chi^{(3)}$ are the most common quantities obtained from optical experiments. The linear susceptibility is related to the linear absorption spectroscopy. All MDVS methods introduced in this review are based on the 3rd order nonlinear susceptibility.

2.2.1. *Density matrix and perturbative expansion*

Most vibrational modes of the functional groups of a polyatomic molecule are significantly more energetic than the thermal energy ($\sim$200 cm^{-1}) at room temperature. Therefore, according to the Boltzmann distribution, most molecules at room temperature are at the ground state $|\psi\rangle = |0\rangle$ of these modes. After interacting with the incident light, a small portion of these molecules can be excited to a new state, i.e. $|\psi\rangle = \sum_n c_n|n\rangle$. $|n\rangle$ is the nth vibrational state: $n=0$, ground state, $n=1$, 1st excited state, and so on. c_n is the coefficient of nth vibrational state. The polarisation can be given by the expectation value of the dipole operator μ:

$$P(t) = \langle\psi|\mu|\psi\rangle = \sum_{nm} c_n c_m^* \langle m|\mu|n\rangle = \sum_{nm} c_n c_m^* \mu_{mn}. \tag{2.4}$$

In condensed phases, in general we have to deal with statistical ensembles, rather than pure states. Therefore, the representation of wavefunction needs to be replaced by the density matrix. The density operator is defined as:

$$\rho = \sum_k P_k \cdot |\psi_k\rangle\langle\psi_k|, \tag{2.5}$$

where $P_k \geq 0$ denotes the probability of a system being in a pure state $|\psi_k\rangle = \sum_n c_{kn}|n\rangle$, and with the normalisation condition $\sum_k P_k = 1$.

Accordingly, Equation (2.4) can be rewritten as:

$$\begin{aligned} P(t) &= \sum_k P_k \cdot \langle\psi_k|\mu|\psi_k\rangle = \sum_k P_k \cdot \sum_{nm} c_{kn}c^*_{km}\mu_{mn} \\ &= \sum_{nm} \mu_{mn} \sum_k P_k c_{kn} c^*_{km} = \sum_{nm} \mu_{mn}\rho_{nm} \\ &= \mathrm{Tr}(\mu\rho), \end{aligned} \tag{2.6}$$

where Tr(A) denotes the trace of a matrix A, and ρ_{nm} is the element of the density matrix.

According to Equation (2.6), in order to examine the dynamic behavior of the macroscopic polarisation, all we need to do is to determine the time evolution of the density matrix of the system $\rho(t)$, because μ_{mn} is time independent. The main question is becoming how to resolve a time-dependent density matrix.

According to the Schrödinger equation:

$$\frac{\mathrm{d}}{\mathrm{d}t}|\psi\rangle = -\frac{i}{\hbar}H|\psi\rangle, \tag{2.7}$$

we can derive the so-called *Liouville–Von Neumann* equation:

$$\begin{aligned} \frac{\mathrm{d}}{\mathrm{d}t}\rho &= \frac{\mathrm{d}}{\mathrm{d}t}\sum_k P_k \cdot |\psi_k\rangle\langle\psi_k| \\ &= \sum_k P_k \cdot \left(-\frac{i}{\hbar}H|\psi_k\rangle\langle\psi_k| + \frac{i}{\hbar}|\psi_k\rangle\langle\psi_k|H\right) \\ &= -\frac{i}{\hbar}H\rho + \frac{i}{\hbar}\rho H = -\frac{i}{\hbar}[H,\rho], \end{aligned} \tag{2.8}$$

with the Hamiltonian approximately written as

$$H = H_0 + H'(t) = H_0 + E(t)\cdot\mu, \tag{2.9}$$

where H_0 is the system Hamiltonian, and $H'(t)$ denotes the interaction with an optical field $E(t)$.

In general, *Liouville–Von Neumann* equation is very difficult to solve since it contains the time-dependent coefficient $H'(t)$. Therefore, the perturbative expansion method is generally employed. Two concepts need to be introduced: 'time evolution operator' and 'interaction picture'.

Time Evolution Operator: The time evolution operator $U(t, t_0)$ is defined as:

$$|\psi(t)\rangle \equiv U(t, t_0)|\psi(t_0)\rangle. \tag{2.10}$$

After inserting it into Equation (2.7), we have

$$\frac{\mathrm{d}}{\mathrm{d}t}U(t,t_0) = -\frac{i}{\hbar}H \cdot U(t,t_0). \tag{2.11}$$

Interaction Picture: The wavefunction in the interaction picture is defined as:

$$\left|\psi(t)\right\rangle \equiv U_0(t,t_0)\left|\psi_I(t)\right\rangle, \tag{2.12}$$

with

$$U_0(t,t_0) = e^{-\frac{i}{\hbar}H_0\cdot(t-t_0)}, \tag{2.13}$$

which is the time evolution operator with respect to the time-independent system Hamiltonian. The subscript I denotes the interaction picture. In this picture, the wavefunction is divided into two parts: $U_0(t,t_0)$ is only related with the system Hamiltonian H_0, and $\left|\psi_I(t)\right\rangle$ is contributed by the weak perturbation $H'(t)$. By inserting Equation (2.12) into Equation (2.7), we get the Schrödinger equation in the interaction picture:

$$\frac{\mathrm{d}}{\mathrm{d}t}\left|\psi_I(t)\right\rangle = -\frac{i}{\hbar}H'_I(t)\left|\psi_I(t)\right\rangle, \tag{2.14}$$

where the weak perturbation $H'_I(t)$ is defined as:

$$\begin{aligned} H'_I(t) &= U_o^{\dagger}H'(t)U_0(t,t_0) \\ &= e^{\frac{i}{\hbar}H_0(t-t_0)}H'(t)e^{-\frac{i}{\hbar}H_0(t-t_0)}. \end{aligned} \tag{2.15}$$

Accordingly, we can also obtain the density matrix in the interaction picture:

$$\rho(t) = U_0(t,t_0)\cdot\rho_I(t)\cdot U_0^{\dagger}(t,t_0), \tag{2.16}$$

as well as the *Liouville–Von Neumann* equation:

$$\frac{\mathrm{d}}{\mathrm{d}t}\rho_I(t) = -\frac{i}{\hbar}\left[H'_I(t),\rho_I(t)\right]. \tag{2.17}$$

The perturbative expansion is an effective means to resolve the density matrix from the *Liouville–Von Neumann* equation. We can integrate Equation (2.17), and obtain

$$\rho_I(t) = \rho_I(t_0) - \frac{i}{\hbar}\int_{t_0}^{t}\mathrm{d}\tau\left[H'_I(\tau),\rho_I(\tau)\right]. \tag{2.18}$$

By repeating this process, we can get

$$\begin{aligned} \rho_I(t) = \rho_I(t_0) + \sum_{n=1}^{\infty}\left(-\frac{i}{\hbar}\right)^n \int_{t_0}^{t}\mathrm{d}\tau_n\int_{t_0}^{\tau_n}\mathrm{d}\tau_{n-1}\cdots\int_{t_0}^{\tau_2}\mathrm{d}\tau_1 \\ \times\left[H'_I(\tau_n),[H'_I(\tau_{n-1}),\ldots[H'_I(\tau_1),\rho_I(t_0)]\ldots]\right]. \end{aligned} \tag{2.19}$$

Inserting this result into Equation (2.16), we have

$$\begin{aligned}\rho(t) &= \rho^{(0)}(t) + \sum_{n=1}^{\infty} \rho^{(n)}(t) \\ &= \rho^{(0)}(t) + \sum_{n=1}^{\infty} \left(-\frac{i}{\hbar}\right)^{n} \int_{t_0}^{t} \mathrm{d}\tau_n \int_{t_0}^{\tau_n} \mathrm{d}\tau_{n-1} \cdots \int_{t_0}^{\tau_2} \mathrm{d}\tau_1 \\ &\quad \times U_0(t,t_0) \cdot [H_I'(\tau_n), [H_I'(\tau_{n-1}), \ldots [H_I'(\tau_1), \rho(t_0)] \ldots]] \cdot U_0^{\dagger}(t,t_0), \end{aligned} \tag{2.20}$$

where $\rho^{(n)}(t)$ is the nth order density matrix.

Substituting $H'(t) = E(t)\cdot\mu$ into Equation (2.20), and setting $t_0 \to -\infty$ when no interaction has happened, we have

$$\begin{aligned}\rho^{(n)}(t) &= \left(-\frac{i}{\hbar}\right)^{(n)} \int_{-\infty}^{t} \mathrm{d}\tau_n \int_{-\infty}^{\tau_n} \mathrm{d}\tau_{n-1} \cdots \int_{-\infty}^{\tau_2} \mathrm{d}\tau_1 E(\tau_n)E(\tau_{n-1}) \cdot \ldots \cdot E(\tau_1) \\ &\quad \cdot U_0(t,t_0) \cdot [\mu_I(\tau_n), [\mu_I(\tau_{n-1}), \ldots [\mu_I(\tau_1), \rho(-\infty)] \ldots]] \cdot U_0^{\dagger}(t,t_0), \end{aligned} \tag{2.21}$$

with the dipole operator in the interaction picture:

$$\mu_I(t) = U_0^{\dagger}(t,t_0)\mu U_0(t,t_0). \tag{2.22}$$

Comparing Equation (2.20) with (2.3) and (2.6), we finally get the nth order polarisation:

$$P^{n}(t) = \langle \mu\rho^{(n)}(t)\rangle \tag{2.23}$$

In general, the perturbation $H_I'(t)$ caused by the external electric field ($10^{11} \sim 10^{16}\,\mathrm{W/cm^2}$) of even very intense lasers is usually very weak compared to the system Hamiltonian H_0 of the atomic internal field ($> 10^{17}\,\mathrm{W/cm^2}$). Therefore, in most cases, the perturbation theory works well in processing nonlinear optical spectroscopic results. According to Equation (2.21), the ratio of a higher order matrix (e.g. 5th) over a lower order (e.g. 3th) matrix approximately equals $(\mu Et/\hbar)^2$. Under most nonlinear vibrational spectroscopic experimental conditions, this value is significantly smaller than 1. Therefore, density matrices of higher orders are in general smaller than those of lower orders. Accordingly, polarisations of lower orders are stronger. However, it is worth nothing that when the external electric field is sufficiently strong, the light/matter interaction time is sufficiently long, and the transition dipole moment is sufficiently strong, e.g. those of the carbonyl stretches of metal carbonyl compounds, the higher order nonlinear signal can be very intense [73–76].

As discussed above, the 2nd order response is zero for central symmetric samples which most bulk samples are. Therefore, the lowest nonlinear response for most bulk samples is of the 3rd order. Responses of higher orders, e.g. 4th and 5th, are only occasionally applied to samples with large transition dipole moments [5,77,78]. Most MDVS methods discussed in this work is based on the 3rd order polarisation:

$$\begin{aligned}P^{3}(t) &= \left(-\frac{i}{\hbar}\right)^{3} \int_{-\infty}^{t} \mathrm{d}\tau_3 \int_{-\infty}^{\tau_3} \mathrm{d}\tau_3 \int_{-\infty}^{\tau_2} \mathrm{d}\tau_1 E(\tau_3)E(\tau_2)E(\tau_1) \\ &\quad \cdot \langle \mu_I(t) \cdot [\mu(\tau_3), [\mu(\tau_2), [\mu(\tau_1), \rho(-\infty)]]]\rangle \\ &= \left(-\frac{i}{\hbar}\right)^{(3)} \int_{0}^{\infty} \mathrm{d}t_3 \int_{0}^{\infty} \mathrm{d}t_2 \int_{0}^{\infty} \mathrm{d}t_1 E(t-t_3)E(t-t_3-t_2)E(t-t_3-t_2-t_1) \\ &\quad \cdot \langle \mu(t_3+t_2+t_1)[\mu(t_2+t_1), [\mu(t_1), [\mu(0), \rho(-\infty)]]]\rangle, \end{aligned} \tag{2.24}$$

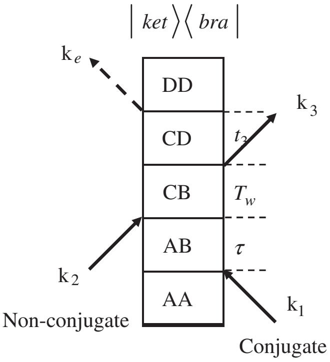

Figure 2.1. A Feynman diagram for a 3rd order interaction under the phase match condition $k_e = -k_1 + k_2 + k_3$. The system starts from the ρ_{AA} state and ends at the ρ_{DD}. k_1 and k_e are conjugate fields, while k_2 and k_3 are non-conjugate fields. The energy of states B and C must be higher than states A and D, in order to be fully resonant. (Practically, a signal emits immediately after the 3rd interaction. The above diagram is for an ideal case).

where we have changed the time variables in the second step, and

$$S^{(3)}(t_3, t_2, t_1) = \left(-\frac{i}{\hbar}\right)^{(3)} \langle \mu(t_3 + t_2 + t_1)[\mu(t_2 + t_1), [\mu(t_1), [\mu(0), \rho(-\infty)]]] \rangle \tag{2.25}$$

is called the 3th order nonlinear response function:

2.2.2. *Feynman diagram*

Equation (2.24) takes into account all possible types and time-orderings of interactions between the system and radiation fields. For the 3rd order experiments described later, expanding the nested commutator in Equation (2.24) leads to 48 terms, since each interaction can operate to the left or right (i.e. operate on the bra or ket) giving a factor of $2^3 = 8$, and there are $3! = 6$ ways to time-order the field interactions. However, for any given experiment, most of these terms are negligibly small and can be ignored, because they either have the incorrect time ordering of the field interactions, can't meet the phase matching condition preset in the experiment, or involve at least one nonresonant field interaction. It is therefore necessary to have a method of quickly identifying the important terms in Equation (2.24) which contribute to the experimental signal, and deriving expressions for them.

Feynman diagrams are commonly used for this purpose. In a Feynman diagram (shown in Figure 2.1), two vertical lines are used to represent the evolution of the system's density matrix elements in time. Time progresses upwards along the vertical lines. The left vertical line records the $|ket\rangle$ state of the system, and the right vertical line records the $\langle bra|$ state of the system. The $|ket\rangle$ and $\langle bra|$ states are written between the vertical lines. The n applied fields are represented as n straight arrows that slant upwards either to the left or right, and point either into or out of the outsides of the vertical lines, depending on the phase match condition. The point where an arrow intersects with the vertical line is a system-field interaction. An arrow that slants upwards to the right is considered to be a non-conjugate electric field, $\vec{E}_A(r,t) = \xi_A(t)\exp[ik_A \cdot r - i\omega_A t]$ and an arrow that slants upwards to the left is considered to be a conjugate electric field, $\vec{E}^*_A(r,t) = \xi^*_A(t)\exp[-ik_A \cdot r + i\omega_A t]$, with k_A, ω_A are the wave vector and the angular frequency of the electric field, respectively, and the function $\xi_A(t)$ is the envelope function of the applied field A and describes its time dependence. In addition to the n arrows representing the applied fields, a final dotted arrow represents the trace over $\rho^{(n)}(t)$ with the dipole operator μ. The initial and final states of the density matrix in each diagram must be diagonal. Following a field interaction, the density matrix element $|A\rangle\langle B|$ has a coherence frequency defined as

$$\omega_{AB} = \frac{E_A - E_B}{\hbar}. \tag{2.26}$$

Diagonal (population) states have zero frequency.

For a typical resonant experiment using pulsed fields, three constraints are applied to eliminate negligible terms and identify important contributions to the nonlinear polarisation. First, the phase-matching condition states that the sum over all applied wave vectors is equal to the wave vector of the induced polarisation, dictated by the momentum conservation principle. The momentum of a photon is proportional to the corresponding wave vector, i.e. $p = \hbar k$. The direction of a wave vector is the direction of light propagation, and its amplitude is proportional to the frequency of the light. This implies that signals with different phase-matching conditions will propagate in different directions, and only signals from those Feynman diagrams that have the required phase matching condition will be detected in a given direction. Selecting a phase-matching condition forces each applied field to slant only to either the right or left. For example, selecting the phase matching condition $k_e = -k_1 + k_2 + k_3$ restricts the relevant Feynman diagrams to only those that have k_1 slanting to the left, and k_2 and k_3 slanting to the right.

The second constraint on the number of relevant Feynman diagrams is the time-ordering of the interactions. In pulsed experiments, the time-ordering of interactions between the system and applied fields is under experimental control. If pulse 1 is experimentally set to arrive at the sample earlier in time than pulse 2, then any diagrams in which pulse 2 precedes pulse 1 can be ignored.

The final constraint on the number of relevant diagrams is the rotating wave approximation, namely, that a transition couples strongly to an applied field only when the transition and optical field have the same sense of rotation. The rotating wave approximation requires that all interactions must be resonant in order for the diagram to contribute strongly. In a Feynman diagram, the rotating wave approximation requires an arrow that points into it to couple a state of lower energy to higher energy, i.e. light is absorbed, and an arrow that points out of it to couple a state of higher energy to a state of lower energy, i.e. light is emitted. Any diagrams containing nonresonant interactions, i.e. absorbing from a higher state to a lower state or emitting from a lower state to a higher state, can be ignored. The constraints will be demonstrated in the following data analysis.

Once the relevant Feynman diagrams have been identified, expressions for the appropriate terms in Equation (2.24) can be straightforwardly derived [16]. However, it is important to note that the exact form of the expressions for the response of the optical polarisation will depend on details of the model for the system-bath interaction.

The 3$^{\text{rd}}$ order polarisation $P^{(3)}$ in Equation (2.24) can be typically rewritten as

$$P^{(3)}(\tau, T_w, t_3) \propto \int_0^\infty \mathrm{d}t_{3'} \int_0^\infty \mathrm{d}t_2 \int_0^\infty \mathrm{d}t_1 \left(\sum_i R_i(t_{3'}, t_2, t_1) \right) \times E_3(\tau + T_w + t_3 - t_{3'}) \cdot E_2(\tau + T_w + t_3 - t_{3'} - t_2) \cdot E_1(\tau + T_w + t_3 - t_{3'} - t_2 - t_1), \tag{2.27}$$

where

$$R_i \propto (-1)^n \cdot \mu_{AB} \times \mu_{AC} \times \mu_{BD} \times \mu_{CD} \times e^{\pm i\omega_1 \tau} \cdot e^{\pm i\omega_3 t_3} \cdot \Gamma(\tau, T_w, t_3) \cdot \exp[g(\tau, T_w, t_3)] \tag{2.28}$$

is the material nonlinear response function. n is the number of arrows on either side of the diagram. -1 represents that the signal is from absorption, and 1 represents that the signal is from either bleaching or stimulated emission. Experimental data to illustrate the principles will be discussed in Section 2.4. ω_1 and ω_3 are the frequencies of coherences during τ and t_3 periods, respectively, and their signs depend on detailed Feynman diagrams. If B and C are not the same states, which means the intermediate state BC during the T_w time is a not population state but a coherence state. In this case, an addition term $e^{\pm i\omega_2 T_w}$ should be multiplied to the right side of Equation (2.28), where $\omega_2 = \omega_B - \omega_C$ is the frequency of coherences during T_w periods. $\Gamma(\tau, T_w, t_3)$ is a time-damping factor whose details depend on the kinetic models. $g(t)$ is a line-broadening function, and μ_{IJ} is the transition dipole moment of a transition in Figure 2.1. In Equation (2.27), each response function corresponds to one Feynman diagram. Therefore, finding right Feynman diagrams is the core issue in analyzing MDVS spectra.

If vibrational coherences (AB or CD in Figure 2.1) can transfer, the Feynman diagram analysis method will break because coherence transfers produce too many possible diagrams. Luckily, if vibrational coherences do transfer, it seems that their contributions to the overall MDVS signal are not very significant [27,48,79,80]. One possible reason is that coherence transfers require energy exchange with the environment to fill the energy mismatch between the coherences, while the interaction with a thermal bath is typically to randomise the phase of coherences. In the following analysis, coherence transfers are not considered.

In summary, this section finally comes down to the response functions, which the experimental MDVS signals are from. As we can see from Equation (2.28), a response function contains information about two frequencies: ω_1 (initial) and ω_3 (final), and the dynamics: $\Gamma(\tau, T_w, t_3)$. Now the next issue is how to experimentally obtain these three types of information to decipher molecular structures and dynamics.

2.3. *Experimental setup*

As discussed above, most MDVS techniques are based on the 3rd order nonlinear optical polarisation. The only difference is how to obtain the two frequencies involved in Equation (2.28), i.e., ω_1 and ω_3, which we have already introduced at the beginning of this chapter. In general, there are two methods to resolve the frequency of an electric field via Fourier transform: one is the instrumental method, i.e., by using some dispersing elements (e.g. grating or etalon), the light can be extracted at any specific frequency; the other method is the numerical Fourier transform, i.e., by scanning the signal at various time delays between two adjacent pulses, one can get time dependent coherent patterns

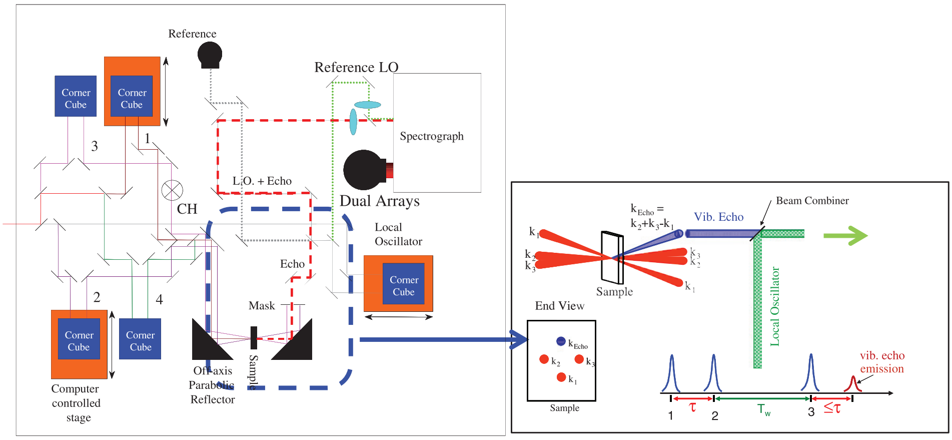

Figure 2.2. (Colour online) The schematic diagram of the photon echo 2D IR experimental setup. The input infrared light was initially divided into 5 parts by four beamsplitters. Beams 1, 2 and 3 were successively applied to the sample and generated the vibrational echo or free induction decay signal. Beam 4 served as the tracer beam, which was preset to follow the signal direction and used to trace and properly align the signal to combine with the local oscillator beam [83].

(interferograms), and then the signal at different frequencies can be extracted by the numerical Fourier transformation of the coherent patterns. Both methods are widely used in the MDVS techniques. For the probe frequency ω_3, it is usually obtained through the instrumental method (using a grating). There are two main reasons for the choice: (1) saving data acquisition time. A typical MDVS experiment only needs information within the band width of tens of cm^{-1}. Lights in this band width resolved by a grating can be simultaneously detected by an array detector at one laser shot ($\sim 10^{-3}$ second). The numerical method takes long time to obtain an interferogram (~1 minute). (2) Free of phase errors. The instrumental method is phase-locked. It does not produce phase errors that generally occur in the numerical method where the experimental time uncertainty is converted into the phase uncertainty during the numerical transformation (Details see below). For the excitational frequency ω_1, either method can be used, with respective advantages and disadvantages. In the following, two types of MDVS experimental setups based on different transformation methods to obtain ω_1 are introduced.

2.3.1. *Numerical transformation methods*

2.3.1.1. *Photon echo approach*. From the so called "photon echo" experiments, ω_1 is obtained by the numerical transformation method, and ω_3 is resolved by a grating [8,15,31]. Both the frequency and temporal resolutions of this method are very high: (1) the frequency resolution can be better than 2 cm^{-1}, and (2) the temporal resolution can be faster than 50 fs. However, several disadvantages are also associated with this approach. It is generally quite time consuming to obtain the interferograms for ω_1. In addition, the experimental setup is very complicated, and generally requires experts to operate. Data processing to remove the phase errors induced by the time errors in the experiments is also nontrivial.

The experimental setup of the photon echo approach [81,82] is sketched in Figure 2.2. The light source of the experiment typically includes three major components: (1) a

Ti:Sapphire oscillator which generates laser pulses centered at ~800 nm with a band width 10~50 nm and a repetition rate of ~80 MHz; (2) A Ti:Sapphire regenerative amplifier which amplifies the pulses from the oscillator to generate lasers centered at ~800 nm with a pulse duration 30~150 fs, a repetition rate of 1 KHz and output power 0.5~4 W; and (3) an optical parametric amplifier (OPA) system to convert the 800 nm light from the amplifier into Mid-IR pulses. The IR pulses from the OPA can span sufficient bandwidth (300 cm^{-1}) with tunable central wavelength from 3 to 22 μm. In the echo experiments, the infrared light was divided into 5 beams. Three of them were successively applied to induce the subsequent emission in a distinct direction of a time delayed 4th pulse, the vibrational echo from the phase match direction $k_e = -k_1 + k_2 + k_3$ or the free induction decay from $k_n = k_1 - k_2 + k_3$. The signal pulse is traced and properly aligned with the aid of a fourth beam which was preset to follow the signal direction. The aligned signal was then detected with frequency and phase resolution by combining it with a 5th beam, the local oscillator, and the combined pulses are dispersed in a spectrograph. The detection method with a local oscillator is called "heterodyne detection". The function of the local oscillator is to phase resolve and amplify the vibrational echo signal. Data are thus obtained as a function of three variables: the emitted signal frequencies ω_3, and the variable time delays between the first and second pulses (τ), and second and third pulses (T_w, the variable "waiting" time). By numerical Fourier transform, the τ scan data taken at every ω_3 are mapped to a second frequency variable ω_1 for each T_w. The echo and free induction decay data are then summed together with proper phase correlations to remove most of the dispersion contribution [9,82]. The data are then plotted in three dimensions, the signal amplitude as a function of both ω_1 and ω_3, which correspond to the ω_1 and ω_3 axes, respectively in 2D NMR.

The experimental detected signal I_s can be expressed as

$$\begin{aligned} I_s &= |\mathbf{E}_{LO} + \mathbf{S}|^2 = |\mathbf{E}_{LO}|^2 + 2\mathrm{Re}\left[\mathbf{E}_{LO}^* \cdot \mathbf{S}_{echo}\right] + |\mathbf{S}|^2 \\ &= |\mathbf{E}_{LO}|^2 + 2|\mathbf{E}_{LO}| \cdot |\mathbf{S}| \cdot \cos(\omega_1 \tau) \cdot \cos(\omega_3 t_3) + |\mathbf{S}|^2, \end{aligned} \tag{2.29}$$

where $\mathbf{E}_{LO}$ and $\mathbf{S}$ are the electric fields of the local oscillator and the signal, respectively. Re represents the real part. $\mathbf{E}_{LO}$ is experimentally adjusted to be much bigger than $\mathbf{S}$, so that $|\mathbf{S}|^2$ is too smaller to be important compared to the other two terms at the right side of Equation (2.29). $|\mathbf{E}_{LO}|^2$ is a constant which is removed by the chopping method through which signals between excitation on and off are subtracted with a chopper in experiments. Therefore, only the cross term matters. It contains all useful information we need: two frequencies ω_1 and ω_3, and the time dependent signal amplitude $|\mathbf{S}|$. The next step is to process the signal to obtain the two frequency values.

The Fourier transformation of the time domain signal I_s (Figure 2.3(A)) into signal in one-dimensional frequency results in a complex number (Figure 2.3(B)). The real part of the number is the absorptive spectrum, the red peak in Figure 2.3(B), and the imaginary part is the dispersive spectrum, the blue peak [62]. The absorptive spectrum has a much better frequency resolution, which is generally more desirable than the dispersive spectrum. In the transformations of signal into data in two-dimensional frequencies, in which the signal is first transformed for one dimension frequency and the resulted data are then transformed again to obtain the other dimension frequency, the final result of the twice transformation is still a complex number. However, both the real and imaginary part

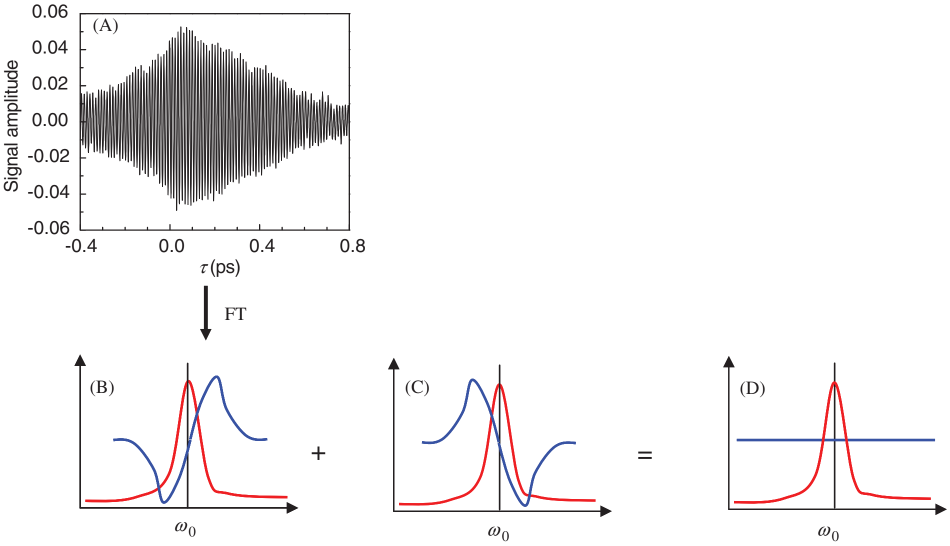

Figure 2.3. (Colour online) The schematic diagram of how to remove the dispersive contributions by summing signals from two phase matched directions together. The red peaks represent the absorptive spectra, and the blue peaks represent the dispersive spectra. The interferrogram in (A) is signal scanned along τ and detected by an element of an array detector. Each element of the array detector represents each ω_3 frequency. Fourier transformation of data in (A) results in a complex number with a real part (red line in (B)) and an imaginary number (blue line in (B)).

of this number contain both real and dispersive contributions from the twice transformations, as shown in Equation (2.31).

For an experiment with a preset phase match direction, e.g. the so called "photon echo" or "rephasing" direction $k_e = -k_1 + k_2 + k_3$, the signal can be rewritten as (see Equation (2.28))

$$S_e(\tau, T_w, t_3) \propto A \times B(\tau, T_w, t_3) \times e^{i\omega_1\tau} \times e^{-i\omega_3 t_3}. \tag{2.30}$$

Transforming the signal twice, we have

$$\begin{aligned} S_e(\omega_1, \omega_3, T_w) &= \int_0^\infty \mathrm{d}\tau \int_0^\infty \mathrm{d}t_3 e^{i\omega_3 t_3 - i\omega_1\tau} \times S_e(\tau, T_w, t_3) \\ &= [R(\omega_1) - I(\omega_1)i] \times [R(\omega_3) + I(\omega_3)i] \\ &= [R(\omega_1)R(\omega_3) + I(\omega_1)I(\omega_3)] \\ &\quad - i[I(\omega_1)R(\omega_3) - R(\omega_1)I(\omega_3)], \end{aligned} \tag{2.31}$$

where R and I represent the real and imaginary parts resulted from the Fourier transformations, respectively. According to Equation (2.31), transformations of the signal from this single phase match direction into two dimensional frequencies lead to a superposition of both absorptive and dispersive contributions. As a result, the spectrum from such a superposition has a low frequency resolution and a distorted line shape [15]. Now, let's examine the signal from another phase matched direction, the "nonrephasing" direction $k_n = k_1 - k_2 + k_3$. Following the same mathematical procedure as Equations (2.30 and 3.1), we get

$$S_n(\tau, T_w, t_3) \propto A \times B(\tau, T_w, t_3) \times e^{-i\omega_1\tau} \times e^{-i\omega_3 t_3}, \tag{2.32}$$

and

$$\begin{aligned} S_n(\omega_1, \omega_3, T_w) &= \int_0^\infty \mathrm{d}\tau \int_0^\infty \mathrm{d}t_3 \exp(i\omega_3 t_3 + i\omega_1\tau) \times S_n(\tau, T_w, t_3) \\ &= [R(\omega_1) + I(\omega_1)i] \times [R(\omega_3) + I(\omega_3)i] \\ &= [R(\omega_1)R(\omega_3) - I(\omega_1)I(\omega_3)] + i[I(\omega_1)R(\omega_3) + R(\omega_1)I(\omega_3)]. \end{aligned} \tag{2.33}$$

The real parts of Equations (2.31 and 3.3) are similar, except the opposite signs of the $I(\omega_1)I(\omega_3)$ term. If they are summed together, the result is

$$\mathrm{Re}(S_n(\omega_1, \omega_3, T_w)) + \mathrm{Re}(S_e(\omega_1, \omega_3, T_w)) = 2R(\omega_1)R(\omega_3), \tag{2.34}$$

where the dispersive contribution, $I(\omega_1)I(\omega_3)$, is removed. Only the purely absorptive contribution $R(\omega_1)R(\omega_3)$ is left. This method of eliminating dispersive components is depicted in Figure 2.3, which was developed gradually from 2D NMR, 2D visible spectroscopy and then to the 2D IR spectroscopy [9,69,84].

However, it is important to note that there is an assumption used in Equation (2.34): signals from both phase match conditions have an equal contribution, which is generally not true in experiment. In fact, the rephasing signal is always a little more intense than that of the nonrephasing signal. As a result, an adjustable amplitude parameter was always required to compensate this difference in the final data processing.

The result in Equation (2.34) is for the ideal case. In reality, due to the existence of many experimental uncertain factors, the time delays τ and t_3 cannot be determined 100% accurately, and the IR pulses are not perfectly at the transform limit. According to the time shift theorem [69], the uncertainty in time will inevitably lead to an uncertainty of the phase during the Fourier transform, i.e.:

$$FT\{S(\tau - \Delta_\tau, t_3 - \Delta_{t_3})\} = e^{-i\omega_1\Delta_\tau - i\omega_3\Delta_{t_3}} S(\omega_1, T_w, \omega_3), \tag{2.35}$$

and hence results in an distorted 2D spectrum. To solve this problem, the 2D spectrum obtained after the Fourier transform is assumed to have the following form:

$$\begin{aligned} S_{2D}(\omega_1, T_w, \omega_3) = \mathrm{Re}(&C \times S_n(\omega_1, T_w, \omega_3) \times e^{i\omega_1\Delta_{n\tau} + i\omega_3\Delta_n t_3 + i\omega_1\omega_3\Delta_{2n} + \cdots}) \\ &+ \mathrm{Re}(S_e(\omega_1, T_w, \omega_3) \times e^{i\omega_1\Delta_{e\tau} + i\omega_3\Delta_e t_3 + i\omega_1\omega_3\Delta_{2e} + \cdots}), \end{aligned} \tag{2.36}$$

with $C, \Delta_{n\tau}, \Delta_{nt3}, \Delta_{2n}, \Delta_{e\tau}, \Delta_{et3}, \Delta_{2e}, \ldots$ are adjustable parameters. More specifically, the subscripts e and n represent rephasing signal (i.e. echo signal) and nonrephasing signal, respectively. C is a parameter to compensate for the amplitude difference between the two phase match conditions, $\Delta_{n\tau}, \Delta_{nt3}, \Delta_{e\tau}, \Delta_{et3}$ are time parameters used to correct the experimental time-uncertainties. Δ_{2n}, Δ_{2e} are high order time correction terms. In experiments, the value of C can be determined by the intensity ratio of the rephasing signal and the nonrephasing signal. The following correlations, $\Delta_{n\tau} = -\Delta_{e\tau}$, $\Delta_{nt3} = \Delta_{et3}, \Delta_{2n} = \Delta_{2e}$, can be further set based on experimental conditions. Hence, to obtain a relatively phase-corrected 2D spectrum, there were only three necessary adjustable parameters. Two criterions can be used to find these parameters. One is based on the fact that a corrected 2D absorption peak must have the same symmetries with the one in the corresponding 1D absorption spectrum, while incorrect parameters will result in an unsymmetrical line shape. The other criterion is based on the projection theorem [84], e.g.:

$$\int S_{2D}(\omega_1, T_w, \omega_3)\mathrm{d}\omega_1 = S_{pp}(T_w, \omega_3), \tag{2.37}$$

where $S_{pp}(T_w, \omega_3)$ is the signal acquired from a broadband pump/probe measurement with exactly the same experimental environment. This is because the pump/probe signal is actually a combination of the two kinds of phase matching signal, which will be discussed later. By choosing appropriate parameters, a 2D spectrum with most dispersive contribution removed can be finally obtained through the procedure described.

2.3.1.2. *Pump/probe and pulse shaper approaches.* As discussed above, the numerical transformation method based on the photon echo approach has several major disadvantages: (1) it is time consuming to collect interferograms from each phase match direction; (2) the relative timing of the rephasing and nonrephasing coherence signals and the absolute τ and t_3 timings can have relatively big uncertainties (a few fs to tens of fs) and these uncertainties can be fluctuating during the experiments; (3) experimentally it is very difficult to operate and maintain such a system with five invisible beams which must have perfect temporal and spatial overlaps. To address these problems, two different approaches based on the pump/probe scheme were adopted [22,85–89]. In these two new approaches, only two laser beams interact with the samples, extremely simplifying the experimental operation. It is worth noting that, the physical nature of these two approaches is almost the same as that of the photon echo approach. All of these need to collect the τ-dependent coherent patterns, and the signal at different frequencies (ω_1) can be extracted by the numerical Fourier transformation of the coherent patterns as discussed above.

One approach is to use the crossed-beam geometry between a collinear pulse-pair pump and a probe beam, as shown in Figure 2.4 [85]. In brief, the IR source was first split into three beams by beam splitters, and then the beams 1 and 2 were combined by another beam splitter to create the pulse-pair collinear pump (E_1&E_2). The relative time delay τ between the pulse-pair (E_1&E_2) can be controlled by a delay line, e.g. through the translation of ZnSe wedge pairs. Beam 3 is the 3rd excitation pulse and the local oscillator (E_3&E_{LO}). In the pump/probe geometry, E_1&E_2 are collinear and both are included in the pump beam, and E_3&E_{LO} are collinear and both are included in the probe beam. The 3rd order signals from both rephasing and nonrephasing directions are collinear with the probe beam direction, because either $k_n = k_1 - k_2 + k_3$ or $k_e = -k_1 + k_2 + k_3$ results in the same direction $\vec{k}_e = \vec{k}_n = \vec{k}_3$. Therefore, scanning τ once can automatically obtain signals from both phase match directions, different from the echo method that both directions have to be scanned one by one. In addition, because E_3&E_{LO} are essentially the same pulse, the time difference between them is locked, which simplifies the data phasing procedure. Compared to the echo method, experiments through this approach are much easier to handle. Data acquisition is also faster. However, as can be seen from Figure 2.4, at least 50% of the excitation energy is wastes at the beam combiner. In addition, because E_3&E_{LO} are the same pulse, the relative amplitude of E_3&E_{LO} cannot be adjusted as what

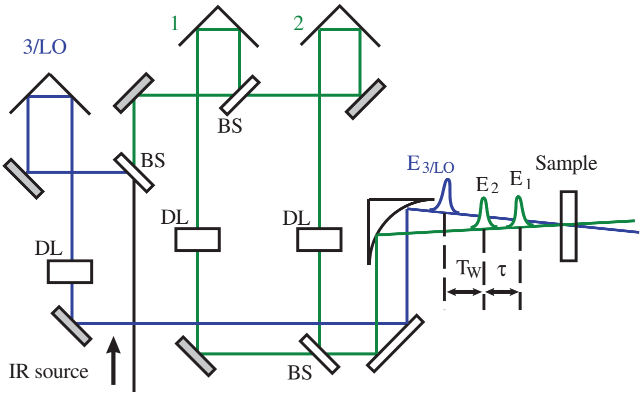

Figure 2.4. (Colour online) Experimental setup of the 2D FT spectrometer in the pump-probe geometry. BS: beam splitter, DL: Delay line.

is usually done in the echo approach where E_3 is bigger than E_{LO}. This can lead to a weaker detected signal, because the signal detected is usually in the form of

$$\frac{I_s - I_{LO}}{I_{LO}} \propto \frac{|S|}{|E_{LO}|} = \frac{|E_1| \cdot |E_2| \cdot |E_3|}{|E_{LO}|}. \tag{2.38}$$

The other approach is the pulse shaper method. It is also a two-beam experiment. The difference is that it adopts a pulse shaper to generate the collinear pulse-pair pump with adjustable delays instead of beam splitters and a delay line in the method discussed above, as shown in Figure 2.5 [22,86–89]. The pulse shaper is aligned in a 4-*f* geometry using a pair of diffraction gratings and a pair of cylindrical mirrors. The first grating and cylindrical mirror are used to disperse and collimate the frequency components of the incident mid-IR pulses. By inserting the Ge AOM (germanium acousto-optic modulator) to the Fourier plane, the dispersed pulse is then deflected at the Bragg angle with the specified desired amplitude and phase according to the acoustic wave passing through the crystal, which is controlled by an arbitrary waveform generator (AWG) equipped on a computer. At last, the deflected frequencies were transformed back into the time domain through the second grating and cylindrical mirror. In other words, under the modulation of Ge AOM, a Gaussian line shape corresponding to a single Gaussian pulse was able to be converted to an interference pattern, which corresponding to a collinear pulse-pair in the time domain (see Figure 2.5), and thus can be employed as the pump pulse. The major advantage of this method is to in principle eliminate the uncertainties of both the absolute τ and t_3 timings, and fundamentally solve the phase distortion problem, if the light intensity in the frequency domain can be perfectly controlled by the AOM. Similar to the above approach where much energy is wasted at the beam combiner, much of the excitation energy is wasted on the two gratings and the Ge AOM. The relative E_3&E_{LO} amplitudes can be adjusted by changing the beam polarisations [87], but applications in measuring anisotropy would be limited by this approach then.

2.3.2. *Instrumental transformation methods*

With recent developments, phase uncertainties in the numerical transformation methods to obtain ω_1 are now much more controllable. However, completely free of any phase

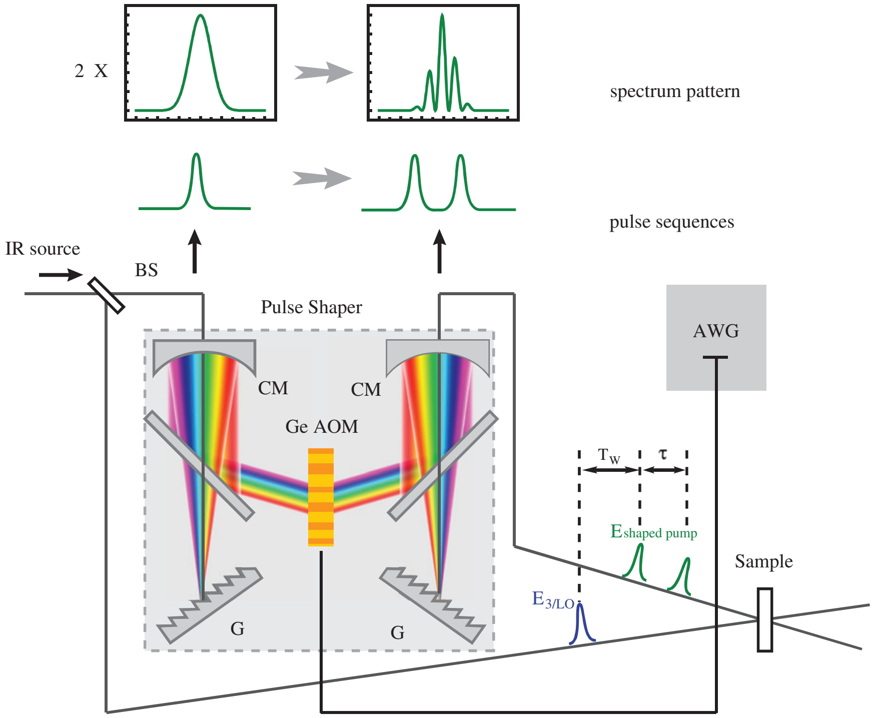

Figure 2.5. (Colour online) Experimental setup of the mid-IR pulse shaper based 2D IR spectrometer. BS: beam splitter, CM: cylindrical mirrors, G: grating, AWG: arbitrary waveform generator, Ge AOM: germanium acousto-optic modulator.

uncertainties can be only achieved by the instrumental transformation methods. In addition, acquiring an interferogram by scanning τ in the numerical transformation methods is always a timing consuming process. It is particularly inefficient in cases where kinetic or dynamic data from various waiting times are required from only a few frequency points. The instrumental transformation methods through which both ω_1 and ω_3 are directly resolved by refractive optics are apt for this application. Another significant limitation of the numerical transformation methods is that their excitation power is relatively low. Signals from direct excitations or couplings of vibrational modes with small transition dipole moments can be too weak to be detected by the methods. This is limited by the current ultrafast Mid-IR laser technology. A typical fs Mid-IR pulse has a bandwidth $100\sim300\,\mathrm{cm}^{-1}$ with energy $1\sim10\,\mu\mathrm{J}$/pulse with $0.5\sim1\,\mathrm{W}$ pump at 1 KHz with a pulse duration $40\sim150\,\mathrm{fs}$, dependent on the central frequency. Many vibrational peaks in condensed phases are only $10\sim20\,\mathrm{cm}^{-1}$ wide, which means that most of the energy in the fs pulse is wasted because most of the frequencies of the pulse don't overlap with the 0–1 or 1–2 transitions of the modes. If the pulse energy can be concentrated within this $10\sim20\,\mathrm{cm}^{-1}$ range, the excitation power and therefore the signal can be increased for many times. Many previously unlikely experiments, e.g. obtaining a 2D spectrum covering many vibrational modes and their couplings to resolve the molecular structures similar to that 2D NMR does, can then be realised by this approach. Such an approach with very high excitation power was recently developed by our group through synchronising a ps laser with a fs laser [70,90,91]. Our method is essentially a double instrumental transformation method to obtain both ω_1 and ω_3. Prior to our approach, another double instrumental approach with an etalon to directly resolve ω_1 was adopted in MDVS [2,71].

2.3.2.1. *The etalon approach.* The etalon approach is a two-beam experiment. It uses the pump/probe scheme where the pump frequency ω_1 is resolved by an etalon, and the probe frequency ω_3 is resolved by a spectrograph as in other approaches.

An etalon is also known as a Fabry–Pérot interferometer. It is typically made of two partially reflective dielectric mirrors separated by a small gap, the spacing of which can be controlled by a piezocrystal actuator or by mounting one of the mirrors on a stepping motor controlled translation stage. Once a fs laser IR pulse which is typically $100 \sim 300\,\mathrm{cm}^{-1}$ wide enters the etalon, it will be reflected back and forth between the mirrors. As the result of interference among the multiple reflections, only light within a certain narrow range of frequencies can transmit through the etalon. The transmittance function of the etalon is given by

$$T_e = \frac{(1-R)^2}{1+R^2-2R\cos\delta} = \frac{1}{1+F\sin^2(\delta/2)}, \tag{2.39}$$

where R is the reflectivity of the mirrors, $F = 4R/(1-R)^2$ is the coefficient of finesse, and $\delta = 4\pi l/\lambda$ is the phase difference between each succeeding reflection, with l is the spacing between two mirrors and λ is the wavelength of the incident light. The maximum transmission of an etalon occurs when $2l = m\lambda$, where the integer number m is the order of interference. The choice of interference order must follow the principle that only one transmission peak lies within the spectral region determined by the above transmittance function. The bandwidth of the transmitted pulse is determined by the reflection coefficient of the mirrors, which is typically chosen as $R \approx 90\%$ so that the output bandwidth is $5 \sim 20\,\mathrm{cm}^{-1}$. The center frequency of the transmitted pulse is scanned by adjusting the spacing l, which is typically controlled by a computer.

The experimental MDVS setup based on etalon is straightforward. For a system with only one fs OPA, the IR output is split into two beams ($\sim$90% and $\sim$10%). The beam with 90% of the IR light from the OPA goes through a computer-controlled etalon to get frequency resolved with a resolution $5 \sim 20\,\mathrm{cm}^{-1}$. This is the pump beam. The beam with only 10% intensity is the probe beam. In experiments, the pump and probe are crossed on the sample. The pump frequency ω_1 is then scanned by tuning the spacing between the two mirrors in the etalon by the computer. The signal detected is frequency resolved by a spectrograph to prove the ω_3 axis.

Compared to the numerical transformation methods, the etalon method is relatively inexpensive and easy to operate. However, since the pump pulse from the etalon is a narrow band pulse, its frequency resolution and temporal resolution are correlated by the uncertainty principle. A better frequency resolution means a worse temporal resolution. For example, if the frequency resolution is $\sim 10\,\mathrm{cm}^{-1}$, its temporal resolution is $1 \sim 2$ ps. Certainly this is only the pulse duration of the pump beam. The temporal resolution of the final signal is determined by the pulse durations of both pump and probe pulses.

With simple mathematical treatments, the final temporal resolution can be close to that of the probe pulse which is 40 ~ 150 fs. Therefore, both temporal and frequency resolutions of the etalon approach are generally not as good as those numerical methods. In addition, what the etalon does is to pick some frequencies out of a wide range of frequencies within one pulse. It does not amplify the pump power. As that is mentioned above, E_3 and E_{LO} are generally not adjustable in the pump/probe scheme, leading to a relatively weak signal from the etalon approach, compared to the numerical methods.

2.3.2.2. *The ps/fs hybrid approach.* The etalon approach is a completely phase-locked method and its signal is pure absorptive. Different from the numerical methods, the approach does not require any phasing procedure to obtain the pure absorptive lineshape. However, its relative weak signal prevents it from studying weak vibrational transitions or couplings. The difficulty in obtaining coating for the etalon mirrors with relatively constant reflectivities in a wide frequency range is also a problem.

After comparing the advantages and disadvantages of various MDVS approaches, we adopted a new approach to construct our MDVS apparatus with extremely high excitation power and independent tunable ω_1 and ω_3 covering almost the whole Mid-IR range. The unique design has created many novel opportunities for exploring molecular structures and dynamics. Our setup is a two-beam experiment, based on the pump/probe scheme, as shown in Figure 2.6.

Briefly, a ps amplifier and a fs amplifier are synchronised with the same seed pulse. The ps amplifier (~2.8 mJ/pulse) pumps an OPA to produce ~ 0.8 ps (vary from 0.7 ~ 0.9 ps in different frequencies) Mid-IR pulses with a bandwidth ~ 21 cm^{-1} (12 ~ 35 cm^{-1}) in a tunable frequency range from 500 cm^{-1} to 4000 cm^{-1} with energy 1 ~ 40 μJ/pulse (1 ~ 10 μJ/pulse for 500 cm^{-1} to 900 cm^{-1} and > 10 μJ/pulse for higher frequencies) at 1 kHz. The fs amplifier (~2.8 mJ/pulse) pumps another OPA to produce ~ 140 fs Mid-IR pulses with a bandwidth ~ 200 cm^{-1} in a tunable frequency range from 500 cm^{-1} to 4000 cm^{-1} with energy 1 ~ 40 μJ/pulse at 1 kHz. In the experiments, the ps IR pulse is the excitation beam. The fs IR pulse is the probe beam which is frequency resolved by a spectrograph yielding the ω_3 axis of a 2D spectrum. The temporal shapes of the IR pulses are Gaussian. Scanning the pump frequency yields the ω_1 axis of the spectrum. Two polarisers are added into the probe beam path to selectively measure the parallel or perpendicular polarised signal relative to the pump beam.

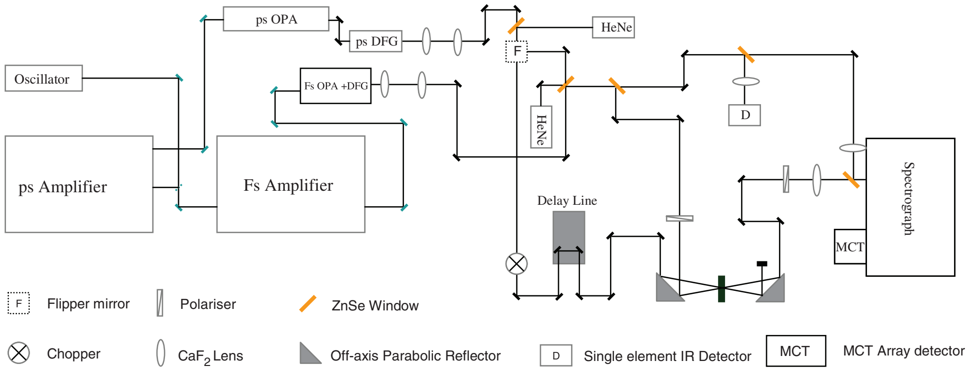

Figure 2.6. Schematic representation of the ps/fs hybridisation MDVS setup.

The key component of the setup is the synchronisation of the ps and fs amplifiers. Two special designs were adopted to accomplish the synchronisation: (1) we used the same seed pulse from the same oscillator to seed both amplifiers; (2) the two amplifiers have the same two-stage amplification in the cavity, which allows us relatively easily adjust the number of round trips of the light inside the cavity by changing the pump power. The synchronisation jitter is very small, ~ 100 fs, as shown in Figure 2.7.

The approach is a double instrumental transformation method. The probe frequency ω_3 is resolved from a fs IR pulse by a spectrograph as in other approaches. The pump frequency ω_1 is obtained by scanning the output frequency of the ps OPA through adjusting the positions and angles of the grating and crystals and other optics inside the OPA. As discussed above, in the pump/probe configuration, signals from both rephasing and nonrephasing pathways simultaneously emit along the same direction of the probe beam because the pump beam is the sum of the excitation pulse E_1 and E_2, and the probe beam is the sum of the excitation pulse E_3 and the local oscillator E_{LO}. There is no need in the pump/probe configuration to scan twice to obtain signals from both rephasing and nonrephasing pathways as what is done in the echo approach. Different from the numerical transformation approaches where the procedures to obtain ω_1 inevitably introduce some phase uncertainties, the ps/fs hybridisation method obtains ω_1 directly from the grating inside the OPA. Its signal is therefore phase-locked and the spectra are pure absorptive without further data processing required. The major advantages of the design are: (1) its excitation power is extremely high with $1 \sim 40$ μJ/pulse concentrated within $\sim 20\,\mathrm{cm}^{-1}$ band width, which is at least one order of magnitude higher than most other MDVS setups. Such high pump power enables measurements on vibrational transitions and couplings with very weak signals. Almost all molecules with active IR modes in condensed phases can be studied by this high power approach now. (2) The excitation and detection frequencies ω_1 and ω_3 are independently tunable because they are from different OPAs. This design allows us to probe the coupling and energy transfer between essentially any two modes only if their frequencies are within the range of $500 \sim 6000\,\mathrm{cm}^{-1}$. The major drawback of the approach is that the temporal and frequency resolutions of the pump pulse are correlated by the uncertainty principle, similar to that of the etalon approach. As displayed in Figure 2.7, the band width of the ps pulse is $\sim 18\,\mathrm{cm}^{-1}$, and its pulse duration is 0.8ps. Therefore, it is difficult to obtain fast dynamics ($100 \sim 200$ fs) with a good frequency resolution ($< 10\,\mathrm{cm}^{-1}$). The numerical methods don't have this problem, because the temporal resolution is determined by the fs pulse duration, and the method frequency resolution is determined by the sampling method, and the intrinsic frequency resolution is determined by the molecular dynamics of the samples.

As discussed above, each MDVS approach has its own advantages and disadvantages. In summary, the numerical transformation methods have better temporal and frequency resolutions. The instrumental transformation methods have faster data acquisition rates and well defined results. Different approaches may be apt for different applications.

2.4. *On the analysis of MDVS spectra*

2.4.1. *Origins of diagonal and cross peaks*

As introduced above, a typical MDVS spectrum can be plotted in three dimensions, the signal amplitude as a function of both ω_1 and ω_3, shown in Figure 2.9. By varying the

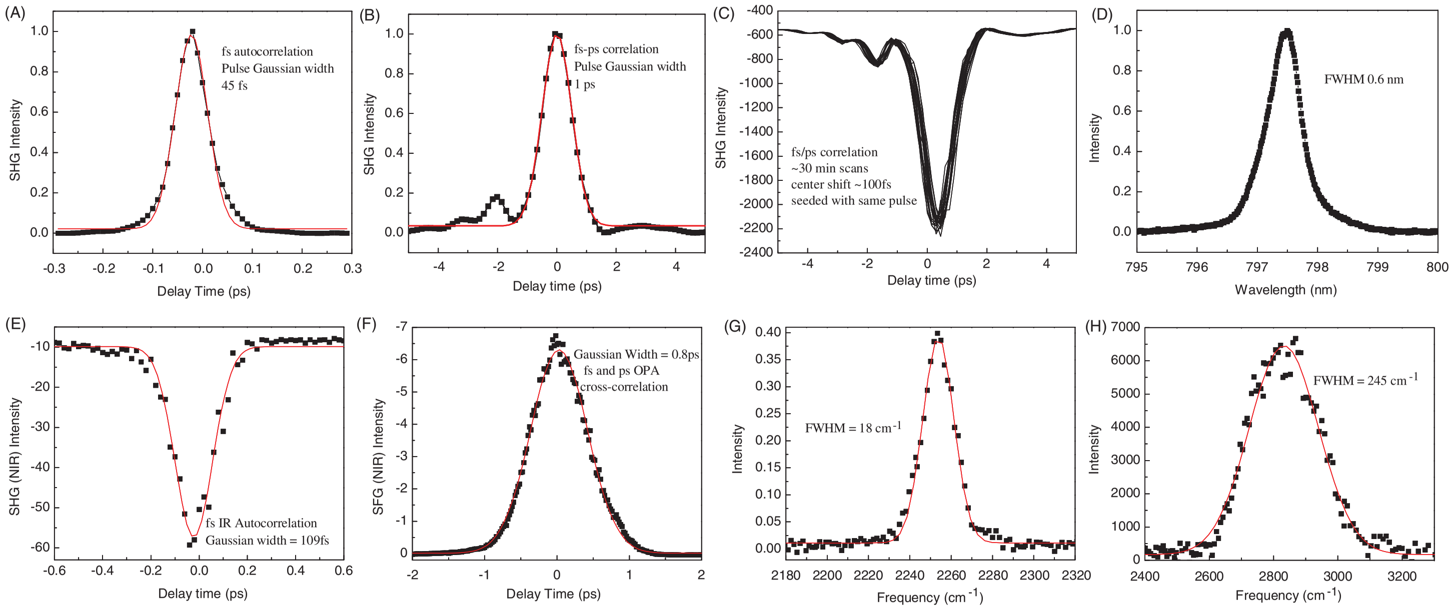

Figure 2.7. (Colour online) (A) Autocorrelation trace of the fs amplifier output showing that the pulse duration is ∼45 fs; (B) Crosscorrelation trace between the fs and ps amplifier outputs showing that the ps pulse duration is ∼1 ps; (C) fs/ps crosscorrelation traces by continuous scan in 30 minutes showing that the synchronisation jitter is ∼100 fs; (D) the band width of the ps amplifier output ∼0.6 nm; (E) autocorrelation trace of the fs OPA output showing that the pulse duration is ∼109 fs; (F) crosscorrelation trace between the fs and ps OPA outputs showing that the ps IR pulse duration is ∼0.8 ps; (G) the band width of the ps OPA output ∼18 cm^{-1}; (H) the band width of the fs OPA output ∼245 cm^{-1}.

waiting time T_w, we have one more dimension for the data. The slice along the diagonal of the 2D frequency spectrum gives an identical spectrum as the 1D IR spectrum obtained from FTIR. The major difference between 1D and 2D IR data is that 2D IR data can detect correlations among different vibrational frequencies. Molecular structural and dynamic information can be obtained from such correlations which generally show up in the 2D spectra as the growth of cross peaks appearing on the off-diagonal positions of the spectra and the change of the diagonal peak lineshape. The time evolution of diagonal peakshape from elongated to round along the diagonal, as can be seen from the two diagonal peaks in Figure 2.18, is called spectral diffusion. The phenomenon is caused by the exchange of local environments of the IR probes because of the molecular motions in the system. Analysing this type of lineshape change in principle can provide information about the probe's local electric field and environmental structural fluctuations [40,53]. In general, the lineshape of a 2D peak is sensitive to the phase errors. Great care must be taken to properly phase the data before a reasonable result can be obtained from the spectral diffusion analysis. The growths of cross peaks can be from various origins, e.g. (1) vibrational couplings, (2) energy transfers, (3) chemical exchanges, and (4) heat effects [3,4,8,12,14,19,27,33,34,38,48,49,59,79,80,92,93]. Majority of molecular information that MDVS methods can provide is carried by these cross peaks.

In this section, the four types of molecular mechanism responsible for the growth of cross peaks in 2D spectra are introduced in details. The origins of both diagonal and cross peaks are analysed with the light-material interaction principles through Feynman diagrams.

Origin 1: Vibrational Coupling and Intramolecular Vibrational Energy Exchange

Vibrational couplings and intramolecular vibrational energy transfers are probably the most common reasons causing the growth of cross peaks because almost all vibrational modes inside a molecule are anharmonically coupled. Excellent research work on this topic can be found in literature [2,8,48,94]. Here, the vibrational coupling and energy exchange between a Fermi resonant mode and the NCO asymmetric stretch of ethylisocyanate are used to demonstrate the principle.

Figure 2.8 displays the FTIR spectrum of a dilute (0.2 wt%) ethylisocyanate solution in CCl_4 in the frequency range of the NCO asymmetric stretch [83]. The main peak at $2278\,cm^{-1}$ is assigned to the NCO asymmetric stretch and the small peak at $2220\,cm^{-1}$ is assigned to a dark mode (called D) coupled with the NCO asymmetric stretch through a Fermi resonance. The main peak is actually the motional narrowing result of two isomers rotating along the CN single bond of the ethylisocyante [95]. The spectrum is indeed from two exchanging indistinguishable isomers, which can be treated as a single component.

Figure 2.9 shows T_w dependent 2D IR spectra of the ethylisocyanate solution [83]. The red peaks 1 ($\omega_1 = 2278\,cm^{-1}$; $\omega_3 = 2278\,cm^{-1}$) and 4 ($\omega_1 = 2220\,cm^{-1}$; $\omega_3 = 2220\,cm^{-1}$) are assigned to the 0–1 transitions of the NCO asymmetric stretch mode and the dark mode D, respectively. Both ω_1 and ω_3 have the same frequency as measured from FTIR. They come from five Feynman diagrams shown in Figure 2.10. In all five diagrams, during the two coherence periods τ and t_3, all coherences (01 or 10) are between the ground state 0 and the 1st excited state 1 of the same mode, which determines that the peak from these diagrams has ω_1 (from the τ period) $= \omega_3$ (from the t_3 period) $= \omega_{01}$ (the 0–1 transition frequency) of the same mode. For the NCO asymmetric stretch mode, $\omega_{01} = 2278\,cm^{-1}$,

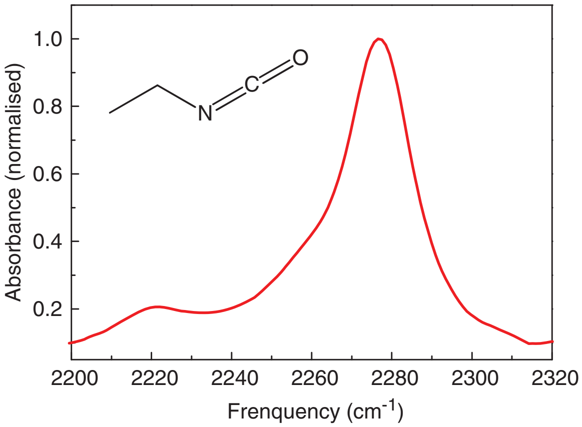

Figure 2.8. (Colour online) FTIR spectrum of a 0.2 wt% ethylisocyanate solution in CCl_4 for the NCO asymmetric stretch. The main peak at 2278 cm^{-1} is for the NCO asymmetric stretch and the small peak at 2220 cm^{-1} is for a dark mode D coupled with the NCO asymmetric stretch through a Fermi resonance. Inset: the molecular structure of ethylisocyanate [83].

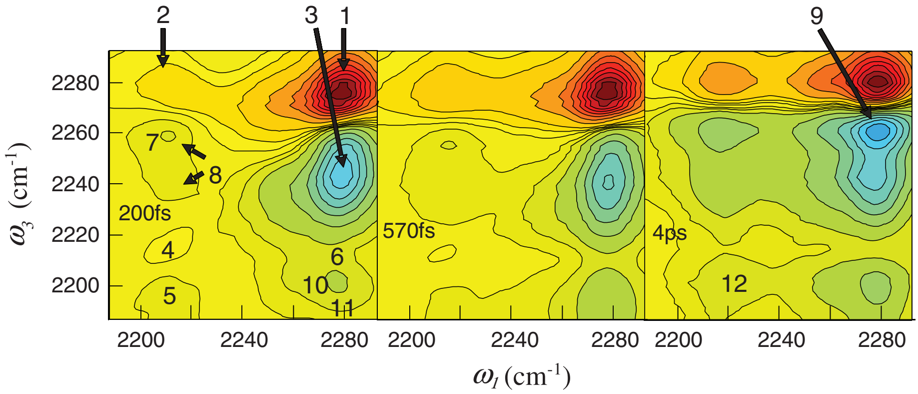

Figure 2.9. (Colour online) T_w dependent 2D IR absorptive spectra of a 0.2wt% ethylisocyanate/ CCl_4 solution at room temperature from a broad band echo 2D IR setup. [83].

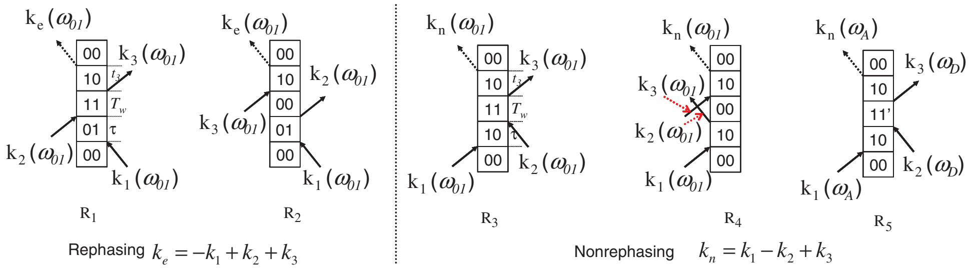

Figure 2.10. Feynman diagrams contributing to Peak 1 and 4 in Figure 2.9. 0 represents the ground state, 1 and 1′ represent the 1st excited states of the NCO asymmetric stretch mode and the dark mode.

and for the dark mode, it is 2220 cm^{-1}. During the population period T_w, diagrams $R_1 \sim R_4$ produce populations in either the 1st excited state (11, the excited state stimulated emission) or the ground state (00, the ground state bleaching). Both stimulated emission and ground state bleaching "add" more light to the local oscillator. Therefore, the peak signals from them are positive and colored as red. Diagram R_5 from the nonrephasing phase match condition produces populations (or superposition) oscillating between the 1st excited states of the dark mode and the NCO asymmetric stretch mode (11′). The signal from R_5 will oscillate at the frequency difference between the two modes 2278 cm^{-1} – 2220 cm^{-1} = 58 cm^{-1}. In other words, the oscillation period is ~575 fs ($(1/58)/(3 \times 10^{10}) = 5.75 \times 10^{-13}$ s = 575 fs). Similar phenomena have been observed in metal carbonyl compounds [27,48]. The numbers of the nonrephasing and rephasing diagrams are different, which counts for the slightly-distorted lineshapes in 2D IR spectra (the sum of signals from all diagrams) of short T_w periods in Figure 2.9. The oscillating signal from R_5 decays typically much faster than signals from other diagrams which have normal population decays. Therefore, at longer T_w periods, the signal sizes from both phase match conditions will become closer, and the lineshape distortion will be less severe. Diagram R_5 requires the two coupled modes to be both excited by the first two interactions E_1 and E_2. This cannot be fulfilled in the narrow-pump/broad-probe methods (the etalon and ps/fs hybridisation approaches) because the bandwidth of the pump pulse is too narrow to cover the two modes simultaneously. Therefore, in these two approaches, the 0- transition peak is only from $R_1 \sim R_4$. Similarly, in the following analysis, those diagrams containing excitations of different modes by the first two pulses don't exist in the experiments by the narrow-pump/broad-probe methods.

Peak 3 (2278 cm^{-1}, 2242cm^{-1}) and Peak 5 (2220 cm^{-1}, 2195cm^{-1}) are assigned to the 1–2 transitions of the NCO asymmetric stretch mode and D. They are from diagrams R_6 and R_7 shown in Figure 2.11. The shape of peak 3 is obviously longer than peak 1 and the intensity is around 60% of peak 1. The observation is very similar to those observed for the Fermi resonance in o-methylphenol-OD and o-ethoxylphenol-OD [49]. Here the elongated shape is tentatively assigned to the coupling between the 2nd excited state of the NCO asymmetric mode and a dark mode through another Fermi resonance without further experiments. During the τ period, both diagrams R_6 and R_7 produce a coherence (01 or 10) between the ground state **0** and the 1st excited state **1** of the same mode, determining $\omega_1 = \omega_{01}$. During the t_3 period, both diagrams produce a coherence (21) between the 1st excited state 1 and the 2nd excited state **2** of the same mode,

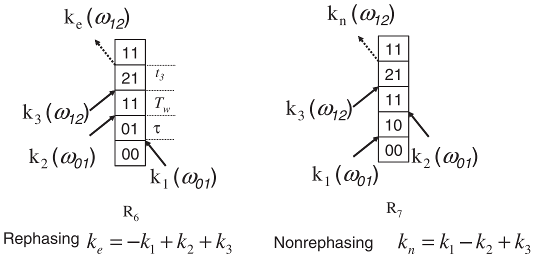

Figure 2.11. Feynman diagrams contributing to Peak 3 and 5 in Figure 2.9. 0, 1, and 2 represent the ground state, the 1st and 2nd excited states of the NCO asymmetric stretch mode and the dark mode.

determining $\omega_3 = \omega_{12}$. During the population period T_w, both diagrams produce populations in the 1st excited state (11, the excited state absorption). The excited state absorption "subtracts" light from the local oscillator. The signal is negative and colored as blue. No oscillating populations are produced. The diagram where the 2nd interaction produces 11′ and then the 3rd interaction convert 11′ into 12 described in literature [8] is not a likely pathway (or if any, its contribution is small) to produce Peak 3 or 5. The conclusion is supported by: (1) no oscillating signal is observed for the 1–2 transitions of two coupled modes; and (2) the 1–2 transition peaks are smaller than the corresponding 0–1 transition peaks. The existence of this diagram would have produced an oscillating signal and made the 1–2 signal bigger than the 0–1 signal (three 1–2 diagrams, the signal from each is 2 times of the 0–1 transition, while there are only five 0–1 diagrams, assuming the transition dipole moments of the two coupled modes are similar, which is true for the asymmetric and symmetric stretches of RDC [8]).

Peak 2 ($2220\,\text{cm}^{-1}$, $2278\,\text{cm}^{-1}$) and 6 ($2278\,\text{cm}^{-1}$, $2220\,\text{cm}^{-1}$) (red peak, almost cancelled out by the big blue peak nearby) come from both "static" (the vibrational coupling, which is a static property between two vibrational modes) and "dynamic" (the energy transfer, which is time dependent) contributions. The static contribution because of vibrational coupling consists of two rephasing diagrams R_8 and R_9 and one nonrephasing diagram R_{10} in Figure 2.12. During the τ period, all diagrams produce a coherence (01′ or 1′0) between the ground state **0** and the 1st excited state **1** of one mode, resulting in $\omega_1 = \omega_{01'}$. During the t_3 period, all diagrams produce a 0–1 coherence (10) of the other mode, determining $\omega_3 = \omega_{01}$. The pathways determine that the coordinates of the peaks must be either $(\omega_{01'}, \omega_{01})$ or $(\omega_{01}, \omega_{01'})$. During the population period T_w, R_9 and R_{10} produce populations in the ground state (00, the ground state bleaching). R_8 creates a superposition between the 1st excited state of D and the NCO asymmetric stretching mode 1st excited state (11′, the excited state stimulated emission), and the signal from this diagram oscillates with T_w at a frequency equal to the $58\,\text{cm}^{-1}$ ($= \omega_{01} - \omega_{01'}$, $\sim 575\,\text{fs}$). The dynamic contribution is from the intramolecular vibrational energy exchange between D and the NCO asymmetric stretch mode, which consists of four diagrams $R_{1'}$, $R_{2'}$, $R_{3'}$, and $R_{4'}$ shown in Figure 2.13. During the coherence periods, these four diagrams generate exactly the same coherences as the static diagrams, therefore producing the same peaks. During the population period, vibrational energy exchanges induce population exchanges in both ground and 1st excited states between two modes. The exchanges don't produce any oscillating signal.

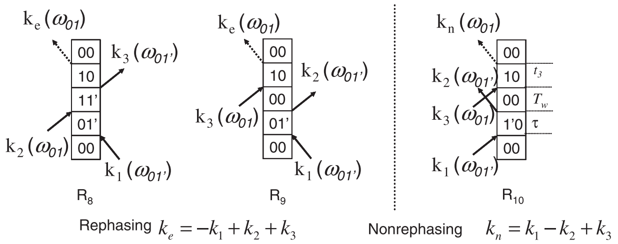

Figure 2.12. Feynman diagrams "statically" contributing to Peak 2 and 6 in Figure 2.9. 0, 1, and 1′ represent the ground state and the 1st excited states of the NCO asymmetric stretch mode and the dark mode.

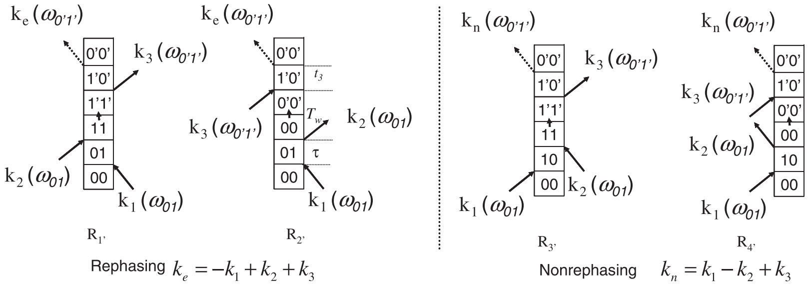

Figure 2.13. Feynman diagrams "dynamically" contributing to Peak 2 and 6 in Figure 2.9. 0, 1, and 1′ represent the ground state and the 1st excited states of the NCO asymmetric stretch mode and the dark mode.

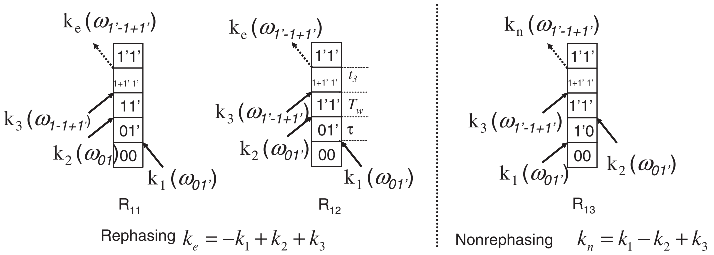

Figure 2.14. Feynman diagrams contributing to Peak 7 and 10 in Figure 2.9. 0, 1, 1′and 1 + 1′ represent the ground state, the 1st excited states and the combinational band of the NCO asymmetric stretch mode and the dark mode.
Note: the combinational band can be the sum of the NCO asymmetric stretch + any suitable modes which are strongly coupled to it and can shift the NCO 0–1 transition frequency with the same amplitude.

Peak 7 (2220 cm^{-1}, 2260 cm^{-1}) and 10 (2278 cm^{-1}, 2202 cm^{-1}) are absorption transitions between the 1st excited state and the combinational band, originating from two rephasing diagrams R_{11} and R_{12}, and one nonrephasing diagram R_{13} in Figure 2.14. All the diagrams are excited state absorptions, resulting in blue peaks. During the t_3 period, the diagrams produce a coherence (1 + 1′ 1′) between the 1st excited state and the combinational band of the two modes. R_{11} creates a superposition between the dark mode 1st excited state and the NCO asymmetric stretching mode 1st excited state after the 2nd interaction, and the signal from this diagram oscillates with T_w at a frequency equal to the 58 cm^{-1} ($= \omega_{01} - \omega_{01'}$).

Peak 8 (2220 cm^{-1}, 2242 cm^{-1}) and 11 (2278 cm^{-1}, 2195 cm^{-1}) are peaks of intramolecular vibrational exchanges between the two modes, from the 1st excited state absorption diagrams $R_{6'}$ and $R_{7'}$ in Figure 2.11. Peak 8 has an elongated lineshape along ω_m, which is similar to peak 3. The upper part of peak 8 overlaps with peak 7.

Peaks 9 (2278 cm^{-1}, 2260 cm^{-1}) and 12 (2220 cm^{-1}, 2202 cm^{-1}) come from vibrational energy exchanges between the NCO asymmetric stretching mode and the dark mode (diagrams R_{14} and R_{15} in Figure 2.16), and vibrational coupling (diagram R_{16}). Accompanying the evolution of the population period, the signal from R_{16} will diminish very fast, while signals from the other two will increase and then decay with the normal vibrational lifetimes.

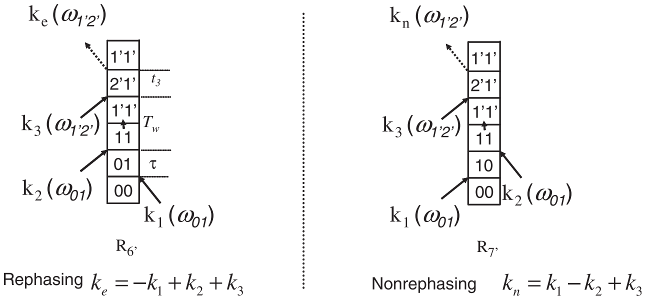

Figure 2.15. Feynman diagrams contributing to Peak 8 and 11 in Figure 2.9. 0, 1, 1′, 2, and 2′ represent the ground state, the 1st excited states, and the 2nd excited state of the NCO asymmetric stretch mode and the dark mode. During the population period, vibrational exchanges produce population exchanges.

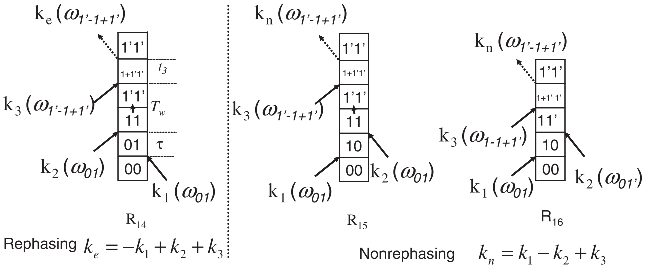

Figure 2.16. Feynman diagrams contributing to Peak 9 and 12 in Figure 2.9. 0, 1, 1′and 1 + 1′ represent the ground state, the 1st excited states and the combinational band of the NCO asymmetric stretch mode and the dark mode.

From the above analysis, the energy level diagram of the NCO asymmetric stretch mode and the dark mode of the ethylisocyanate molecule can be described in Figure 2.17 [83].

The analysis here is for data from a broad-band numerical Fourier transformed 2D IR method. In the narrow-pump/broad-probe 2D IR measurements, all diagrams with oscillations during the T_w period will not be applicable since the narrow pump pulse is too narrow to excite both modes at the same time.

Origin 2: Chemical Exchanges

Chemical exchanges, e.g. hydrogen bond formation and dissociation [3,14,32,34,58,59], and isomerisations [33,43], are dynamic equilibrium, which ubiquitously exist in nature. In chemical exchanges, the macroscopic concentration of each species is constant, but all species are constantly exchanging at the microscopic level. They can also produce cross peaks in 2D IR spectra [4,6]. The major difference between chemical exchanges and vibrational couples is that the probe vibrational modes of species under exchange are not coupled. Therefore, among the Feynman diagrams provided in the above section, those related to vibrational coupling, e.g., those producing oscillating populations, or those associated with the combinational band, are not applicable to chemical exchanges. A slow

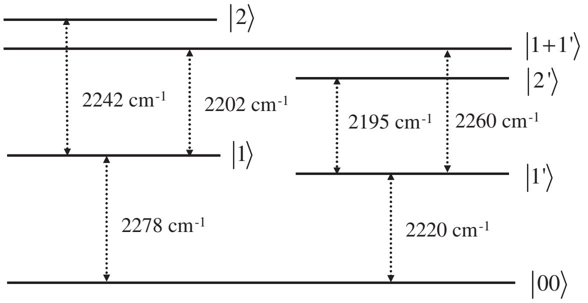

Figure 2.17. Energy level diagram of ethylisocyanate. |1⟩ and |2⟩ represent the 1st and 2nd excited states of the NCO asymmetric stretch mode. |00⟩ represents the ground state. |1 + 1′⟩ represents the combinational band (both modes are excited to the 1st excited state). |1′⟩ and |2′⟩ represent the 1st and 2nd excited states of the dark mode. In all above Feynman diagrams, n or n’ represents either mode, different from the assignments here [83].

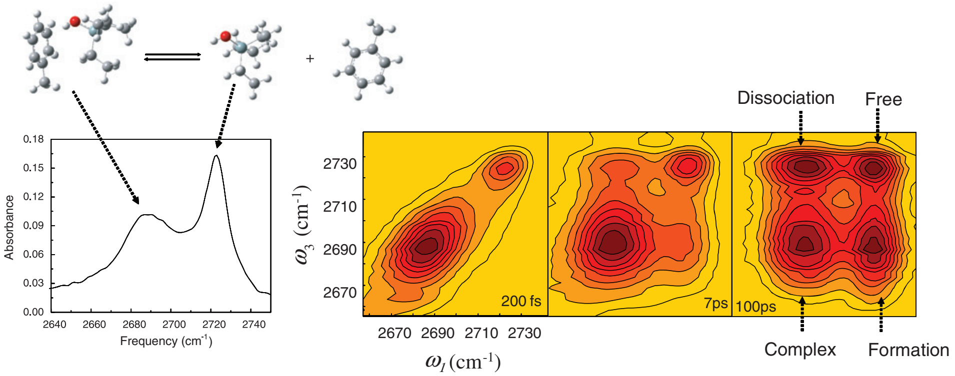

Figure 2.18. (Colour online) FTIR and 2D IR (only for 0–1 transition) spectra of hydroxyl-od stretches of free and complexed triethylsilanol molecules in a 1.6 wt% of triethylsilanol solution in 1:4 wt toluene and CCl_4 mixed solvent at room temperature. In the solution, some triethylsilanol molecules form complexes with toluene, while some stay free in CCl_4. These two types of silanol molecules are under fast chemical exchanges, manifested by the growth of the cross peaks in 2D IR spectra [83].

exchange example (the exchange is slower than the dephasing times of the vibrational probes) will be used to demonstrate the principle.

Figure 2.18 are FTIR and 2D IR (only for 0–1 transition) spectra of hydroxyl-od stretches of free (2722 cm^{-1}) and complexed triethylsilanol molecules (2688 cm^{-1}) in a 1.6 wt% of triethylsilanol solution in a toluene/CCl_4 (1/4 wt) mixed solvent at room temperature [83]. In the solution, some triethylsilanol molecules form complexes with toluene, and some stay free with CCl_4. These two types of silanol molecules are under chemical exchanges, manifested by the growth of the cross peaks in 2D IR spectra. In a chemical exchange, the vibrational excitation is conserved in the same vibrational mode, while the mode’s vibrational frequency is altered by the exchange. The frequency change indicates that the exchange has occurred because the frequency change induced by environment change is almost instantaneous. For instance, if the OD stretch of a free silanol molecule is excited, it will be vibrating at its frequency 2722 cm^{-1} during the τ period. If during the population period T_w, this silanol molecule forms a complex with a toluene molecule, its OD stretch is still vibrating but now at 2688 cm^{-1}, the frequency of the complexed silanol during the t_3 period, assuming the complex formation does not deactivate the vibration. The process forms the formation cross peak ($\omega_1 = 2722\,\mathrm{cm}^{-1}$, $\omega_3 = 2688\,\mathrm{cm}^{-1}$). The physical picture of the growth of cross peaks here is different from the intramolecular vibrational energy exchange. However, the Feynman diagram analysis for the growth of cross peaks in chemical exchanges is actually identical to that for the vibrational energy transfer. Cross peaks **Dissociation** and **Formation** are from diagrams $R_{1'} \sim R_{4'}$, and diagonal peaks **Free** and **Complex** are from $R_1 \sim R_4$. The corresponding 1–2 transition exchange peaks [34] (not shown here) are from $R_{6'}$ and $R_{7'}$, and the corresponding 1–2 transition free and complex peaks (not shown here) are from R_6 and R_7.

Origin 3: Intermolecular Vibrational Energy Exchanges

Intermolecular vibrational energy relaxations are ultimate pathways for vibrational energy to dissipate into environment in condensed phases. Intermolecular vibrational energy transfers can also produce cross peaks in 2D IR spectra. There are two cases: 1, the vibrational probes are directly involved in the energy transfers [70,90,96,97]; and 2, the vibrational probes are not involved in the energy transfer process but act as the reporters [98]. In the first case, the vibrational probe modes of different frequencies are under energy exchange. The intermolecular energy transfer produces cross peaks in 2D IR spectra in a way similar to the intramolecular vibrational energy transfer. A typical example is the energy exchange between SCN^- and $S^{13}C^{15}N^-$ in $KSCN/KS^{13}C^{15}N$ (1/1) mixed aqueous solutions [90], displayed in Figure 4.1. The energy transfer peaks are from diagrams $R_{1'} \sim R_{4'}$ for the red cross peaks, and $R_{6'} \sim R_{7'}$ for the blue cross peaks. In the second case, the mechanism is different. In the following, an example is used to demonstrate how cross peaks are generated in 2D IR spectra for this situation [98].

Figure 2.19 displays the FTIR and 2D IR spectra of CN groups of acetonitrile-d$_3$ (~2263 cm^{-1}) and benzonitrile (~2230 cm^{-1}) molecules in a mixed acetonitrile-d$_3$ (A) and benzonitrile (B) solution (molar ratio A/B ~1.8) at room temperature [83]. In the solution, once the nitrile asymmetric streches are excited to their 1st excited states, the excitations of both molecules quickly relax to intramolecular low frequency modes within 20 ps as we can see that the 1–2 transition peaks in panel 15 ps are almost gone, and then the vibrational energy of some of these low frequency modes exchanges between the two types of molecules within 30 ~ 50 ps. The energy exchange is manifested by the growth of the cross peaks in 2D IR spectra. Note: very little vibrational energy has exchanged directly between the nitrile groups, since no 1–2 exchange cross peaks (should be at the positions of (2263 cm^{-1}, 2209 cm^{-1}) and (2230 cm^{-1}, 2245cm^{-1}) similar to peak 8 and 11 in Figure 2.9 has been observed.

In Figure 2.19, the origins of the diagonal peaks and their corresponding 1–2 transition peaks in the 2 ps panel (before vibrational energy relaxations) are identical to those in the chemical exchange cases. In other words, the diagonal peaks are from diagrams $R_1 \sim R_4$, and their 1–2 transition peaks are from R_6 and R_7. After intramolecular vibrational energy relaxations in panels 15 ps and 30 ps, the 1–2 transition peaks (2263 cm^{-1}, 2245 cm^{-1}) and (2230 cm^{-1}, 2209 cm^{-1}) in panel 2 ps disappear, and two new blue peaks (2263 cm^{-1}, 2254 cm^{-1}) and (2230 cm^{-1}, 2224 cm^{-1}) grow in. The disappearances of the

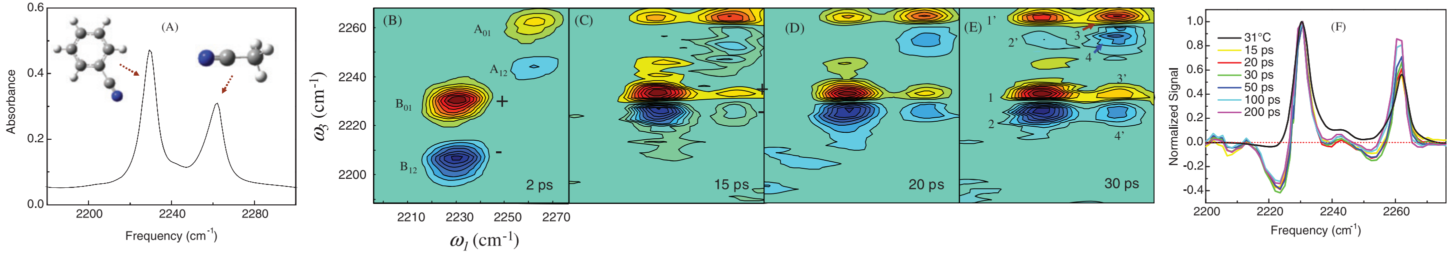

Figure 2.19. (Colour online) FTIR (A) and 2D IR spectra (B ~ E) of CN groups of acetonitrile-d$_3$ (~2263 cm^{-1}) and benzonitrile (~2230 cm^{-1}) molecules in a mixed acetonitrile-d$_3$ (A) and benzonitrile (B) solution (molar ratio A/B ~ 1.8) at room temperature. In the solution, after excitation, the vibrational energy of the nitrile groups of both molecules mostly relaxes to intramolecular low frequency modes, and then the vibrational energy of some of these low frequency modes exchanges between the two types of molecules. (F) Temperature dependent IR spectral difference between 54°C and 23°C (black line 31°C) and pump/probe spectra at difference time delays. The spectral difference is obtained from (transmittance$_{54°C}$ − transmittance$_{23°C}$)/transmittance$_{23°C}$ in linear IR measurements. The data clearly show that the dip at 2224 cm^{-1}(the sum of peaks 2 and 4′ in C ~ E is not from heating [83].

two 1–2 transition peaks indicate that the excitation of the CN stretches have relaxed away. Two diagonal red peaks are still in the spectra after relaxations, resulting from that the ground states are not filled by the relaxations of CN excitations and the transition dipole moment decrease with the increase of internal molecular temperature (which can be confirmed with temperature dependent FTIR measurements in (F)). Both factors are ground state bleaching. Therefore, the origins of the diagonal peaks after intramolecular relaxations are diagrams R_2 and R_4. The new blue peaks ($2263\,\text{cm}^{-1}, 2254\,\text{cm}^{-1}$) and ($2230\,\text{cm}^{-1}, 2224\,\text{cm}^{-1}$) come from combinational band absorptions R_{14} and R_{15}; similar to peak 9 and 12 in Figure 2.9 (the dark mode here can be one or more modes which accept energy from the CN groups). This relaxation induced absorption phenomenon has been observed previously [99,100].

After intermolecular energy exchanges, two additional red peaks and two additional blue peaks grow in as in panels 15 ps and 30 ps in Figure 2.19. The origin mechanisms of these peaks are different from those of intramolecular energy exchange peaks which are the results of direct energy exchanges between two modes. The peaks here are not the results of direct energy exchanges between the CN groups, but energy exchanges among other modes. The red cross peaks ($2263\,\text{cm}^{-1}$, $2230\,\text{cm}^{-1}$) and ($2230\,\text{cm}^{-1}$, $2263\,\text{cm}^{-1}$) are purely from ground state bleachings caused by energy exchanges among low frequency modes (including heat) between two molecules, which can be expressed as diagrams $R_{2'}$ and $R_{4'}$. There is no stimulated emission contribution for the red cross peaks because all CN stretch excited state populations have relaxed to the low frequency modes. The blue cross peaks ($2263\,\text{cm}^{-1}$, $2224\,\text{cm}^{-1}$) and ($2230\,\text{cm}^{-1}$, $2254\,\text{cm}^{-1}$) are both from sequent intramolecular and then intermolecular energy relaxations, expressed as diagrams R_{17} and R_{18} in Figure 2.20. The physical picture of the diagrams is that during the population period, after the CN group of one molecule (e.g. A) is excited to its 1st excited state with an excitational frequency $\omega_1 = 2263\,\text{cm}^{-1}$, the excitation relaxes to intramolecular low frequency mode(s) ($\boldsymbol{L}$), and then the energy of $\boldsymbol{L}$ transfers to the low frequency mode(s) ($\boldsymbol{L'}$) of another molecule (B). The 3rd pulse creates a coherence between $\boldsymbol{L'}$ and the combinational band $\boldsymbol{1'} + \boldsymbol{L'}$ of B. The coherence produces a signal with an emission frequency $\omega_3 = 2224\,\text{cm}^{-1}$. The two diagrams are excited state absorptions, peaks from them are therefore negative and labeled as blue.

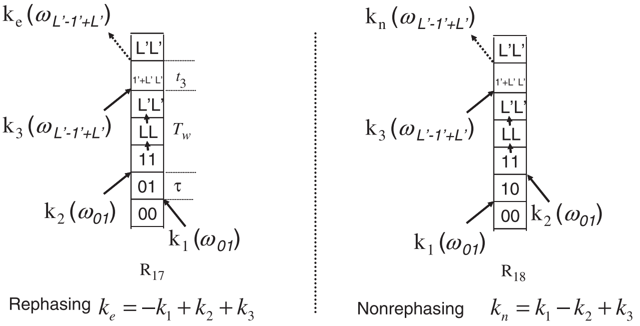

Figure 2.20. Feynman diagrams contributing to intermolecular energy exchange blue cross peaks ($2263\,\text{cm}^{-1}$, $2224\,\text{cm}^{-1}$) and ($2230\,\text{cm}^{-1}$, $2254\,\text{cm}^{-1}$) in figure 2.15. 0, 1, 1′, L, L′ and 1′ + L′ represent the ground state, the 1st excited states, the low frequency mode(s), and the combinational band of the CN stretch mode and the low frequency mode(s) of acetonitrile and benzonitrile.

Origin 4: Vibrational Relaxation Induced Heat Effects

In the 2nd case of intermolecular vibrational energy transfer discussed above, we mentioned that the red peaks at long waiting times are partially caused by the heat effect from the vibrational relaxations. Here a more detailed description about heat induced cross peaks in 2D IR spectra is provided.

In a nonlinear vibrational spectroscopic measurement, it is quite typical that the relaxation of a vibrational excitation can increase the temperature of the sample within the focus spot for a few degrees [70,98,101]. The amplitude of temperature increase (~6°C) can be estimated with the following experimental parameters: the excitation pulse energy of 5 μJ/pulse, the diameter of focus spot of 100 μ*m*, the sample thickness of 20μ*m*, the sample density and heat capacity assumed to be the same as those of water. The temperature increase can have several effects on the sample: (1) the absorption coefficient of the vibrational modes are altered; (2) the populations of molecules in different substates also change because of the Boltzmann distribution; (3) the local structures and chemical equilibrium shift following the temperature change, e.g. H-bonds become weaker at higher temperature [30,102]. These effects produce new absorptions and bleachings at various temperatures in both temperature difference FTIR spectra (Figure 2.19(F) and Figure 2.21(D) ~ (E)) and 2D IR spectra (Figure 2.21(C)) [96].

The black curve in Figure 2.21(A) is the FTIR spectrum of a KSeCN/D_2O (~1/2.4 molar ratio) solution. The peak at ~ 2060 cm^{-1} is the CN stretch of the $SeCN^-$ anion, the shoulder at ~ 2636 cm^{-1} is assigned to a combination band of $SeCN^-$ through FTIR measurements in different solvents, and the rest of the broad peak in the range of

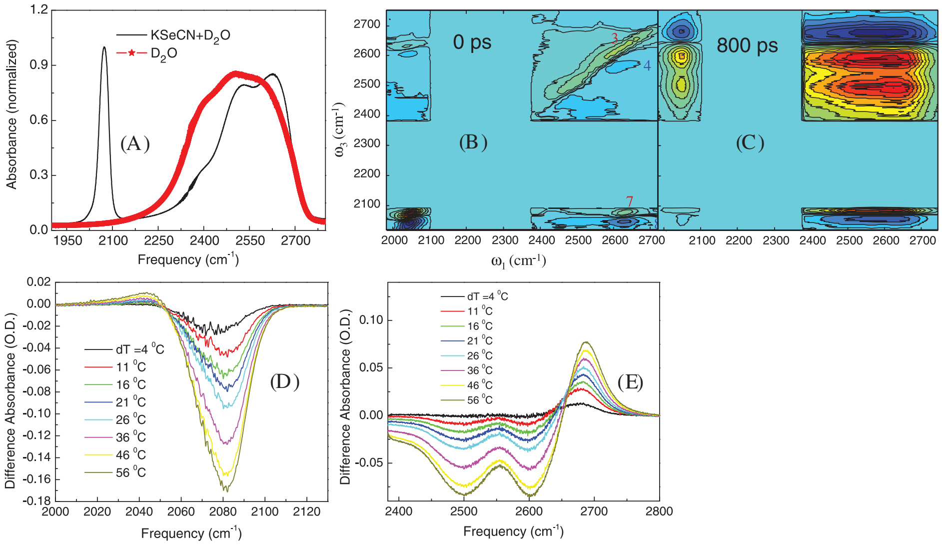

Figure 2.21. (Colour online) (A) FTIR spectrum (the black curve); (B) and (C) 2D IR spectra at two waiting times, and (D) and (E) temperature difference FTIR spectra in the CN stretch and OD stretch frequency ranges of a KSeCN/D_2O (~1/2.4 molar ratio) solution. The temperature difference spectra were obtained from subtracting the FTIR spectrum at room temperature (24°C) from the spectrum at a higher temperature, e.g. line 11°C in D&E represents the subtraction result from 35°C–24°C. Positive values in (D) and (E) represent absorption, and negative values represent bleaching. Reprinted with permission from [96]. Copyright 2010, American Institute of Physics.

$2400 \sim 2700\,\text{cm}^{-1}$ is assigned to the OD stretch of D_2O. (B)&(C) are 2D IR spectra of the solution at waiting time 0 ps and 800 ps. At the short waiting time, the diagonal peak pairs and the cross peak pairs because of the vibrational coupling between the combination band and the CN stretch are clearly visible. At the long waiting time 800 ps, most of the vibrational excitations of OD and CN have relaxed into heat because their vibrational lifetimes are relatively short (<100 ps) compared to 800 ps [96], but many peaks still appear in both the diagonal and cross positions. The patterns of these peaks at the same ω_3 are identical regardless of ω_1, and very similar to those at the same frequencies in the temperature difference FTIR spectra (D)&(E). The peak intensity at the same ω_3 varies with the ω_1 value, because the excitation power and optical density of the sample at different ω_1 values are different, leading to different amount of energy deposit into the sample. These are the major features of heat induced peaks in 2D IR measurements. These heat effects can also be explained with Feynman diagrams. The heat induced bleaching is from diagrams $R_{2'}$ and $R_{4'}$, similar to the chemical exchange, because no matter the bleaching is caused by the decrease of the optical density or the disappearance of an old species induced by heat, the signal is always from the ground state holes at various frequencies. The heat inducing absorption can be from two different reasons. One is that those low frequency modes excited by heat are coupled to the high frequency modes, so that these high frequency modes appear as combination band absorption. The diagrams for this reason are R_{17} and R_{18}. The other reason is that a new species is created by the heat, e.g. H-bond breaking, resulting in a new absorption similar to peaks at $\omega_3 \sim 2680\,\text{cm}^{-1}$ in Figure 2.21(C). The diagrams for this reason are displayed in Figure 2.22.

2.4.2. *Polarisation selective 2D IR data*

2.4.2.1. *Anisotropy*. As discussed above, molecular information can be obtained from the time dependent lineshapes and growth of cross peaks in 2D IR spectra. In addition, the 2D measurements provide another type of important information for the studies of molecular structures and dynamics: anisotropies of vibrational modes, obtained through the polarisation-selective method. In general, each laser pulse used in the MDVS experiments

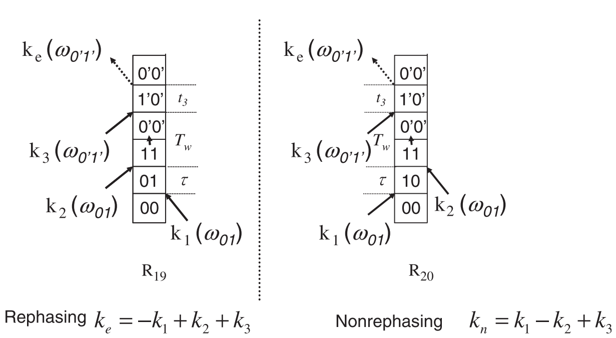

Figure 2.22. Feynman diagrams contributing to the heat induced new absorption. During the T_w period, the relaxation of the 1st excited state of one mode creates a new species at its ground state 0′. The third pulse E_3 produces the new species 0′–1′ absorption.

is a linearly polarised light. Therefore, on one hand, the electric field E prefers to interact with molecules along its vector direction, perpendicular to the direction of light propagation. On the other hand, a vibrational mode of a molecule prefers to absorb light along the vector direction of its transition dipole moment. The probability of exciting a specific vibrational mode by a pulse is thus proportional to the square of the scalar product of the transition dipole moment and the electric field, i.e., $E^2\mu^2\cos^2\theta_0$, with θ_0 being the angle between the electric vector of the laser pulse and the transition dipole moment of the mode. As a consequence, vibrational modes with transition dipole moment parallel to that of the electric field are preferentially excited, and those with transition dipole moment perpendicular to that of the electric field are least excited. Based on this principle, the relative reorientations of molecules or vibrational modes can be directly measured by manipulating the polarisations of the laser pulses in MDVS experiments.

In experiments, the relative molecular orientation is generally characterised with a parameter called anisotropy [103], which is defined as

$$r(t) = \frac{P_\parallel(t) - P_\perp(t)}{P_\parallel(t) + 2P_\perp(t)}, \tag{2.40}$$

where $P_\parallel(t)$ and $P_\perp(t)$ are the signal intensities from experiments with the probe beam ($E_3\&E_{LO}$) is parallel and perpendicular to the pump beam ($E_1\&E_2$) respectively, and t is the waiting time between pump and probe. The numerator of Equation (2.40) counts for the signal difference between the two experiments, and the denominator counts for the total signal in the x, y, and z directions. Assuming that the pump beam propagates along the y-axis, and the z-axis is the direction of electric field, according to the derived 2D IR signal (see Equation (2.27)), we have

$$P_\parallel(t) = P_z(t) = A_0[\vec{z}_{E_{pump}} \cdot \vec{\mu}_{pump}(0)]^2[\vec{z}_{E_{probe}} \cdot \vec{\mu}_{probe}(t)]^2 \tag{2.41}$$

$$P_\perp(t) = P_x(t) = A_0[\vec{z}_{E_{pump}} \cdot \vec{\mu}_{pump}(0)]^2[\vec{x}_{E_{probe}} \cdot \vec{\mu}_{probe}(t)]^2 \tag{2.42}$$

where $A_0 = kE^2_{pump}E^2_{probe}\mu^2_{pump}\mu^2_{probe}$, and k is a constant. E_i is the electric field amplitude. μ_i is the transition dipole moment. $\vec{z}$ and $\vec{x}$ are the unit vectors of the electric fields along the z-axis and the x-axis, respectively. $\vec{\mu}_i$ is the unit vector of the transition dipole moment.

For the diagonal red peaks in 2D spectra, $\hat{\mu}_{pump} = \hat{\mu}_{probe}$ at $t = 0$ because the excited mode is identical to the detected mode ($\omega_1 = \omega_3$). Therefore

$$P_\parallel(0) = A_0\overline{\cos^4(\theta_z)} \tag{2.43}$$

$$P_\perp(0) = A_0\overline{\cos^2(\theta_z)\cos^2(\theta_x)}, \tag{2.44}$$

where θ_z and θ_x are the angles between the directions of transition dipole moment and the electric fields along the z-axis and the x-axis, respectively. The bars denote an ensemble average over all molecules.

According to the classical formula of spherical trigonometry, if the angle between vectors **A** and **B** is θ_1, and that between **A** and **C** is θ_2, the angle θ between **A** and **B** satisfies the following equation:

$$\cos\theta = \cos\theta_1\cos\theta_2 + \cos\psi\sin\theta_1\sin\theta_2, \tag{2.45}$$

where ψ is the angle between planes **AB** and **AC**.

By inserting Equation (2.45) with $\theta = \theta_x$, $\theta_1 = \theta_z$ and $\theta_2 = \pi/2$, Equation (2.44) can be replaced by

$$\begin{aligned} P_{\perp}(0) &= A_0\overline{\cos^2(\theta_z)[\cos(\theta_z)\cos(\pi/2) + \cos\psi\sin(\theta_z)\sin(\pi/2)]^2} \\ &= A_0\overline{\cos^2(\theta_z)\cos\psi^2\sin(\theta_z)^2} = A_0\overline{\cos^2(\theta_z)\sin(\theta_z)^2}/2. \end{aligned} \tag{2.46}$$

All values of ψ are equiprobable for randomly oriented molecules, thus we have $\overline{\cos\psi} = 0$ and $\overline{\cos^2\psi} = 1/2$.

If the distribution of molecules that contribute to the signal is isotropic, we can calculate

$$\overline{\cos^4\theta_z} = \frac{1}{2}\int_0^{\pi} \cos^4\theta_z \cdot \sin\theta_z \, \mathrm{d}\theta_z = 1/5, \tag{2.47}$$

$$\overline{\cos^2\theta_z \sin^2\theta_z} = \frac{1}{2}\int_0^{\pi} \cos^2\theta_z \sin^2\theta_z \cdot \sin\theta_z \, \mathrm{d}\theta_z = 2/15. \tag{2.48}$$

Finally, by substituting Equations (2.47) and (2.48) into Equations (2.43) and (2.46), we get

$$r(0) = r_0 = \frac{P_{\parallel}(0) - P_{\perp}(0)}{P_{\parallel}(0) + 2P_{\perp}(0)} = \frac{2}{5}. \tag{2.49}$$

$r_0 = 0.4$ is the theoretical value when we measured the anisotropy of the diagonal peak at time $t = 0$, when no dynamics have occurred.

For the anisotropy of cross peaks or the 1–2 transition peaks in 2D spectra at $t = 0$, Equations (2.43) and (2.44) can be rewritten as

$$P_{\parallel}(0) = A_0\overline{\cos^2(\theta_z)\cos^2(\theta'_z)} \tag{2.50}$$

$$P_{\perp}(0) = A_0\overline{\cos^2(\theta_z)\cos^2(\theta'_x)} \tag{2.51}$$

where θ_z is the angle between the directions of the dipole moment of the mode excited by the first pulse (E_1) and the electric field along the z-axis. θ'_z and θ'_x are angles between the directions of the dipole moment of the mode interacted with the 3rd pulse (E_3) and electric fields along the z-axis and the x-axis, respectively.

If the angle between the mode excited by E_1 and that interacted with E_3 is defined as θ, we have

$$\begin{aligned} P_{\parallel}(0) &= A_0\overline{\cos^2\theta_z(\cos\theta_z\cos\theta + \cos\psi\sin\theta_z\sin\theta)^2} \\ &= A_0\left(\cos^2\theta\overline{\cos^4\theta_z} + \frac{1}{2}\sin\theta^2\overline{\cos^2\theta_z\sin^2\theta_z}\right) \\ &= \frac{A_0}{15}(2\cos^2\theta + 1), \end{aligned} \tag{2.52}$$

and

$$
\begin{aligned}
P_{\perp}(0) &= \frac{A_0}{2}\overline{\cos^2\theta_z \sin^2\theta_z'} \\
&= \frac{A_0}{2}\overline{\cos^2\theta_z - \cos^2\theta_z\cos^2\theta_z'} \\
&= \frac{A_0}{15}(2-\cos^2\theta). \qquad (2.53)
\end{aligned}
$$

Accordingly, the anisotropy of the cross peak at $t = 0$ is

$$
r(0) = r(\theta) = \frac{P_{\parallel}(0) - P_{\perp}(0)}{P_{\parallel}(0) + 2P_{\perp}(0)} = \frac{3\cos^2\theta - 1}{5}. \qquad (2.54)
$$

This result shows that, the cross angle θ between the transition dipole moments of two normal modes can be directly derived from the anisotropy value $r(\theta)$ of the corresponding cross peaks. We will see in Chapter 5, this conclusion plays a significant role on analyzing the three-dimensional molecular conformations. The relative directions of 0–1 and 1–2 transitions of a vibrational mode can also be determined with Equation (2.54) by examining the anisotropy of the diagonal blue peaks (the 1–2 transition peaks) in 2D spectra. For most vibrational modes we have studied so far, within experimental uncertainties, their 0–1 and 1–2 transitions are parallel.

It is worth noting that the dependence of the cross peak anisotropy on the cross angle is not linear (see Figure 2.23). The corresponding slope curve indicates that, the value of the anisotropy is very sensitive to the cross angle at around 45°, which is confirmed by the maximum slope at $\theta = \pi/4$. If the cross angle between two modes is near 0° or 90° where the slope approximates to zero, the anisotropy is not as sensitive to the cross angle. The analysis implies that the method based on Equation (2.54) to determine the cross angle between two vibrational modes has a more precise value for two modes with a 30° ~ 60° cross angle. If two modes are nearly parallel or perpendicular to each other, the experimental result will have a bigger uncertainty.

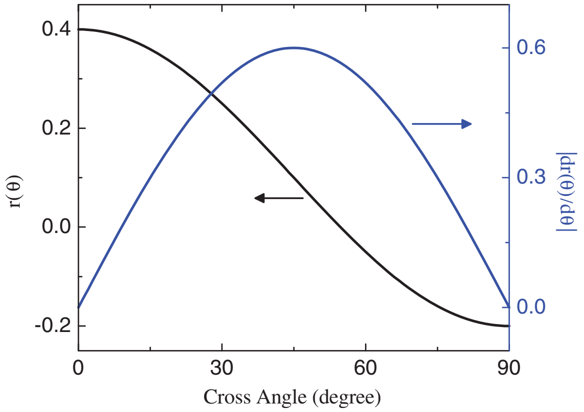

Figure 2.23. The dependence of cross peak anisotropy on the cross angle between two modes (left) and corresponding slope curve (right), according to Equation (2.54).

2.4.2.2. *Molecular rotations and energy transfers.* In condensed phases, some dynamic processes, e.g. molecular rotations and energy transfers from one molecule to another, can lead to a change in the direction of the transition moment of the excited molecules. This can cause the anisotropy defined in Equation (2.40) to decay (to 0 for a complete randomisation of the excited molecules). Based on the molecular mechanism, time dependent polarisation-selective MDVS measurements can provide abundant information on the molecular dynamic behaviors.

The rotations of excited molecules can lead to the randomisation of their orientations, leading to a gradually smaller anisotropy value of the signal. For the simplest but probably the most important case, the isotropic free rotation, the time dependent anisotropy can be simply written as a function of single exponential decay [104]:

$$r(t) = r(0)\exp(-6D_r t) = r(0)\exp(-t/\tau_c), \tag{2.55}$$

where D_r is the rotation diffusion coefficient, and $\tau_c = 1/(6D_r)$ is a rotational time constant. According to the Stokes–Einstein relation:

$$D_r = \frac{RT}{6V\eta}, \tag{2.56}$$

where V is the hydrodynamic molecular volume of the molecule. η is the viscosity of the medium, T is the absolute temperature and R is the gas constant. Although the validity of the Stokes–Einstein relation is still questionable at the molecular scale, it has been found to work surprisingly well for molecules embedded in a homogeneous liquid [105]. That means, from the time dependent depolarisation of the pump/probe signal, we can obtain information on the molecular motions, which depend on the size and the shape of molecules, and the fluidity of their microenvironment. In addition, the rotation-free pump/probe signal can be simply obtained by $P(t) = P_{\parallel}(t) + 2 \times P_{\perp}(t)$, the intensity of signal in all three directions (x, y and z), which is usually used to estimate vibrational lifetimes of the excited modes.

The vibrational energy transfer from one mode to another mode with a different orientation can also lead to the depolarisation of the pump/probe signal. Therefore, the vibrational energy transfer rate can also be derived from the anisotropy decay curve acquired from time dependent pump/probe experiments [90,106].

Under the dipole-dipole approximation [106–108], the vibrational energy transfer rate is proportional to the square of the coupling between an energy donor and its acceptor β, which has the form:

$$\begin{aligned}\beta &= \frac{1}{4\pi\varepsilon_0 n^2}\left[\frac{\boldsymbol{\mu}_D \cdot \boldsymbol{\mu}_A}{r_{DA}^3} - 3\frac{(\boldsymbol{\mu}_D \cdot \mathbf{r}_{DA})(\boldsymbol{\mu}_A \cdot \mathbf{r}_{DA})}{r_{DA}^5}\right] \\ &= \frac{1}{4\pi\varepsilon_0 n^2}\frac{\mu_D \mu_A \kappa}{r_{DA}^3},\end{aligned} \tag{2.57}$$

where ε_0 demotes vacuum permittivity, n is the local refractive index of the media, r_{DA} is the distance between two modes, μ_D and μ_A are transition dipole moments of the pumping mode and probing mode, respectively, and κ is the orientational factor:

$$\begin{aligned}\kappa &= \cos\theta_{DA} - 3\cos\theta_D\cos\theta_A \\ &= \sin\theta_D\sin\theta_A\cos\varphi - 2\cos\theta_D\cos\theta_A\end{aligned} \tag{2.58}$$

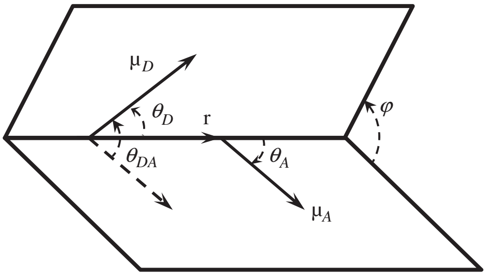

Figure 2.24. Geometric angles involved in the definition of the orientation factor.

with θ_{AD} is the angle between the two transition dipole moments, θ_A and θ_D are the angles between each transition moment and the vector connecting them, respectively, φ is the angle between the projections of the transition moments on a plane perpendicular to the line through the centers, as shown in Figure 2.24.

For simplicity, the molecules are assumed to be immobile and with a random distribution. Neglecting the effects of rotational diffusion and only considering the situation at $t = 0$, where the excited state is assumed to remain localised on the originally excited molecule, the probability for energy transfer between a pair of donor and accepter depends on θ_D, θ_A and φ according to

$$W(\theta, \omega) \propto \kappa^2 = (\sin\theta_D \sin\theta_A \cos\varphi - 2\cos\theta_D \cos\theta_A)^2. \tag{2.59}$$

After one energy transfer process, the transition dipole moment of the excited mode rotates by an angle θ_{DA} (in Figure 2.24), because the energy has transferred from the donor to the acceptor, resulting in an anisotropy

$$\begin{aligned} r_{ET}(\theta_D, \theta_A, \varphi) &= (3\cos^2\theta_{DA} - 1)/5 \\ &= [3(\sin\theta_D \sin\theta_A \cos\varphi + \cos\theta_D \cos\theta_A)^2 - 1]/5, \end{aligned} \tag{2.60}$$

according to Equation (2.54). As a result of random distribution, the angular jumps of θ_D, θ_A and θ_{DA} have equal probability in all the orientations. Therefore, taking all energy transfer probability into account, the final anisotropy of the pump/probe signal after the transfer can be derived as:

$$\begin{aligned} r_{ET} &= \frac{\int_0^{2\pi} \mathrm{d}\varphi \int_0^{\pi} \mathrm{d}\theta_A \int_0^{\pi} W(\theta_D, \theta_A, \varphi) r_{ET}(\theta_D, \theta_A, \varphi) \sin\theta_D \sin\theta_A \, \mathrm{d}\theta_D}{\int_0^{2\pi} \mathrm{d}\varphi \int_0^{\pi} \mathrm{d}\theta_A \int_0^{\pi} W(\theta_D, \theta_A, \varphi) \sin\theta_D \sin\theta_A \, \mathrm{d}\theta_D} \\ &= 0.016 = 0.04 \cdot r_0 \end{aligned} \tag{2.61}$$

The result shows that a single resonance energy transfer step can reduce the anisotropy to 4% of the initial value. In other words, the anisotropy decay rate constant is about 96% of the energy transfer rate constant. The common approach is to disregard this 4% difference and take both constants to be the same.

2.5. *Applications of MDVS*

The MDVS methods detect the nuclear degrees of freedom of molecules. The experimental observables are determined by the nuclear coordinates. Therefore, any molecular structural information and dynamic processes related to the nuclear motions, e.g. chemical bonds or H-bonds transformations, molecular and chemical bond rotations, and vibrational energy flows, can be in principle investigated by the methods. The methods have been extensively applied in studies of water, aqueous solutions, proteins, peptides, nanomaterials, chemical reactions, H-bond dynamics, vibrational dynamics, molecular isomerisations, lipids, and surfaces.

The past and ongoing research in our group asks a simple question: can MDVS become a self-consistent structural tool for resolving three-dimensional molecular conformations similar to XRD or NMR?

To become such a tool, MDVS needs to have the capability to determine both the relative chemical bond orientations and the absolute chemical bond distances. In principle, if the cross angle between the transition dipole moments of any two normal modes in a molecule can be determined, these vibrational angles can then be translated into the cross angle between any two bonds even if the vibrations are not along the bond directions. The relative orientations of the chemical bonds of this molecule, which molecular conformations are referred to, are determined by these bond angles. The absolute distance between any two chemical bonds can also be determined by measuring the vibrational energy transfer kinetics between two vibrational modes associated with these bonds, if the general correlations between molecular structures and energy transfer kinetics are known. Here, we want to emphasize that the vibrational energy transfer method does not require a structure-disturbing labeling which is usually required in electronic energy transfer measurements. The chemical bonds themselves are chromophores. If it can work, it should be able to detect distances with a spatial resolution at the order of bond lengths, $1\sim2$ angstrom.

Our research has followed these two directions: (1) to explore the nature of vibrational energy transfers, and the potential of using vibrational energy transfers as a ‘‘molecular ruler’’ to measure molecular distances; and (2) to explore the potential of determining 3D molecular conformations in various condensed phases by measuring vibrational cross angles. In chapter 3 and 4, we will introduce our work in searching for the general correlations between vibrational energy transfer kinetics and molecular structural parameters, and the applications of vibrational energy transfers in studies of ion clustering, ion/ion interactions, and ion/molecule interactions in liquids. In chapter 5, applications of our multiple-mode approach in determining 3D molecular conformations in liquids, solids, interfaces are introduced.

3. Mode-specific intermolecular vibrational energy transfer

Vibrational energy transfer is a critical step of molecular reaction dynamics [109–113]. For example, in condensed phases, whenever a molecular bond is broken, formed, or changed into other conformations, a large part of the energy involved in the processes inevitably comes from or converts into vibrational energy, the dynamics of which has been extensively studied in both theory and experiments for decades [101,114–136]. In addition, intermolecular vibrational energy transfer is also a key part of many important phenomena, e.g., heat transportations and cell signaling. However, quantitative studies on vibrational energy transfer kinetics have proved to be very challenging [137]. One major reason is that in condensed phases, a vibrational energy donor usually has a very large number of acceptors, which can be thousands or even millions. Some of these acceptors are intramolecular, and some are intermolecular. Some acceptors are normal modes which can be straightforwardly predicted, and some are combination bands or overtones which are simply "dark" states. It is therefore very difficult to precisely determine the direct vibrational energy transfer pathway from one mode to another. In addition, infrared laser technology and infrared detection methods were also limiting factors in the studies of vibrational energy transfers. Thus, the general correlation between molecular structures and vibrational energy transfer kinetics was mainly from theoretical studies based on the Fermi goldern ruler approach [137,138]. Almost no experimental results were able to directly examine such a theoretical prediction. It is therefore not surprising that different from electronic energy transfers which have been widely used in various fields to probe molecular interactions, vibrational energy transfers have almost never been used to do similar jobs.

For the purpose of developing our multiple-mode multiple-dimensional vibrational spectroscopy to become a structural tool, the first step of our experiments is to explore the general correlation between molecular structures and vibrational energy transfer kinetics. To address problems associated with vibrational energy studies mentioned above, we adopted several approaches: (1) to avoid the many-acceptor problem, we chose to study mode-specific vibrational energy transfer; (2) to relieve the problem that the energy donor overlaps in frequency with and strongly couples to a combination band involving the acceptor, we studied intermolecular energy transfers rather than intramolecular transfers; (3) to increase the intermolecular energy transfer efficiency, we used the heavy atom approach to block intramolecular energy transfer pathways [70]; and (4) to increase the very weak mode-specific energy transfer signal, we designed the high power ps/fs hybridisation laser setup to make sure the signal/noise ratio is sufficiently high.

A series of experiments was designed to address how and why the vibrational energy of one mode on one molecule transfers to another mode on another molecule, e.g., we measured the vibrational energy transfer from the first excited state of the C-D stretch of deuterated chloroform ($DCCl_3$) to the 0–1 transition of the CN stretch of phenyl selenocyanate (C_6H_5SeCN) in their 1:1 liquid mixture [70], as well as the vibrational energy transfers between the CN stretch of SCN^- and the $^{13}C^{15}N^-$ stretch in $KSCN/KS^{13}C^{15}N$ mixed aqueous solutions [97]. From the experiments, a quantitative analytical equation which describes the correlation between the vibrational energy transfer rate constant and the molecular structural parameters was derived.

In this chapter, we first use the work on the $C_6H_5SeCN/DCCl_3$ liquid mixture as an example to demonstrate how the intermolecular mode-specific vibrational energy transfer kinetics are investigated and analyzed [70], and then how the analytical equation was derived and experimentally examined [96,97].

3.1. *Phenyl selenocyanate and deuterated chloroform mixture*

The first system we studied is a $C_6H_5SeCN/DCCl_3$ liquid mixture with a molar ratio 1:1. The FTIR spectra of pure C_6H_5SeCN liquid, pure $DCCl_3$, and their mixture are shown in Figure 3.1. As will be discussed in this section, vibrational energy transfer kinetics from the 1st excited state ($2252\,cm^{-1}$) of the C-D stretch of $DCCl_3$ to excite the 0–1 transition ($2155\,cm^{-1}$) of the CN stretch of C_6H_5SeCN in the mixture can be directly determined [70].

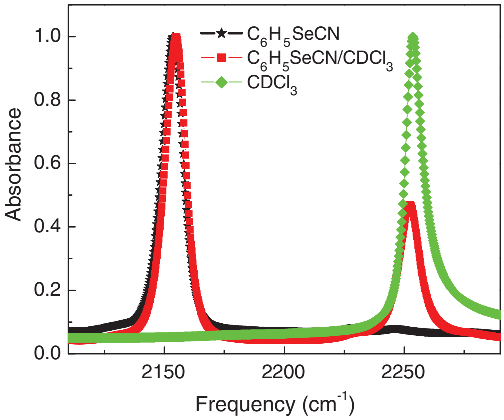

Figure 3.1. (Colour online) FTIR spectra of pure C_6H_5SeCN liquid, pure $DCCl_3$, and their mixture with a molar ratio 1:1. The peak at $2155\,cm^{-1}$ is the CN stretch mode of the C_6H_5SeCN molecule, and the peak at $2252\,cm^{-1}$ is the CD stretch mode of the $DCCl_3$ molecule. Reprinted with permission from [70]. Copyright 2010, American Institute of Physics.

3.1.1. *Basis of observing the energy transfer*

The long vibrational lifetime of the CN stretch 1st excited state of the SeCN group and the relatively strong hydrogen-bond between the C-D and CN are the main molecular mechanism for us to experimentally observe the direct energy transfer from the CD stretch to the CN stretch.

To retain the vibrational excitation in the donor or the acceptor or both as long as possible, we need their vibrational lifetimes to be as long as possible. According to the arguable "heavy atom effect", heavy atoms can block intramolecular vibrational energy transfer from one mode to others in some cases of gas phase [139–141] and condensed phases [59,142,143]. We therefore chose and designed molecules with heavy atoms, e.g. Si, S and Se, and measured vibrational lifetimes of these molecules. These heavy atoms were found indeed to be able to effectively block vibrational energy from relaxing to other modes inside the molecule in nonpolar solvents for some molecules. For example, as shown in Figure 3.2, the CN stretch lifetimes of $C_2H_5CH_2CN$, C_2H_5SCN, and C_2H_5SeCN in CCl_4 solutions are about 5.5 ps, 84 ps and 282 ps, respectively. The results clearly show that heavier atoms are better energy blockers ($Se > S > C$). The longer vibrational lifetime means that more vibrational energy will be transferred to intermolecular modes instead of intramolecular acceptors. Note, the heavy atom effect does not always hold as we experimentally demonstrated [70].

On the other hand, DFT calculations [70] (Figure 3.3) show that the CD group of $CDCl_3$ and the CN group of C_6H_5SeCN can form a relatively strong hydrogen-bond in the mixed solution, which is also a key role for vibrational energy to transfer between CN and CD.

3.1.2. *Detailed analyses of 2D IR spectra*

Figure 3.4 displays waiting time dependent 2D IR spectra and an energy level diagram showing the peak origins in the spectra of a C_6H_5SeCN/Cl_3CD (1/1 molar ratio) mixed liquid at room temperature [70]. In the following, we will describe in details how each peak

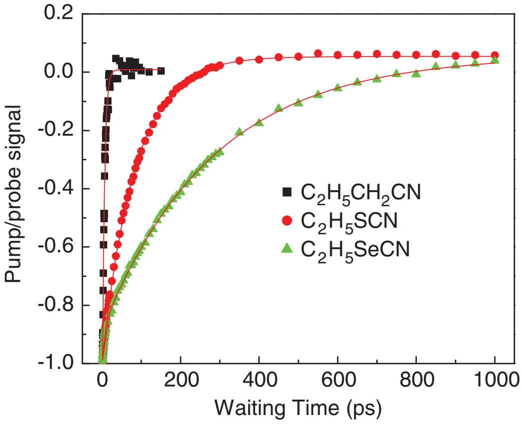

Figure 3.2. (Colour online) Rotation-free pump/probe CN 1–2 transition data (points are data. Lines are fits) of $C_2H_5CH_2CN$ (~2252 cm^{-1}), C_2H_5SCN (~2156 cm^{-1}), and C_2H_5SeCN (~2155 cm^{-1}). Reprinted with permission from [70]. Copyright 2010, American Institute of Physics.

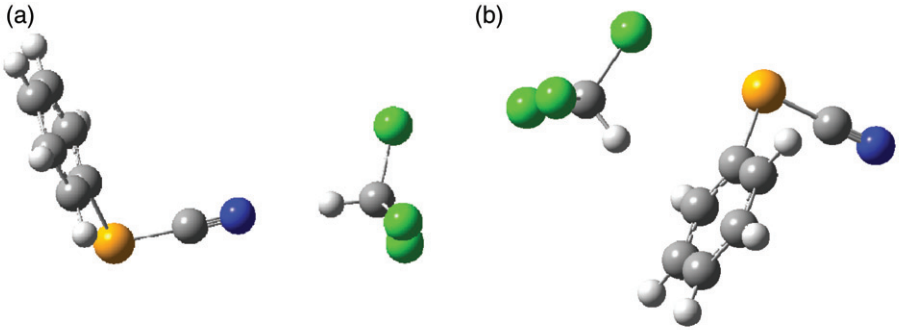

Figure 3.3. (Colour online) Two calculated H-bonds between C_6H_5SeCN and $DCCl_3$ in gas phase. (a) is more stable than (b) by ~ 1.53 kcal/mol. Reprinted with permission from [70]. Copyright 2010, American Institute of Physics.

grows in the spectra, and how the vibrational energy transfer of CD to CN between the two molecules can be revealed by the peak growths and decays in the 2D IR spectra.

At short waiting times, e.g. 1 ps, only two red/blue peak-pairs show up in the spectrum. Peak 1 and 2 belong to the CD 0–1 transition and 1–2 transition, respectively, while Peak 3 and 4 belong to the CN 0–1 transition and 1–2 transition, respectively. It also shows that the CD peak pair decays much faster than the CN peaks, indicating a much shorter lifetime of CD stretch (~8.6 ps) than that of the CN stretch (~330 ps).

Some peaks grow in on the off-diagonal positions with the increase of waiting time, e.g. Peaks 5, 6, 7, 8, and 9. As discussed in the previous chapter, the growth of these cross peaks is one major feature of 2D IR spectra, which can be utilised to analyse detailed molecular structures and dynamics. In general, cross peaks can be induced by several molecular phenomena: vibrational coupling [12,48,144], intramolecular vibrational energy transfers [19,33,48,136], intermolecular vibrational energy and heat transfers [98], molecular transformations [4,33,34]. In the case studied here, we will demonstrate that

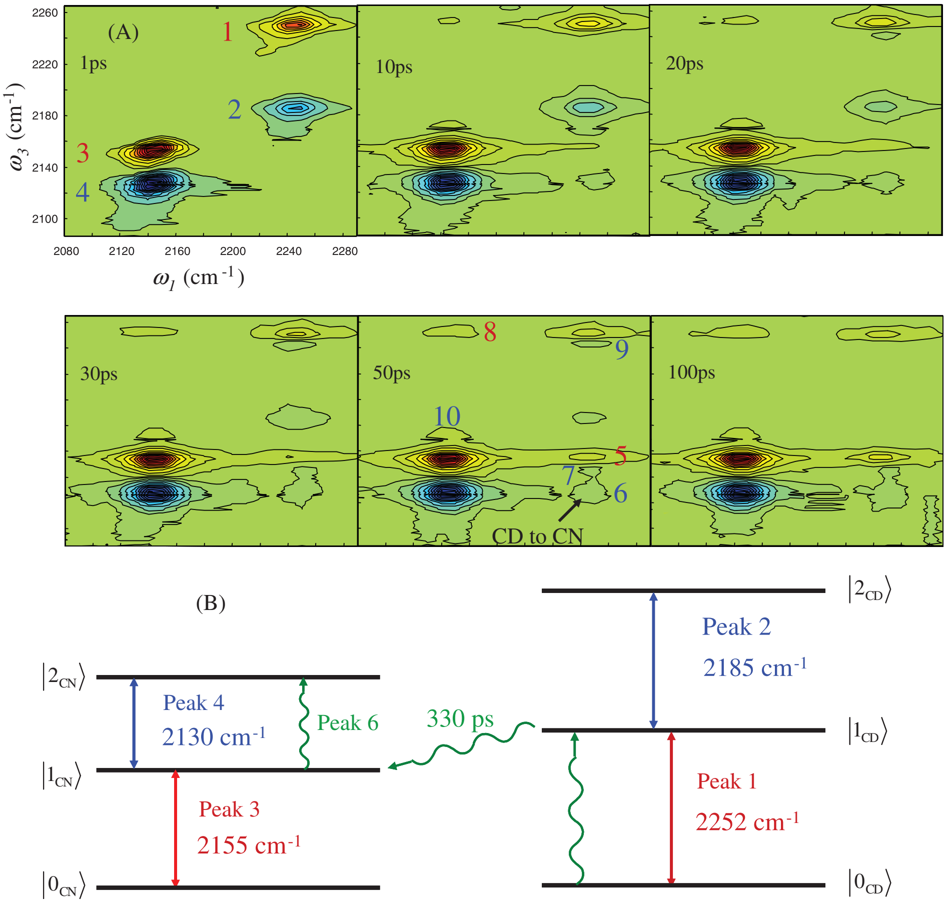

Figure 3.4. (Colour online) (A) Waiting time dependent 2D IR spectra of a C_6H_5SeCN/Cl_3CD (1/1 molar ratio) mixed liquid at room temperature. (B) Energy level diagram showing the origins of Peaks 1, 2, 3, 4, and 6. The wavy curves demonstrate how energy flows from CD to CN to produce the energy transfer peak 6. In 2D IR spectra, each contour represents 10% intensity increase except the smallest two (5% and 1% of the maximum intensity, respectively. In the 1ps panel, the smallest contour is 5%.). Reprinted with permission from [70]. Copyright 2010, American Institute of Physics.

the molecular phenomena responsible for the growth of the cross peaks in Figure 3.4(A) can be mainly attributed to the intermolecular vibrational energy and heat transfers.

The red cross peak 8 is mainly caused by the CD absorption transparency induced by heat from the vibrational relaxation of CN. The peak's excitation frequency ω_1 is $2155\,\mathrm{cm}^{-1}$, representing the heat coming from the CN 0–1 transition relaxation. Its detection frequency ω_3 is $2252\,\mathrm{cm}^{-1}$, representing the signal coming from the CD stretch. The Feynman diagrams describing the light/material interaction origin for this peak are similar as $R_{2'}$ and $R_{4'}$ shown in Figure 2.13. It is also possible that peak 8 is from the mode specific vibrational energy transfer from CN to CD. However, very little blue cross peak 10 at ($\omega_1 = 2155\,\mathrm{cm}^{-1}$, $\omega_3 = 2185\,\mathrm{cm}^{-1}$) observed means that the contribution to the overall intensity peak 8 of this possibility is very small. The contribution of energy exchange among low frequency modes similar to that of the acetonitrile/benzonitrile system in chapter 2 is also small, because no blue peaks underneath of peak 8 is observed.

Blue cross peak 6 is mainly from the mode specific vibrational energy transfer from CD to CN. Its excitation frequency is the CD 0–1 transition frequency $2252\,\mathrm{cm}^{-1}$, indicating that the energy is from the CD excitation. Its detection frequency is the CN 1–2 transition frequency $2130\,\mathrm{cm}^{-1}$, indicating that the energy has transferred to the CN stretch 1st excited state. Feynman diagrams describing the light/material interaction origin for this peak are $R_{6'}$ and $R_{7'}$ shown in Figure 2.15. However, two other molecular processes can also produce cross blue peaks at positions close to peak 6: intermolecular heat induced absorption and vibrational relaxation induced combination band absorption [33,98,136]. Typically these two processes induce a relatively small frequency shifts from the cross red peak. Blue peak 7 growing in from panel 20ps to 100ps in Figure 3.4(A) is from these effects.

The red cross peak 5 has several origins: heat induced transparency, possible vibrational relaxation induced ground state bleaching [98], and the mode specific vibrational energy transfer from CD to CN. Heat induced transparency can be justified by the temperature dependent FTIR spectra. The mode specific vibrational energy transfer is confirmed by the appearance of the blue cross peak 6, because there must be a 0–1 transition Peak 5, corresponding to the 1–2 transition peak 6 induced by the energy transfer. The vibrational relaxation inducing ground state bleaching is difficult to experimentally justify since the vibrational lifetime of CN is longer than 300 s and the diagonal CN peaks 3 and 4 don't show clear frequency shifts with time. All these contributions add up together making its amplitude bigger than any cross blue peak underneath of it.

A small blue peak 9 grows in and then disappears just underneath of the CD 0–1 transition red peak in the 2D IR spectra. This peak is a typical intramolecular vibrational relaxation induced combination band absorption, which has been observed in many systems with pump/probe and 2D IR methods [33,98,99,126,136]. The origin of this peak can be explained as the following: The excitation of CD stretch relaxes to other modes which are strongly coupled to the CD stretch inside the molecule. While these modes are excited through accepting the energy from the CD stretch, they form a new combination band with the CD stretch 0–1 transition. Light at the combination band frequency (a little lower than the CD 0–1 transition) is then absorbed by this new band. Feynman diagrams describing the light/material interaction origin for this peak are depicted in the Figure 3.5.

From the above analysis, we know that only blue cross peak 6 is purely caused by the vibrational energy transfer from CD to CN. Other cross peaks are from various contributions. Therefore, the growth of peak 6 is used to analyse the CD to CN energy transfer kinetics.

3.1.3. *Kinetic analysis of energy transfer from CD to CN*

According to the analysis above, the appearance and growth of the blue cross peak 6 in Figure 3.4 confirms mode specific vibrational energy transfer from CD to CN. The energy transfer efficiency is somehow unexpectedly low, only $\sim 2\%$, indicating relatively slow energy transfer kinetics from CD to CN.

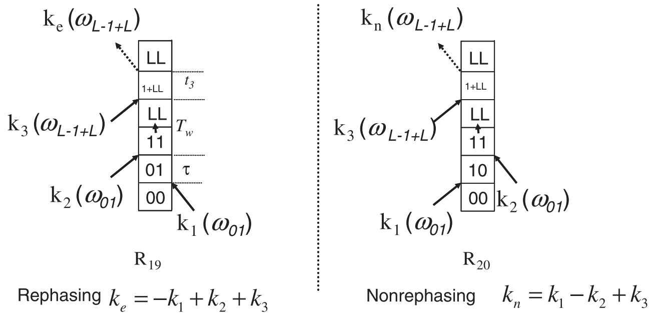

Figure 3.5. Feynman diagrams showing the origins of vibrational relaxation induced blue peak 9. The first interaction frequency ω_{01} is the CD 0–1 transition frequency 2252 cm^{-1}, and the emission frequency ω_{L-1+L} is the CD combination band transition frequency 2241 cm^{-1}. During the population period, the excitation of CD stretch (11) transfers to other mode(s) LL strongly coupled to it. The third interaction excites the CD 0–1 transition again while LL is (are) on the 1st excited state. The 0–1 transition frequencies are different, depending on whether LL is (are) on the ground state.

$$\xleftarrow{k_{CD}} CD \underset{k_{CN\to CD}}{\overset{k_{CD\to CN}}{\rightleftarrows}} CN \xrightarrow{k_{CN}},$$

Scheme 3.1. Kinetic model of vibrational energy exchange between CD and CN.

To quantitatively analyse the mode specific energy transfer kinetics, an appropriate kinetic model is needed. Two issues need to be clarified before we introduce the model. First, most molecules in $C_6H_5SeCN/DCCl_3$ mixture are always H-bonded due to their big formation energy $\Delta E = -5.36$ kcal/mol from DFT calculations. It means that there is always one major H-bonded state in the system, and most of the vibrational energy transfers occur when two molecules are H-bonded. Second, it can be estimated that the molecules that are not H-bonded will dissociate and reform within a few ps [59], which is much faster than the energy transfer studied here. Besides, the transition dipole moment of the free CD is much smaller than the bonded one, which makes sure that the energy transfer signal experimentally observed is mainly from the bonded species. Therefore, it is reasonable to assume that the measured energy transfer rate is mainly from the bonded species.

Based on these discussions, a simple model can be constructed, where CD and CN can exchange vibrational energy, and they also decays with their own lifetimes and possible H-bond dynamics. It can be illustrated in the following scheme,where k_{CD} and k_{CN} are the vibrational lifetimes of CD and CN, respectively. $k_{CD\to CN}$ and $k_{CN\to CD}$ are the energy exchange rate constants, of which the ratio $\frac{k_{CN\to CD}}{k_{CD\to CN}} = e^{-\frac{2252-2155}{200}} = 0.62$ is determined by the detailed balance principle. Two differential equations are obtained from Scheme 3.1:

$$\frac{\mathrm{d}[CD]}{\mathrm{d}t} = -k_{CD\to CN}[CD] - k_{CD}[CD] + k_{CN\to CD}[CN] \tag{3.1}$$

$$\frac{\mathrm{d}[CN]}{\mathrm{d}t} = -k_{CN\rightarrow CD}[CD] - k_{CN}[CN] + k_{CD\rightarrow CN}[CD]. \tag{3.2}$$

In the two equations, for the energy transfer process of CD to CN, the time dependent CD and CN populations [CD] and [CN] are provided by the normalised intensities of the CD 1–2 transition peak 2, and the CD to CN energy transfer peak 6, respectively. For the energy transfer process of CN to CD, [CN] is the normalised intensity of the CN 1-2 transition peak 4, and [CD] is the normalised intensity of the CN to CD transfer peak 10. The normalisation of peak 6 is obtained by dividing its intensity by the square root of the intensity ratio ($I_{CN}/I_{CD} = 2.5$) of the CN and CD diagonal peaks at the earliest waiting time. The normalisation of peak 10 is to multiple the same constant. The normalisation is to compensate for the difference between the transition dipole moments of the CD stretch and the CN stretch. All the experimental data are rotation free ($P_{\parallel}(t) + 2P_{\perp}(t)$).

According to the model, there are four parameters k_{CD}, k_{CN}, $k_{CD\rightarrow CN}$ and $k_{CN\rightarrow CD}$ need to be determined. k_{CD} and k_{CN} can be independently constrained in a small range by experiments. Although the vibrational lifetimes of the CD and CN, i.e. k_{CD} and k_{CN} can't be predetermined in their pure liquids, because different solvents can change the lifetimes substantially. However, they must be very close to their apparent lifetimes (the rotation-free decay time constants of their 1–2 transition peaks in Figure 3.4 (A)), because the vibrational energy involved in the mode specific vibrational exchange is only $\sim 2\%$ of the initial excitation energy. Therefore, during the calculation, we used $k_{CD} = 8.6\,\mathrm{ps}$ and $k_{CN} = 330\,\mathrm{ps}$ as initial input values and allowed them to vary at most 20%. Moreover, from experimental data and theory by Kenkre *et al.* [116] or the detailed balance principle, we also have the relationship: $k_{ba} = 0.62k_{ab}$. With all these constraints, there is only one unknown parameter in Equations (3.1) and (3.2). Calculations based on the equations and experimental results yield $1/k_{CD\rightarrow CN} = 320\,\mathrm{ps}$.

The calculations fit experimental results reasonably well, but it obviously misses the early intensity decay part of peak 4. This is because the apparent vibrational lifetime of CN is not a rigorous signal exponential, but a bi-exponential with $\sim 10\%$ fast component of $\sim 12\,\mathrm{ps}$ and $\sim 90\%$ slow component of $\sim 400\,\mathrm{ps}$ in the mixture. Therefore, we constructed another kinetic model to analyze the data based on this CN bi-exponential lifetime. The core of the new model is identical to Scheme 3.1. The only difference is that we separate the C_6H_5SeCN into two subgroups. The weighing of each subgroup is determined by the prefactors of the bi-exponential. Each subgroup has a single-exponential-decay lifetime time. Each can exchange energy with CD, but the subgroups can't exchange energy with each other (this follows the assumed physical picture of biexponential: the sub-components can be considered as independent species). Following this new model, calculations fit experimental results much better, as shown in Figure 3.6 [70], with the energy transfer rate: $k_a = 1/8.6\,(\mathrm{ps}^{-1})$, $k_{bfast} = 1/11.5\,(\mathrm{ps}^{-1})$, $k_{bslow} = 1/900\,(\mathrm{ps}^{-1})$, $k_{ab} = 1/330\,(\mathrm{ps}^{-1})$ and $k_{ba} = 1/532\,(\mathrm{ps}^{-1})$.

The results show that, despite the relatively strong interaction between the energy donor (CD) and acceptor (CN), the energy transfer efficiency is very low, only $\sim 2\%$, with the energy transfer rate constant slower than 300 ps. The low efficiency is probably due to the short vibrational lifetime of the donor ($\sim$9 ps) and the slow energy transfer rate ($\sim$330 ps), and the slow transfer rate is partially caused by the big energy mismatch ($2252-2155 = 97\,\mathrm{cm}^{-1}$) between the donor and acceptor.

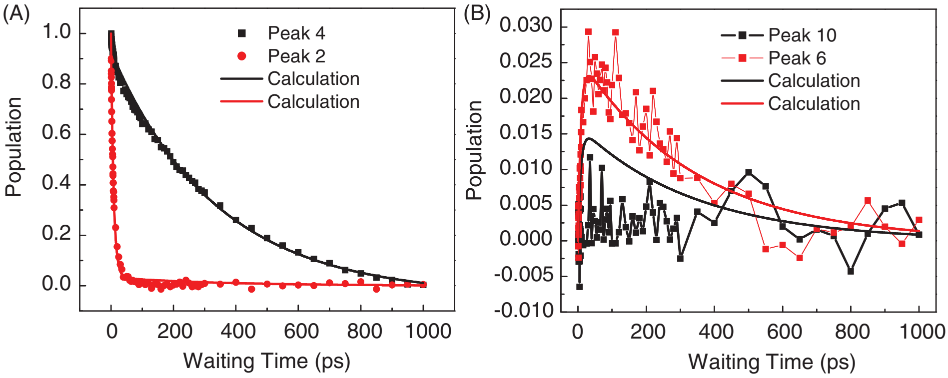

Figure 3.6. (Colour online) Intensities of Peaks 2, 4, 6, and 10 in figure 3.4(A) and calculations based on the bi-exponential model. The CD to CN vibrational energy transfer time constant is 330 ps. The up-pumping energy transfer from CN to CD is slower. Its time constant is 532 ps. The results are within calculation uncertainties of the single exponential model calculations. Reprinted with permission from [70]. Copyright 2010, American Institute of Physics.

3.2. *An analytical equation for the intermolecular vibrational energy transfer*

For the $C_6H_5SeCN/DCCl_3$ mixed solution [70], the coupling strength between the energy donor CD and accepter CN was estimated to be 9.7 cm^{-1} from the exciton model to be descried in the following, with an energy mismatch 97 cm^{-1}, which results in a very slow energy down-flow time constant, 330 ps. In another system, the $KSeCN/D_2O$ mixed solution [96], the coupling strength between the donor, the OD stretch of D_2O and a combinational band of $SeCN^-$ which is on resonance with OD, and the acceptor, the CN stretch of $SeCN^-$, is 175 cm^{-1}, and the donor/acceptor energy mismatch 560 cm^{-1}. The energy transfer time constant from the donor to the acceptor is fast, ~20 ps. Comparison between these two systems shows a qualitative correlation: a stronger coupling produces a faster energy transfer. The big energy mismatch seems to have no significant effect on energy transfer rate. However, when the donor and acceptor are almost on resonance (mismatch $< 30\,cm^{-1}$), the energy transfer time constants can be fast, ~20~40 ps, even with a small coupling (probably $< 18\,cm^{-1}$) [98,126]. These observations raise an interesting question: how are the energy transfer rate, coupling strength and energy mismatch correlated? In the following, we use an approximate equation derived from the Landau–Teller formula [145–149] to address this issue.

3.2.1. *Derivation of the energy transfer rate equation*

The energy transfer rate from vibrational state *i* to state *j* can be described from the Fermi's golden rule as [96,146]

$$k_{ij} = \gamma_{ij} \int_{-\infty}^{\infty} \mathrm{d}t \exp(i\omega_{ij}t) \left\langle \frac{1}{2} \delta\beta(t), \delta\beta(0)_{+} \right\rangle, \tag{3.3}$$

where

$$\gamma_{ij} = \frac{1}{1 + \exp\left(-\frac{\hbar\omega_{ij}}{kT}\right)} \tag{3.4}$$

counts for the detailed balance. ω_{ij} is the energy difference between states i and j. $\delta\beta(t)$ is the time dependent vibrational coupling between the two states as modulated by the bath. $\langle \frac{1}{2}\delta\beta(t), \delta\beta(0)_{+}\rangle$ can be replaced with a classical correlation function [150]. If we assume this correlation function to be a single exponential with a coupling correlation time constant τ_c, and further assume that τ_c is the spectral diffusion time, because the spectral diffusion time characterises the evolution of solvent configurations and the fluctuation of vibrational coupling is largely caused by the molecular motions of the solvent, Equation (3.3) can be rewritten as

$$k_{ij} = \gamma_{ij}\langle\delta\beta^2\rangle\frac{\tau_c^{-1}}{\tau_c^{-2}+\omega_{ij}^2}. \tag{3.5}$$

If we further assume that the fluctuation of vibrational coupling $\delta\beta$ is equal to the average coupling strength $\langle\beta\rangle$ and $\langle\beta^2\rangle = \langle\beta\rangle^2$, Equation (3.5) becomes

$$k_{ij} = \frac{1}{1+\exp\left(-\frac{\hbar\omega_{ij}}{kT}\right)}\langle\beta\rangle^2\frac{\tau_c^{-1}}{\tau_c^{-2}+\omega_{ij}^2}, \tag{3.6}$$

where τ_c^{-2} is in energy unit to match that of ω_{ij}^2. For $\tau_c = 2\,\text{ps}$, $\tau_c^{-1} = 16.7\,\text{cm}^{-1}$.

For the resonant energy transfer condition ($\omega_{ij} = 0$), Equation (3.6) becomes

$$k_{ij} = \frac{1}{2}\langle\beta\rangle^2\frac{\tau_c^{-1}}{\tau_c^{-2}}, \tag{3.7}$$

which can also be directly derived from the 1st order perturbation [151]:

$$\langle i|T(t,0)|f\rangle = -\frac{i}{\hbar}\int_{t_0}^{t}\langle i|V(t')|f\rangle e^{-i\omega_{if}t'}\mathrm{d}t', \tag{3.8}$$

where i and f denote the initial and final states, respectively, $T(t,0)$ is the transition operator. $V(t')$ is the time dependent coupling. ω_{if} is the energy mismatch of the two states. In our system for the resonant case, $i = f$. $V(t')$ is assumed to be a single exponential decay:

$$V(t') = V \times e^{-t'/\tau}. \tag{3.9}$$

From Equations (3.8) and (3.9), the resonant energy transfer rate equation can be derived:

$$p = \left|\langle i|T(t,0)|f\rangle\right|^2 = \left|-\frac{i}{\hbar}\int_0^t\langle V\rangle e^{-t'/\tau}\mathrm{d}t'\right|^2 = \frac{V^2}{\frac{\hbar^2}{\tau^2}}(1-e^{-t/\tau})^2 = \frac{V^2}{E_\tau^2}(1-e^{-t/\tau})^2, \tag{3.10}$$

where p is the probability of energy transfer, and E_τ is the energy corresponding to the decay time constant τ. The energy transfer rate constant is therefore

$$\begin{aligned} k = \frac{\mathrm{d}p}{\mathrm{d}t} &= \left(\frac{V}{E_\tau}\right)^2\frac{\mathrm{d}(1-e^{-t'/\tau})^2}{\mathrm{d}t} \cong \left(\frac{V}{E_\tau}\right)^2\frac{2}{\tau}\times((1-e^{-t/\tau})\times e^{-t/\tau})_{\max} \\ &= \left(\frac{V}{E_\tau}\right)^2\frac{2}{\tau}\times\frac{1}{4} = \frac{1}{2}\times\left(\frac{V}{E_\tau}\right)^2\times\frac{1}{\tau}. \end{aligned} \tag{3.11}$$

Equation (3.11) is actually identical to that obtained from Equation (3.7) for the resonant case. Therefore, Equation (3.6) should be in principle applicable to both resonant and nonresonant energy transfers.

3.2.2. *Experimental parameters for Equation (3.6)*

It is worth noting that all parameters in the right part of Equation (3.6) are experimentally accessible. Among the four parameters, temperature T and the donor/acceptor energy mismatch ω_{ij} are precise. The determination of spectral diffusion times is straightforward from the evolution of line shape of the diagonal peak in 2D IR spectra: from elongated along the diagonal to round (or the slope is from 45° to 0°) with the increase of time [34,53,152]. And the coupling strength can be estimated from the exciton model [153].

Let us take $C_6H_5SeCN/DCCl_3$ system as an example. For the vibrational energy transfer from the CD stretch 0–1 transition to the CN 0–1 transition process, the coupling between the initial state and the final state $\beta_{CD-CN} = \langle 1_{CD}0_{CN}|V|0_{CD}1_{CN}\rangle = \langle 1_{CD}|V|1_{CN}\rangle$ can be experimentally determined assuming the transition dipole coupling mechanism, based on 2D IR measurements and an excitation exchange model [153]. According to the model [71,133,153], the coupling can be obtained [96] with the following equation

$$\Delta_{CD/CN} = \frac{2\beta^2_{CD-CN}(\Delta_{CD} + \Delta_{CN})}{(\omega_{CD0-1} - \omega_{CN0-1})(\omega_{CD0-1} - \omega_{CN0-1})}. \tag{3.12}$$

All parameters in Equation (3.12) are experimentally determined: anharmonicities of the CD stretch $\Delta_{CD} = \omega_{CD1-2} - \omega_{CD0-1} = 67\,\mathrm{cm}^{-1}$, the CN stretch $\Delta_{CN} = \omega_{CN1-2} - \omega_{CN0-1} = 25\,\mathrm{cm}^{-1}$, and the CD/CN combination band shift $\Delta_{CD/CN} = \omega_{CN0-1} - \omega_{1_{CD}-CD/CN} = 6\,\mathrm{cm}^{-1}$, and their 0–1 transition frequencies $\omega_{CD0-1} = 2252\,\mathrm{cm}^{-1}$, and $\omega_{CN0-1} = 2155\,\mathrm{cm}^{-1}$. With these parameters, we obtained $\beta_{CD-CN} = 18\,\mathrm{cm}^{-1}$. Similarly, the coupling between the donor (OD and the combination band) and the acceptor (CN) in the KSeCN/D_2O system is $\langle\beta\rangle = 200\,\mathrm{cm}^{-1}$.

As all parameters have been determined, energy transfer time constant can be straightforward calculated from Equation (3.6). For the KSeCN/D_2O system, $T = 296\,\mathrm{K}$, $\langle\beta\rangle = 200\mathrm{cm}^{-1}$, $\omega_{ij} = 560\mathrm{cm}^{-1}$, and $\tau_c = 1.9\,\mathrm{ps}$. The energy transfer time constant from OD to CN is calculated to be $1/k_{OD\to CN} = 16\,\mathrm{ps}$. The value is very close to 20 ps, which is experimentally determined. However, for the $CDCl_3/C_6H_5SeCN$ system, $T = 296\,\mathrm{K}$, $\langle\beta\rangle = 18\mathrm{cm}^{-1}$, $\omega_{ij} = 97\mathrm{cm}^{-1}$, and $\tau_c = 1.9\,\mathrm{ps}$. The calculated time constant is 90 ps, which is far from the measured value 330 ps.

As discussed below, this deviation mainly arises from the big uncertainty in the calculations of coupling constants. It can be seen from Equation (3.12), that the determination of the coupling constant requires many experimental parameters and one complicated model, which can introduce a huge uncertainty of the coupling constant. In other words, Equation (3.12) comes from a perturbative limit: eigenvalues instead of values of local modes are used to calculate the "coupling between two normal modes" [153]. Such assumptions will inevitably introduce some uncertainty into the final result. The uncertainty is dependent on the coupling constant. In the $CDCl_3/C_6H_5SeCN$ system, the calculated coupling constant is less than 1% of the individual mode frequency ($2155\,\mathrm{cm}^{-1}$ and $2252\,\mathrm{cm}^{-1}$). Such a small value can have a huge uncertainty because of the assumptions.

Direct diagonalisation of the model Hamiltonian matrix can solve this problem. The detail of the calculation procedure can be found in our previous work [96]. It can provide a more precise coupling constant between the energy donor and acceptor in the local mode basis. With the constraints of refined experimental data, it gives the coupling constants $\beta_{OD/CN} = 175.5 \pm 0.5\,\mathrm{cm}^{-1}$ and $\beta_{CD/CN} = 9.7 \pm 0.2\,\mathrm{cm}^{-1}$ for the two systems studied. For the $D_2O/SeCN^-$ system, this value is only $\sim 12\%$ different from what is obtained from Equation (3.12). However, for the $CDCl_3/C_6H_5SeCN$ system, the difference is more than 40%. With the refined coupling values, we thus obtain $1/k_{OD\rightarrow CN} = 21\,\mathrm{ps}$ and $1/k_{CD\rightarrow CN} = 309\,\mathrm{ps}$ from Equation (3.6), which are very close to experimental results.

In addition, it is also worth noting that the calculated time constants strongly depend on what τ_c is in Equation (3.6). Experimentally we don't have a precise way to define τ_c. There are two main reasons for us to choose $\tau_c = 1.9\,\mathrm{ps}$: one is that it is the turning point of the dynamic linewidth curve [96], the other one is that 1.9 ps is the dissociation time of a H-bond with a dissociation enthalpy $0.3 \sim 0.6$ kcal/mol, which is close to the solvent reorganisation energy (activation energy for spectral diffusion) [32,58,59]. On the theoretical side, the assumptions we make in order to obtain Equation (3.6) can be problematic. It is not clear how the spectral diffusion time is correlated to the vibrational coupling correlation time, especially when the spectral diffusion time is slow (in viscous liquids or solids). It is not clear either how the fluctuation of coupling strength is correlated to the strength itself. The correlations can be system dependent. Therefore, more experimental data are needed to further determine the relationship between the energy transfer rate and the structural parameters.

3.3. *The energy mismatch dependence of the vibrational energy transfer*

As derived in the previous section, the intermolecular mode specific vibrational energy transfers rate can be calculated by Equation (3.6). We have demonstrated that the predictions from Equation (3.6) fit two previously investigated systems reasonably well. However, there are four parameters in Equation (3.6). The dependence of k_{ij} on each parameter has not been experimentally independently investigated. It is not clear whether the consistency between the predictions and the experimental results of the two systems is real or just coincident. In the following two sections, we use isotope-labeled KSCN aqueous solutions as model systems to examine the donor/acceptor energy mismatch and vibrational coupling strength dependences of the vibrational energy transfer rates between the nitrile stretches of the isotope-labeled and unlabeled thiocyanate anions.

In mixed $KSCN/KS^{13}CN$ or $KSCN/K^{13}C^{15}N$ aqueous solutions, vibrational energy can exchange between the nitrile stretches of SCN^- and $S^{13}CN^-$ or between the nitrile stretches of SCN^- and $S^{13}C^{15}N^-$. Anions labeled with different isotopes have different nitrile stretch vibrational frequencies. For example, the CN stretch frequency of SCN^- is $2064\,\mathrm{cm}^{-1}$, that of $S^{13}CN^-$ is $2015\,\mathrm{cm}^{-1}$ (see Figure 3.7(A)), and that of $S^{13}C^{15}N^-$ is $1991\,\mathrm{cm}^{-1}$. The donor/acceptor energy mismatch dependent energy transfer experiments can be achieved by measuring energy exchanges among these species with different isotope-labeled anions. Because the isotope labeling doesn't change the ionic interaction strength, the vibrational coupling strength among the anions remains essentially the same as that among the unlabeled anions.

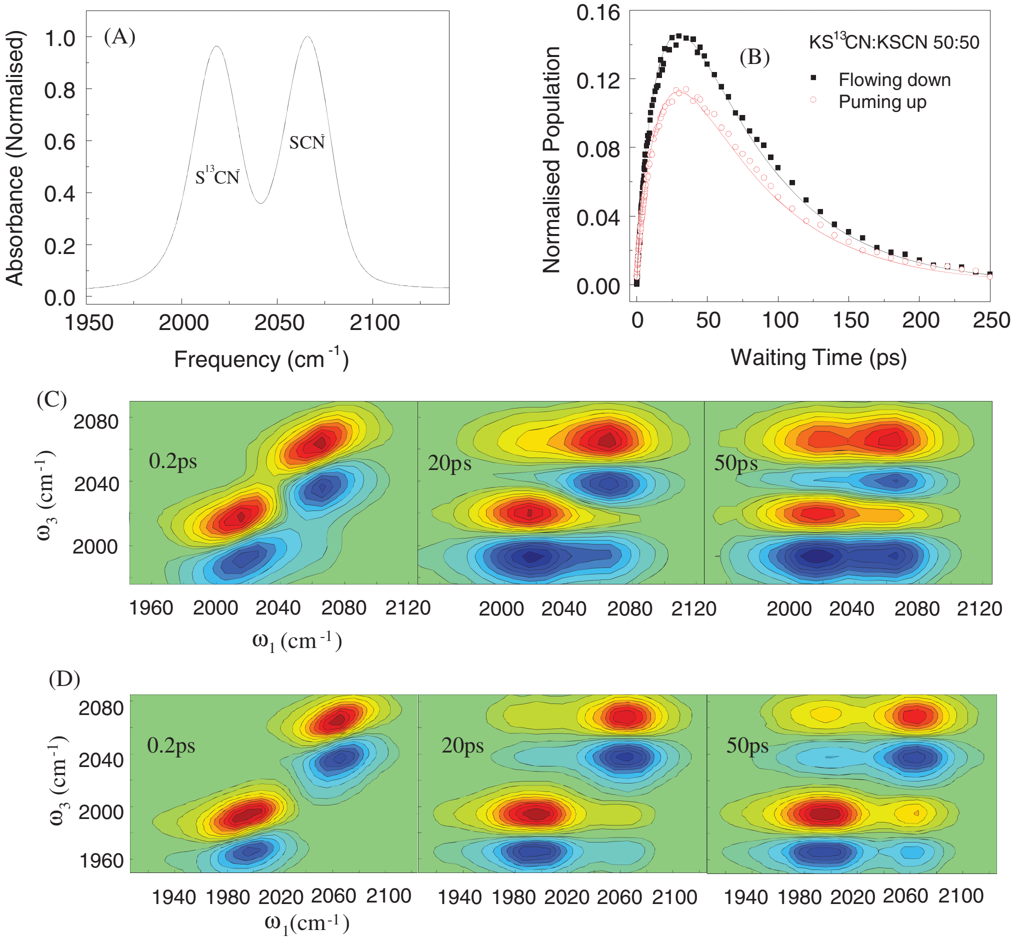

Figure 3.7. (Colour online) (A) FTIR spectra of 1/1 KS^{13}CN/KSCN aqueous solution (10M). (B) Time dependent intensities of energy transfer peaks between S^{13}CN$^-$ and SCN$^-$. Square solid dots are from the flowing-down peaks (SCN$^-$ to S^{13}CN$^-$), and the circle open dots are from the pumping-up peaks (S^{13}CN$^-$ to SCN$^-$). Lines are calculations from the kinetic model. 2D IR spectra of (C) KS^{13}CN/KSCN and (D) KS^{13}C^{15}N/KSCN 10 M aqueous solutions at different waiting times. Reprinted with permission from [97]. Copyright 2011 American Chemical Society.

3.3.1. *Nonresonant energy transfer results*

2D IR spectra of KS^{13}CN/KSCN and KS^{13}C^{15}N/KSCN (1/1 molar ratio) 10 M aqueous solutions at different waiting times are shown in Figure 3.7(C) and (D), respectively [97].

The 2D IR spectra in Figure 3.7 are intuitive, and can be simply explained. At a very short T_w, e.g., 0.2ps, negligible vibrational energy exchange has occurred, so only diagonal peak pairs appear in the 2D spectra. The red peaks are the 0–1 transitions of the CN, ^{13}CN or ^{13}C^{15}N stretch, and the blue peaks are the corresponding 1–2 transitions. After a long waiting period, e.g., $T_w = 50$ ps, additional peak pairs appear on the off-diagonal positions. These peaks arise from the vibrational energy exchange between S^{13}CN$^-$ (or S^{13}C^{15}N$^-$) and SCN$^-$. Each diagonal peak pair and its corresponding cross peak pair along the *y*-axis form an energy donor (diagonal)/acceptor (cross) pair. The relative cross/diagonal peak ratio indicates how fast the vibrational energy transfers from the donor to the acceptor. By comparing Figure 3.7(C) and (D), we can see that the cross peaks of $SCN^-/S^{13}C^{15}N^-$ (energy mismatch $\sim 73\,cm^{-1}$) are obviously smaller than those of the $SCN^-/S^{13}CN^-$ with a smaller mismatch $\sim 49\,cm^{-1}$ at the same waiting time. This simple inspection qualitatively reveals that a system with a bigger energy mismatch has a slower energy transfer rate.

The quantitative analysis of the energy transfer rates of the systems is more complicated than that for the two systems introduced above. It is based on a location-energy-exchange model [90]. In this model, some of the thiocyanate anions ($S^{13}CN^-$ or $S^{13}C^{15}N^-$ or SCN^-) tend to form clusters in the aqueous solution, and the rest anions are separated by water molecules. These two types of anions (not frequency resolvable) are under dynamic equilibrium, i.e., they can exchange locations with each other. The clustered anions can exchange vibration energy with each other because of their close distance, while the separated anion can't transfer vibrational energy to other anions because they are separated by water molecules. The vibrational excitation of each species decays with its own vibrational relaxation rate constant. The details of the model will be elaborated in the next chapter. One point needs to be emphasized here: the assumption of ion clustering is the natural result of the inhomogeneous distribution of solute in a room temperature solution. At room temperature, because of the thermal fluctuation, some ions are always closer to each other while others are well separated in a liquid solution. These closer ions can be considered as clustered in the model. Therefore, it is not necessary that this model can only be applied to or depends on ion clustering.

According to the model, a series of differential equations similar to Equations (3.1) and (3.2) can be derived. Details are in chapter 4. By numerically solving these equations and comparing with the experimental results, the energy transfer rate constants, the equilibrium constant between the clustered and separated anions and the location exchange rate constants can be obtained. For the 1/1 $KSCN/KS^{13}CN$ solution, the energy transfer time constant from SCN^- to $S^{13}CN^-$ is 46 ± 7 ps, and the up-pumping time constant from $S^{13}CN^-$ to SCN^- is 60 ± 8 ps. As shown in Figure 3.7(B), the quantitative kinetic analysis of the $KSCN/KS^{13}CN$ solution based on this location-energy-exchange model describes the experimental data very well. Using the same procedure, for the 1/1 $KS^{13}C^{15}N/KSCN$ solution, the energy transfer time constant from SCN^- to $S^{13}C^{15}N^-$ is 115 ± 10 ps, and the $S^{13}C^{15}N^-$ to SCN^- up-pumping time constant is 164 ± 15 ps. The energy mismatch of nitrile stretch between $KS^{13}C^{15}N$ and KSCN is $73\,cm^{-1}$, bigger than the $49\,cm^{-1}$ between $KS^{13}CN$ and KSCN, and hence slows down the energy transfer for more than two times. The two experiments also directly prove the detailed balance principle: $\frac{k_{up-pumping}}{k_{down-flowing}} = e^{-\frac{\hbar\omega_{ij}}{RT}}$. For the $KSCN/KS^{13}CN$ solution, $\frac{k_{up-pumping}}{k_{down-flowing}} = \frac{46}{60} = 0.77$, and $\frac{k_{up-pumping}}{k_{down-flowing}} = \frac{115}{164} = 0.70$ for the $KSCN/KS^{13}C^{15}N$ solution. These ratios can also be straightforwardly observed from the ratio of the cross peak maxima in Figure 3.7B. Both ratios are perfectly consistent with the detailed balance results based on their energy mismatches $\omega_{SCN-S^{13}CN} = 49\,cm^{-1}$ and $\omega_{SCN-S^{13}C^{15}N} = 73\,cm^{-1}$.

3.3.2. *Resonant energy transfer results*

As shown in chapter 2, the anisotropy decays of the pump/probe or 2D IR signal can be induced by intermolecular resonant vibrational energy transfers. Therefore, the rate of

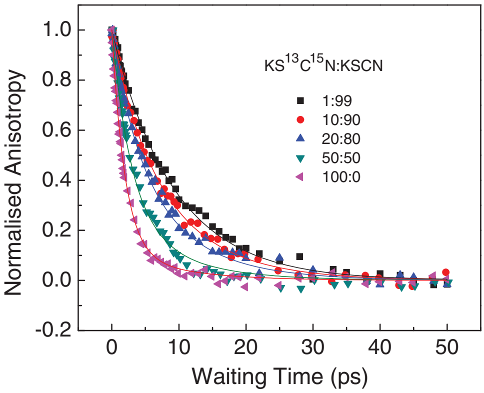

Figure 3.8. (Colour online) The anisotropy decay data (dots) of the $^{13}C^{15}N$ stretch pump/probe signal of $S^{13}C^{15}N^-$ in 10M aqueous solutions with different $KS^{13}C^{15}N$/KSCN molar ratios. Dots are data. Lines are calculations from Equation (3.13). Reprinted with permission from [97]. Copyright 2011 American Chemical Society.

resonant energy transfer among $S^{13}C^{15}N^-$ anions can be obtained by measuring the rate of anisotropy decay induced by energy transfer. However, it needs to note that the anisotropy decay can also be induced by the molecular reorientations, which should be removed from the overall anisotropy decay curves.

In experiments, the contributions from molecular reorientation and vibrational energy transfers can be clearly distinguished by changing the resonant energy transfer rate through adjusting the number of resonant energy acceptors. In measuring the resonant energy transfer rate among the $S^{13}C^{15}N$ anions in the 10M aqueous solutions, we used different amounts of SCN^- to replace $S^{13}C^{15}N^-$ in the solutions with the same overall salt concentration to adjust the number of resonant energy acceptors for the donor $S^{13}C^{15}N^-$. The resonance energy transfer time constant among $S^{13}C^{15}N^-$ can then be obtained from such energy-acceptor-number dependent energy-transfer-induced anisotropy decay measurements [90,106]. Figure 3.8 displays the anisotropy decay of the pump/probe signal of $S^{13}C^{15}N^-$ as a function of delay time in the 10 M aqueous solutions with pure $KS^{13}C^{15}N$ and mixtures of $KS^{13}C^{15}N$/KSCN with different isotope ratios [97]. The anisotropy decay of the $S^{13}C^{15}N^-$ signal obviously becomes faster with the increase of the $KS^{13}C^{15}N$ molar fraction, indicating the resonant energy transfers among the $S^{13}C^{15}N^-$ anions contribute significantly to the overall anisotropy decay of the $S^{13}C^{15}N^-$ signal, especially in the solutions with high $KS^{13}C^{15}N$ molar fractions. The resonant energy transfer time constant can be obtained straightforward. In the solution with 1% $KS^{13}C^{15}N$, the anisotropy decay of the $S^{13}C^{15}N^-$ signal is mostly caused by the molecular rotation because $S^{13}C^{15}N^-$ anions are too far away to effectively exchange energy. Therefore, the anisotropy decay time constant $\tau_{or} = 10 \pm 1$ ps of the solution with 1% $KS^{13}C^{15}N$ can be considered as the molecular rotational time constant of $S^{13}C^{15}N^-$ in all the 10M solutions, ignoring the very small influence caused by the mass differences among the C and N isotopes. In the solution with 100% $KS^{13}C^{15}N$, the anisotropy decay is from both molecular rotations and resonant energy transfers, with a time constant $t = 2.4$ ps. Thus the resonant energy transfer time constant τ can be obtained as 3 ps from the correlation $1/\tau = 1/t - 1/\tau_{or}$.

To more rigorously analyse the resonant energy transfer kinetics, an ion clustering based model is also needed. As a result, the concentration dependent anisotropy decay data shown in Figure 3.8 can be globally fitted by the following equation [90]:

$$\frac{R(t)}{R(0)} = \frac{1}{n_{tot} \times c \times e^{-\frac{t}{\tau_{or}}}} \left[n_{tot} \left(c \times e^{-\frac{t}{\tau}} + 1 - c \right)^{n_{tot}-1} c \times e^{-\frac{t}{\tau}} - \left(c \times e^{-\frac{t}{\tau}} + 1 - c \right)^{n_{tot}} + 1 \right]. \tag{3.13}$$

where τ_{or} is the rotational time constant of $S^{13}C^{15}N^-$, c is the percentage of $S^{13}C^{15}N^-$ (the energy carrier) among the isotopes, and n_{tot} is the number of anions (both $S^{13}C^{15}N^-$ and SCN^-) in an energy transfer unit (a big cluster can have more than one energy transfer units). τ is the resonant one-donor-to-one-acceptor energy transfer time constant.

In our experiment, $\tau_{or} = 10 \pm 1.0$ ps is experimentally determined from the anisotropy measurement of the 1% $KS^{13}C^{15}N$ 10M solution. c is the known experimental condition parameter. Calculations based on Equation (3.13) with two adjustable parameters (τ and n_{tot}) simultaneously fit the five experimental sets of experimental anisotropy decay data very well. The analysis on the results in Figure 3.8 yields $\tau = 54 \pm 8$ ps, and $n_{tot} = 18 \pm 3$. This gives the total resonant energy transfer time constant among the $S^{13}C^{15}N^-$ anions in the 100% $KS^{13}C^{15}N$ 10M solution to be 3 ps (54/18 ps).

3.3.3. *Comparison between experimental and predicted values*

The experimentally determined energy mismatch values and resonant and nonresonant (down-flowing) energy transfer time constants are listed in Table 3.1 [97]. The predicted energy transfer time constants based on Equation (3.6) with $\langle\beta\rangle = 13.6\,\text{cm}^{-1}$ and $\tau_c = 2.1$ ps are also listed. The value of $\langle\beta\rangle$ is experimentally determined, while $\tau_c = 2.1$ ps is a semi-empirical parameters, both of which have been discussed in the previous section.

For the two nonresonant cases, the predictions fit experimental results very well. However, the prediction (5.7 ps) for the resonant case is about 100% slower than what (3 ps) is experimentally observed. As discussed below, this deviation mainly arises from the different donor/acceptor ratio between the nonresonant and resonant energy transfer systems.

In the nonresonant energy transfer experiments, SCN^- and its isotope labeled $S^{13}C^{15}N^-$ (or $S^{13}CN^-$) are mixed with equal amounts, which means that half of the anions in an energy transfer unit are the nonresonant energy acceptors for one donor. However,

Table 3.1. Experimental and calculated energy mismatch dependence. The calculation is based on Equation (3.6) with $\tau_c = 2.1$ ps and $\langle\beta\rangle = 13.6\,\text{cm}^{-1}$.The nonresonant energy transfer time constants are for the down-flowing process. Reprinted with permission from [97]. Copyright 2011 American Chemical Society.

	$SCN^- \rightarrow S^{13}C^{15}N^-$	$SCN^- \rightarrow S^{13}CN^-$	$S^{13}C^{15}N^- \rightarrow S^{13}C^{15}N^-$
Energy mismatch (cm^{-1})	73.0	49.0	0.0
Experimental $1/k$ (ps)	115 ± 10	46 ± 7	3 ± 0.3 (unnormalised)
Calculated $1/k$ (ps)	108	54	6

in the resonant energy transfer experiment, all anions are the same species ($S^{13}C^{15}N^-$). For any energy transfer donor, all anions except this donor in the energy transfer unit are resonant energy acceptors. Therefore, the number of resonant energy acceptors for this donor is $n_{tot} - 1$, nearly two times of that in the nonresonant case $n_{tot}/2$. Since the coupling constant for both resonant and nonresonant calculations we used here is exclusively from the nonresonant energy transfer experiments, the prediction for the resonant energy transfer must therefore be about 100% slower than what is measured due to this acceptor number difference.

With the acceptor number normalised to the same number of energy acceptors in the calculation, based on the result of $n_{tot} = 18$, the experimental resonant energy time constant can be recalculated as 5.7 ± 0.6ps, which is now consistent with the prediction from Equation (3.6).

3.4. *The coupling strength dependence of energy transfer rates*

The analysis on the resonant energy transfer results gives us a hint, by changing the donor/acceptor population ratio, we should be able to change the overall vibrational coupling strength between one donor and its acceptors without changing the energy mismatch. Therefore, we further design a series of experiments to examine the correlation between the coupling strength and the energy transfer rate.

3.4.1. *The donor/acceptor number ratio dependence*

FTIR, 2D IR spectra and waiting time dependent CN/$^{13}C^{15}N$ vibrational energy exchange up-pumping and down-flowing cross peak intensities of 10M aqueous solutions with different KSCN/$KS^{13}C^{15}N$ ratios are shown in Figure 3.9 [97]. It can be clearly seen that the energy transfer rate changes obviously with the change of the donor/acceptor number ratio. In other words, the up-pumping/down-flowing ratio of nonresonant energy transfers with donor/acceptor number ratios other than 1/1 is not the Boltzmann factor, $\exp(-\hbar\omega_{ij}/kT)$. Instead, the rate ratio will be the product of the Boltzmann factor times the donor/acceptor number ratio:

$$\frac{k_{ji(up\text{-}pumping)}}{k_{ij\,(down\text{-}flowing)}} = e^{-\frac{\hbar\omega_{ij}}{RT}} \times \frac{n_i}{n_j} \tag{3.14}$$

It can be directly confirmed by the 2D IR experimental results. In the KSCN/$KS^{13}C^{15}N$ 77/23 sample, more energy acceptors are available for the up-pumping process than the down-flowing process. Therefore, based on Equation (3.14), the up-pumping rate must be 2.3 times of the down-flowing rate in this sample. As shown in Figure 3.9(A), energy up-pumping from $KS^{13}C^{15}N$ to KSCN is obviously faster than the down-flowing process. Quantitative analysis with the previously used location-energy-exchange model gives the result $k_{up\text{-}pumping}/k_{down\text{-}flowing} = 2.3$, same as predicted by Equation (3.14). Likewise, in the KSCN/$KS^{13}C^{15}N$ 25/75 sample (Figure 3.9(C)), the down-flowing rate is much faster than the up-pumping rate, with the rate ratio 4.3. Only in the KSCN/$KS^{13}C^{15}N$ 50/50 sample (Figure 3.9(B)), the rate ratio is determined by the Boltzmann factor $k_{up\text{-}pumping}/k_{down\text{-}flowing} = 0.7$. All the experimental energy transfer time constants are listed in Table 3.2.

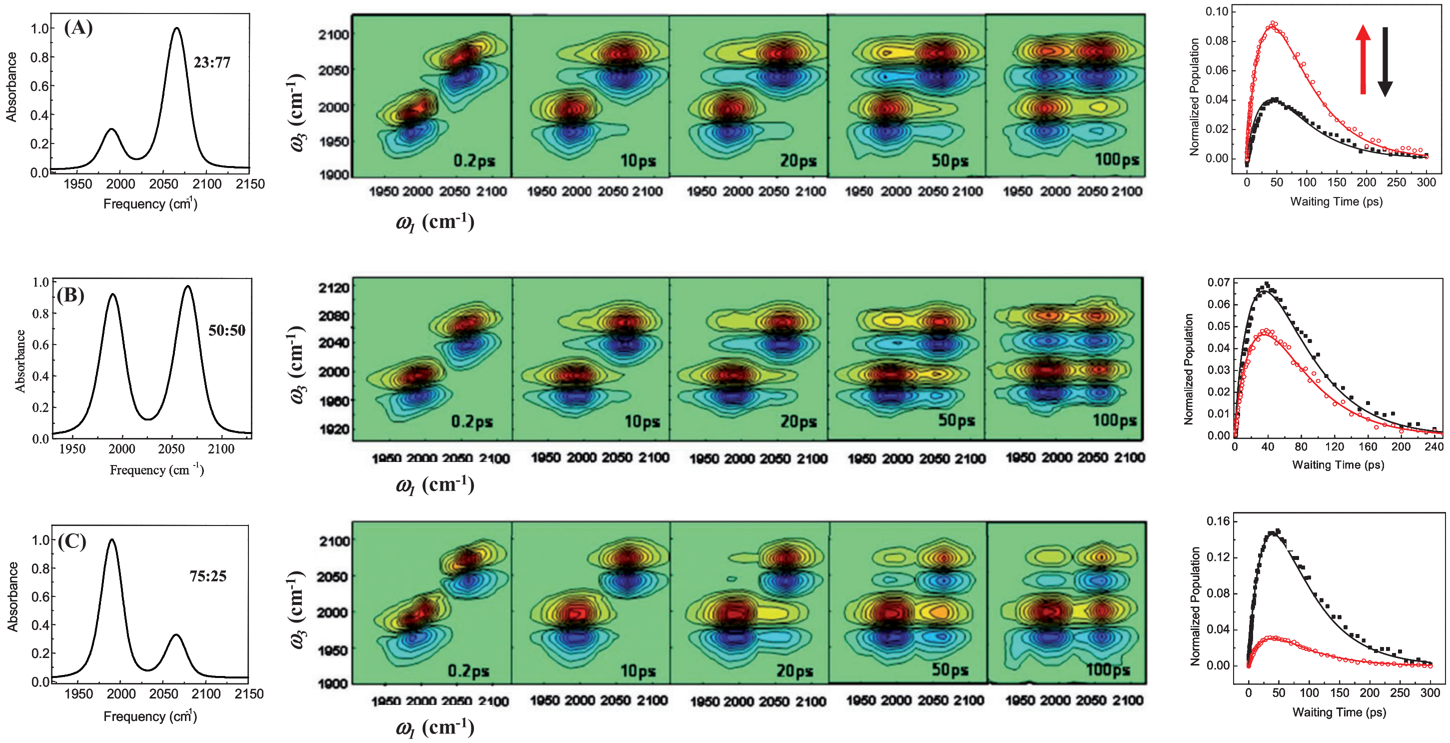

Figure 3.9. (Colour online) FTIR, 2D IR spectra and waiting time dependent up-pumping and down-flowing cross peak intensities (points are data and curves are calculations based on the kinetic model) of 10M aqueous solutions with different KSCN/KS^{13}C^{15}N ratios. (A) KSCN/KS^{13}C^{15}N = 77/23; (B) KSCN/KS^{13}C^{15}N = 50/50; (C) KSCN/KS^{13}C^{15}N = 25/75. At shortest waiting time, the intensities of two diagonal peak pairs in 2D IR spectra are normalised to be equal. Reprinted with permission from [97]. Copyright 2011 American Chemical Society.

3.4.2. *The coupling strength dependence*

The nonresonant energy transfer experiments with different donor/acceptor number ratios provide an opportunity for us to examine the coupling strength dependent energy transfer rates without changing the donor/acceptor energy mismatch. In a sample where the donor/acceptor ratio is not 1/1, the effective coupling strength for the down-flowing process is different from that for the up-pumping process because the energy acceptor numbers for these two processes are different. Provided that the acceptors are identical, the total coupling strength $\langle\beta_{1\to n}\rangle$ from one donor to n acceptors is $\sqrt{n}$ times $\langle\beta_{1\to 1}\rangle$ from one donor to one acceptor [97]:

$$\langle\beta_{1\to n}\rangle = \sqrt{n}\langle\beta_{1\to 1}\rangle. \tag{3.15}$$

The correlation between the donor/acceptor number ratios and the coupling strength is consistent with experimental data. For example, in the KSCN/KS^{13}C^{15}N 77/23 sample, the coupling strength $\langle\beta_{up\text{-}pumping}\rangle$ of the up-pumping from S^{13}C^{15}N$^-$ to SCN$^-$ is for one donor to 77%n_{tot} acceptors, and the down-flowing coupling strength $\langle\beta_{down\text{-}flowing}\rangle$ is for one donor to 23%n_{tot} acceptors. According to Equation (3.15), $\langle\beta_{up\text{-}pumping}\rangle/\langle\beta_{down\text{-}flowing}\rangle = \sqrt{77/23} = 1.8$, which is consistent with the experimental results $\langle\beta_{up\text{-}pumping}\rangle/\langle\beta_{down\text{-}flowing}\rangle = 1.7$. Based on this coupling ratio and Equation (3.6), $k_{up\text{-}pumping}/k_{down\text{-}flowing} = e^{-73/205} \times 1.8^2 = 2.3$, which again agree well with the experimental results $k_{up\text{-}pumping}/k_{down\text{-}flowing} = (1/94)/(1/210) = 2.3$. For other samples with different donor/acceptor population ratios, similar results are obtained. Experimental and predicted coupling strength and energy transfer time constants are listed in Table 3.2 [97]. And the experimental coupling strength and energy mismatch dependences and calculations based on Equation (3.6) are plotted in Figure 3.10.

As shown in Figure 3.10 [97], calculations based on Equation (3.6) are consistent with experimental results. However, the uncertainty of the experimentally measured individual coupling strength is relatively big, resulting in a very big uncertainty in the calculated energy transfer rate constants. The big experimental uncertainty mainly comes from two factors: (1) the anharmonicities of vibrational coupling peaks are only a few wavenumbers, while the resolution of the spectrometer is $1 \sim 2\,\text{cm}^{-1}$; (2) the bandwidth of the coupling

Table 3.2. Calculated and experimental energy transfer (down-flowing and up pumping) time constants and coupling strengths for the mixed KS^{13}C^{15}N/KSCN aqueous solution with different isotope ratios. Reprinted with permission from [97]. Copyright 2011 American Chemical Society.

KS13C15N:KSCN	23:77	34:66	50:50	67:33	75:25
Experimental $\langle\beta\rangle_{down}$ (cm^{-1})	9.8 ± 4.0	11.9 ± 4.0	13.6 ± 3.0	16.2 ± 4.0	18.4 ± 5.0
Experimental $\langle\beta\rangle_{up}$ (cm^{-1})	17.3 ± 4.0	14.9 ± 3.0	13.6 ± 3.0	11.9 ± 4.0	9.8 ± 4.0
Experimental $1/k_{down}$(ps)	210 ± 30	143 ± 15	115 ± 10	68 ± 10	56 ± 8
Experimental $1/k_{up}$(ps)	94 ± 10	113 ± 15	164 ± 15	219 ± 20	267 ± 30
Calculated $\langle\beta\rangle_{down}$ (cm^{-1})	9.7 ± 0.7	11.8 ± 0.6	13.1 ± 0.6	17.1 ± 1.4	18.8 ± 1.4
Calculated $\langle\beta\rangle_{up}$ (cm^{-1})	17.4 ± 0.8	15.9 ± 0.9	13.2 ± 0.5	11.4 ± 0.5	10.4 ± 0.5
Calculated $1/k_{down}$ (ps)	208 ± 80	141 ± 80	108 ± 50	76 ± 40	59 ± 30
Calculated $1/k_{up}$ (ps)	95 ± 60	128 ± 70	154 ± 50	201 ± 90	296 ± 140

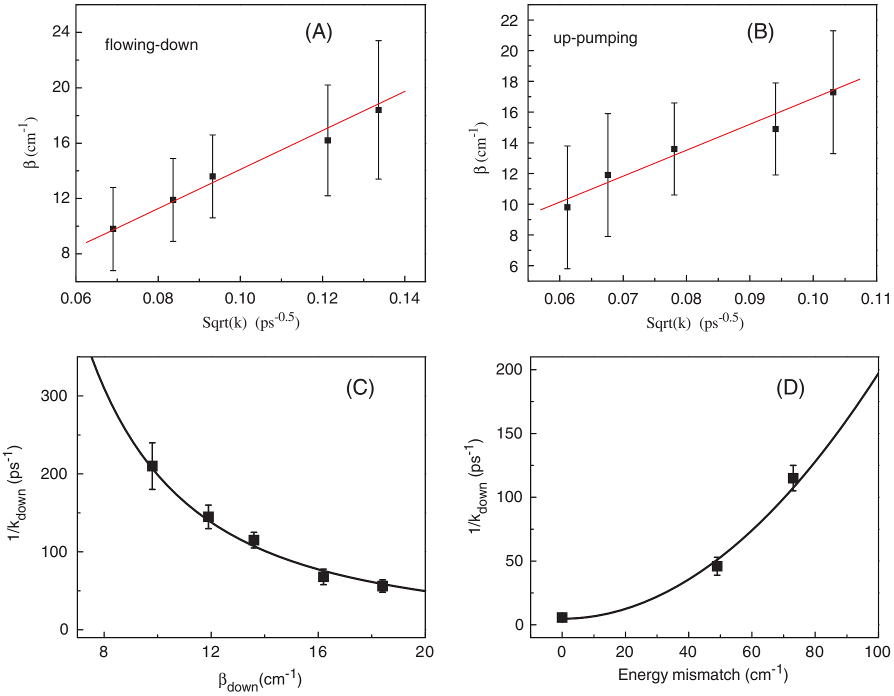

Figure 3.10. (A) Correlation between $\langle\beta\rangle$ and $\sqrt{k_{flowing-down}}$; (B) Correlation between $\langle\beta\rangle$ and $\sqrt{k_{up\text{-}pumping}}$; (C) The coupling strength dependence of the down-flowing energy transfer time constants of the $KS^{13}C^{15}N$/KSCN 10 M solutions with a constant energy mismatch 73 cm^{-1}. (D) The energy mismatch dependence of the down-flowing energy transfer time constants with a constant average coupling strength 13.6 cm^{-1}. Dots are data, and lines are calculations using Equation (3.6) with $\tau_c = 2.1$ ps. Reprinted with permission from [97]. Copyright 2011 American Chemical Society.

red and blue peaks is ~30 cm^{-1}, while their frequency difference is only a few wavenumbers, resulting in a severe spectral overlap. Experimentally, the energy transfer rates can be much more precisely determined. Therefore, in principle, Equation (3.6) provides a better way for obtaining vibrational coupling strength with known energy transfer rates than the direct measurement with 2D IR methods. In this series of experiments, the determination of individual coupling strength through the 2D IR method has a relatively big uncertainty. However, the relative difference among the coupling strengths of samples with different donor/acceptor population ratios has a very small uncertainty. Therefore, the big uncertainty of the individual determination can possibly significantly affect the slopes of the straight lines in Figure 3.10(A) and (B). Its effect on the linearity of the lines is relatively slight.

In conclusion, coupling strength and energy mismatch dependent experiments show that the intermolecular vibrational energy transfer rate can be quantitatively described with an analytical Equation (3.6) derived from the Fermi golden rule. This equation mathematically connects energy transfer kinetics with the average vibrational coupling strength and other structural parameters, and therefore provides an important way to determine the coupling strength between two coupled oscillators through measuring the vibrational energy transfer kinetics. Coupled with the dipole/dipole interaction Equation (2.57) and (3.6) connects vibrational energy transfer kinetics with the energy donor/acceptor distance, forming the basis for determining molecular distances through measuring vibrational energy transfers. However, there are still many questions needs to be resolved before this ultimate goal can be achieved. For example, some other interactions rather than the dipole-dipole interaction, e.g. mechanical couplings or high order interactions can also play roles on the intermolecular vibrational energy transfer. These interactions have different expressions for the coupling strength. How one interaction can be experimentally distinguished from another is still an open question.

In principle, the mode-specific vibrational energy exchange method can be used to study many transient (<1ns) short range (<1 nm) molecular interactions. It may or may not need isotope labeling, which in general does not perturb the molecular interactions. In chapter 4, some applications of vibrational energy transfers in determining molecular distances are introduced.

4. Ion clustering in aqueous solution

We have shown that intermolecular vibrational energy transfer kinetics can be quantitatively correlated to intermolecular distances. In this chapter, we will introduce the applications of vibrational energy transfers in studies of ion clustering, ion/ion interactions, and ion/molecule interactions in liquids.

4.1. *Ion clustering in aqueous solutions probed with vibrational energy transfer*

A majority of chemical and biological processes of the natural world proceed in electrolyte aqueous solutions. The properties of ions in water are relevant to a wide range of systems, including electrochemistry, biological environments and atmospheric aerosols. Tremendous scientific efforts have been devoted to unravel the hydration structures of ions in water [52,66,115,154–161] for more than 100 years. For very dilute solutions, the structures and dynamics of the aqueous electrolyte solutions can be well described by the Debye-Huckel theory [157,162]. However, this theory begins to fail when solutions go to higher concentrations at which many practical situations are, e.g. batteries, fuel cells, salt crystallisations, and the formations of natural mineral compounds.

The formation of ion pairs containing two ions of opposite charge has been proposed to be primarily responsible for this failure [155,156]. Calculations from molecular dynamics (MD) simulations suggested that, clusters with more than one ions of the same charge which are traditionally viewed as unlikely, could be a major factor contributing to the non-ideality of solutions at medium or high concentrations [163,164]. If the MD simulation results are general, in concentrated $KSCN/KS^{13}C^{15}N$ mixed aqueous solutions the probability of forming contact clusters of the general formula $K_n(SCN)_m(S^{13}C^{15}N)_p$ would be statistically very high [165,166]. The thiocyanate anions can be considered as "ligands" to the cation K^+ in these clusters. Therefore, the anions that held in close proximity can exchange vibrational energy through their overlapped orbitals or via dipole-dipole interactions as that observed for metal carbonyl compounds [48], which was already shown in Section 3.3.

By monitoring intermolecular mode-specific resonant and nonresonant vibrational energy transfers [70,96,106,107] among the thiocyanate anions, we were able to directly probe ion clustering in a series of 1:1 strong electrolyte (LiSCN, NaSCN, KSCN and CsSCN) aqueous solutions. These results shows, in an apparent "homogeneous" SCN^- aqueous solution, both clustered and water-solvated anions simultaneously exist, as illustrated in Figure 4.1 (A) [90].

4.1.1. *Vibrational energy exchange in a cluster*

The FTIR spectrum of a 1/1 $KSCN/KS^{13}C^{15}N$ mixed aqueous (D_2O) solution with a salt/water molar ratio 1/2.4 (10 M) is shown in Figure 4.1(B). The isotope labeling shifts

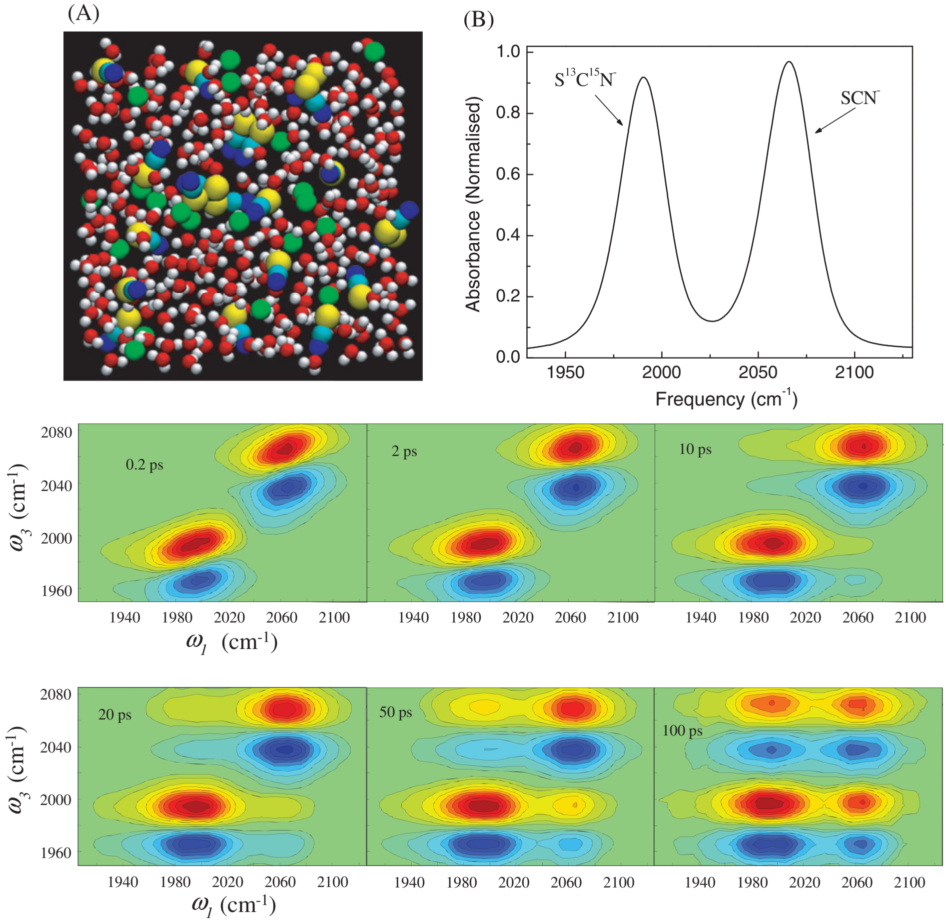

Figure 4.1. (Colour online) (A) A snapshot of a 1.8M KSCN aqueous solution from a molecular dynamics simulation. O (red), H (white), C (light blue), N (deep blue), K (green) and S (yellow). An ion cluster is visible at the center of the picture. Some water molecules are removed from the original file to better display the cluster structure. (B) FTIR absorption spectra and (C) time dependence of the 2D IR spectra of the 10M 1:1 $KSCN/KS^{13}C^{15}N$ aqueous solution [90].

the CN stretch frequency from 2064 cm^{-1} (SCN$^-$) down to 1991 cm^{-1} (S^{13}C^{15}N$^-$). The frequency difference allows the vibrational energy transfers between SCN$^-$ and S^{13}C^{15}N$^-$ to be directly observed by the energy exchange method introduced in chapter 3.

The time dependent 2D IR spectra of the mixed solution are shown in Figure 4.1(C), which we have already discussed in Section 3.3. In short, the growths of the two cross peak pairs (Peaks 5 ~ 8) in the 50-ps panel indicate that the vibrational energy has exchanged between the CN and ^{13}C^{15}N stretches of SCN$^-$ and S^{13}C^{15}N$^-$. As discussed before, in contrast to the chemical exchange 2D IR methods [3,14,34,59,142], the cross peak intensities in the energy exchange method are not equal. According to Equation (3.14), the ratio of their growth rates in the 1:1 mixture is determined by the detailed balance principle. The energy mismatch between the CN and ^{13}C^{15}N stretches is $2064 - 1991 = 73\,\text{cm}^{-1}$, resulting in that the energy up-pumping rate constant from S^{13}C^{15}N$^-$ to SCN$^-$ is ~70% of the down-flowing rate constant from SCN$^-$ to S^{13}C^{15}N$^-$. As a result, Peaks 5 and 6 are always bigger than Peaks 7 and 8 at the same time delay. At 100ps, the diagonal and cross peaks have about the same intensity, indicating the energy exchange times should be at the order of 100 ps.

The observation of vibrational energy exchange between S^{13}C^{15}N$^-$ and SCN$^-$ in the aqueous solution is very surprising and unexpected. As introduced in chapter 3, in the $C_6H_5SeCN/CDCl_4$ system, the energy transfer between the donor and the acceptor is very slow, only ~330 ps. In the KSCN/KS^{13}C^{15}N mixed aqueous solution, intuitively, the two anions were expected to repel each other because of the same charge they have and be surrounded by water molecules. They should not be able to transfer energy three times faster than the $C_6H_5SeCN/CDCl_4$ system where a strong H-bond is formed between the energy donor and acceptor with a similar energy mismatch, 97 cm^{-1}, unless there are some special interactions among the anions keeping them close to each other. According to the dipole/dipole interaction Equation (2.57) and the vibrational energy transfer Equation (3.6), the energy transfer rate is dependent on many factors, e.g. the energy mismatch, environment, the transition dipole moments of the donor and acceptor, the donor/acceptor distance, the local refractive index, and the donor/acceptor transition dipole moment cross angle. Among these factors, the donor/acceptor is the most sensitive one, because the energy transfer rate constant is inversely proportional to the sixth power of the distance for the dipole/dipole interaction. The background led us to rethink about the structures in the aqueous solutions, and we predicted that it was quite conceivable that two anions can be held close to each other by a same cation. Such an ion clustering effect should be the primary reason for the observed relatively fast SCN$^-$ to S^{13}C^{15}N$^-$ energy transfers. This conclusion was further confirm by measuring the 2DIR spectra of 1:1 C_2H_5SCN and $C_2H_5S^{13}C^{15}N$ mixed liquid, which has similar average molecular distance and energy mismatch to those of the 10 M KSCN/KS^{13}C^{15}N mixed solution, but no energy exchange cross peaks was observed in the 2DIR spectra [90]. Many control experiments, e.g. concentration dependent experiments, mixed salts experiments, measurements on mixed isotope labeled potassium thiocyanate crystals, and measurements on samples in different solvents, some of which will be introduced in the following, were conducted to examine the ion clustering hypothesis. From these experiments, we finally concluded that most of the anions in the saturated KSCN/KS^{13}C^{15}N mixed aqueous solution have direct contact with each other.

4.1.2. *Location-energy-exchange kinetic model*

As discussed above, a microscopic picture in the high concentrated KSCN/KS^{13}C^{15}N mixed solution can be depicted: some anions are clustered and can transfer energy efficiently, and other anions are well separated from each other and less able to exchange energy with other anions. These two types of anions are not frequency resolvable. Since the anions that are clustered can exchange energy more efficiently than those are well separated from each other, the off-diagonal peaks in the 2DIR spectra are mainly from the clustered anions. The diagonal peaks are contributed from both separated and clustered anions. Therefore, not only the energy exchange rates but also the ratio of these two anions can be derived by analyzing the time evolutions of both diagonal and off-diagonal peaks simultaneously.

A location-energy-exchange kinetic model was created based on the ion clustering picture to analyze the data. In the aqueous solution, some S^{13}C^{15}N$^-$ and SCN$^-$ form clusters (denoted as $S^{13}C^{15}N^-_{clu}$ and SCN^-_{clu}), and the rest of the anions are separated from each other (denoted as $S^{13}C^{15}N^-_{iso}$ and SCN^-_{iso}). These two types of anions are in dynamic equilibrium: they can exchange locations with rate constants $k_{clu\rightarrow iso}$ and $k_{iso\rightarrow clu}$, the ratio of which is determined by the detailed balance principle: $D = k_{S^{13}C^{15}N^-\rightarrow SCN^-}/k_{SCN^-\rightarrow S^{13}C^{15}N^-} = 0.7$ at the experimental temperature $T = 295K$. The clustered $S^{13}C^{15}N^-_{clu}$ and SCN^-_{clu} anions can exchange vibrational energy with rate constants $k_{S^{13}C^{15}N^-}\ {}_{\rightarrow SCN^-}$ and $k_{SCN^-}\ {}_{\rightarrow S^{13}C^{15}N^-}$. The isolated anions cannot transfer vibrational energy with other isolated anions or with the clustered anions, as the energy transfer rate between the isolated anions must be much smaller than the energy transfer rate inside the clusters. The vibrational excitations of S^{13}C^{15}N$^-$ and SCN$^-$ decay with their own vibrational relaxation rate constants $k_{S^{13}C^{15}N^-}$ and k_{SCN^-}. In experiments, we can manage to obtain rotation-free data to eliminate any rotational component. The model is described in the following scheme,

According to Scheme 4.1, four differential equations can be derived to describe the energy transfer behavior among four sorts of anions:

$$\begin{aligned}\frac{\mathrm{d}\left[S^{13}C^{15}N^- *_{clu}(t)\right]}{\mathrm{d}t} &= -(k_{S^{13}C^{15}N^-} + k_{clu\rightarrow iso} + k_{S^{13}C^{15}N^-\ \rightarrow SCN^-})\left[S^{13}C^{15}N^- *_{clu}(t)\right]\\ &\quad + k_{iso\rightarrow clu}\left[S^{13}C^{15}N^- *_{iso}(t)\right] + k_{SCN^-\ \rightarrow S^{13}C^{15}N^-}\left[SCN^- *_{clu}(t)\right]\end{aligned} \tag{4.1}$$

$$\begin{aligned}\frac{\mathrm{d}\left[S^{13}C^{15}N^- *_{iso}(t)\right]}{\mathrm{d}t} &= -(k_{S^{13}C^{15}N^-} + k_{iso\rightarrow clu})\left[S^{13}C^{15}N^- *_{iso}(t)\right]\\ &\quad + k_{clu\rightarrow iso}\left[S^{13}C^{15}N^- *_{clu}(t)\right]\end{aligned} \tag{4.2}$$

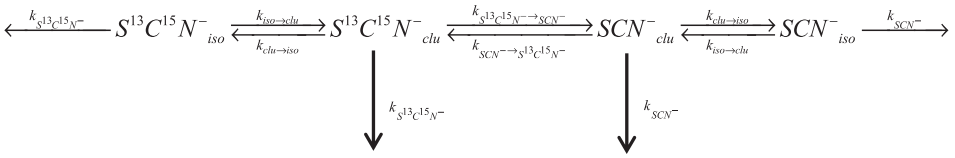

Scheme 4.1. Location-energy-exchange kinetic model.

$$\begin{aligned}\frac{\mathrm{d}[SCN^- *_{clu}(t)]}{\mathrm{d}t} &= -(k_{SCN^-} + k_{clu\to iso} + k_{SCN^-\to}S^{13}C^{15}N^-)[SCN^- *_{clu}(t)] \\ &\quad + k_{iso\to clu}[SCN^- *_{iso}(t)] + k_{S^{13}C^{15}N^- \to SCN^-}\left[S^{13}C^{15}N^- *_{clu}(t)\right] \qquad (4.3)\end{aligned}$$

$$\frac{\mathrm{d}[SCN^- *_{iso}(t)]}{\mathrm{d}t} = -(k_{SCN^-} + k_{iso\to clu})[SCN^- *_{iso}(t)] + k_{clu\to iso}[SCN^- *_{clu}(t)], \qquad (4.4)$$

where * represents vibrational excitation. The equations are numerically solved with initial conditions $[S^{13}C^{15}N^- *_{clu}(0)] = K/(K+1)$, $[S^{13}C^{15}N^- *_{iso}(0)] = 1/(K+1)$, $[SCN^- *_{clu}(0)] = [SCN^- *_{iso}(0)] = 0$ if $S^{13}C^{15}N^-$ is initially excited. $[S^{13}C^{15}N^- *_{clu}(t)] + [S^{13}C^{15}N^- *_{iso}(t)]$ (Peak 3) and $[SCN^- *_{clu}(t)] + [SCN^- *_{iso}(t)]$ (Peak 7) are experimentally determined. Similar expressions are applied if SCN^- is initially excited. Comparing the calculations using Equations (4.1) ~ (4.4) with experimental results, we obtain the energy transfer rate constants, the equilibrium constant and the location exchange rate constants.

The vibrational decays of the nitrile stretches are experimentally observed to be bi-exponential. Vibrational bi-exponential decays are frequently observed for modes in the range of 2000 ~ 2300 cm^{-1} [33,70,81,96]. It has been attributed to the fast vibrational equilibrium between a bright mode and some coupled dark modes [33]. Here, we adopt the method we developed for bi-exponential decays to analyse the kinetics [33,70,96], which we have introduced when deriving the energy transfer rate in the system of $C_6H_5SeCN/DCCl_3$ mixture.

The vibrational decay rate constants are experimentally determined. In calculations, they are allowed to vary by 10%. The exchange rate constants and the equilibrium constant are not known beforehand. Because the ratio of the location exchange rate constants is the equilibrium constant and the ratio of the energy transfer rate constants is determined by the detailed balance principle, there are only three unknown parameters in the calculations. With these constraints, calculations give $1/k_{SCN^- \to S^{13}C^{15}N^-} = 115 \pm 15$ ps, the equilibrium constant K is 19 ± 3, which corresponds to $95 \pm 1\%$ of anions in clusters, and the clustered and isolated anions exchange time constant $1/k_{clu\to iso} = 12 \pm 7$ ps. In this model, we assumed that the clustered and separated anions have the same vibrational lifetimes, which is different from the experimental fact. By using different vibrational lifetimes experimentally determined for the two species, calculations give the same energy transfer time constant, but a slight different ion cluster ratio which is $97 \pm 1\%$ [90]. Calculations with the three parameters simultaneously fit the four experimental curves very well, shown in Figure 4.2 [90].

4.1.3. *Properties of ion clusters*

We have used polarisation selective 2D IR method to study the resonant energy transfer in Section 3.3. An equation to analyze the concentration dependent anisotropy decay data was employed to reveal the resonant energy transfer time constant:

$$\frac{R(t)}{R(0)} = \frac{1}{n_{tot} \times c \times e^{-\frac{t}{\tau_{or}}}}\left[n_{tot}\left(c \times e^{-\frac{\tau}{t}} + 1 - c\right)^{n_{tot}-1} c \times e^{-\frac{t}{\tau}} - \left(c \times e^{-\frac{t}{\tau}} + 1 - c\right)^{n_{tot}} + 1\right]. \qquad (3.13)$$

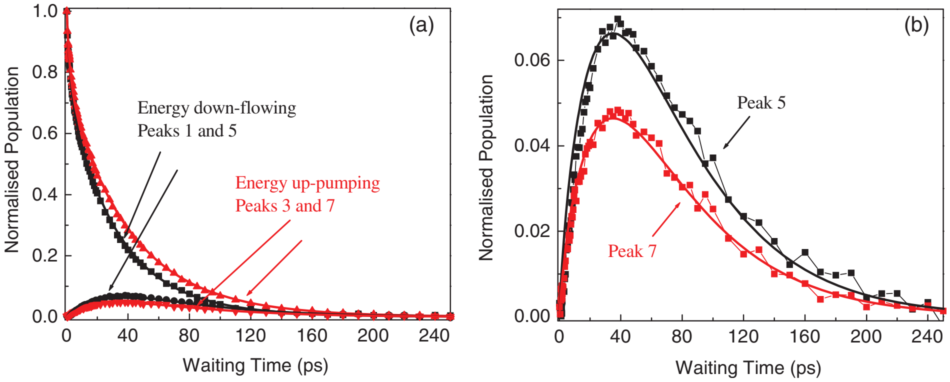

Figure 4.2. (Colour online) Peak intensity data (dots) and fits to the data (lines) of the time dependent 2D IR spectra shown in figure 4.1 [90].

The derivation of Equation (3.13) was based on the fact that the anisotropy is directly proportional to the time dependent number of excited donor molecules (see Section 2.4.2.2). Therefore, the concentration dependent anisotropy decay can be derived by solving the rate equation of the molecules within an average sized cluster. The details was provided in the supporting materials of our previous article [90]. There is also a revised version to improve this model, which can count the signal from each individual cluster to analyze the anisotropy data [97]. The results from these two models differ for only a few percent.

This equation can also be used to estimate the average cluster size in the concentrated KSCN aqueous solution. In Equation (3.13), only two parameters (n_{tot} is the number of anions in an energy transfer unit inside a cluster. It approaches to number of anions within a cluster in smaller clusters. τ is the resonant one-donor-to-one-acceptor energy transfer time constant) are experimentally unknown. Calculations with the two adjustable parameters simultaneously fit the experimental results of six different isotope ratios very well (Figure 4.3 [90]). The calculations show that $\tau = 54 \pm 8$ ps and $n_{tot} = 18 \pm 3$. Note, as we have tried, the standard Forster approach without assuming ion clustering [106] couldn't describe the experimental data well.

The concentration dependence property of the ion clusters was also studied. According to the thermodynamic principle [167], diluting the KSCN concentrated solution with water shifts the dissolution equilibrium to fewer clusters. This can be revealed by simple inspection of the growth of cross peaks in 2D IR spectra of solutions with different salt concentrations in Figure 4.4 [90]. At higher concentrations, the intensities of cross peaks are higher at the same T_ws. As described above, the growth of cross peaks is from the energy exchange of clustered anions, while the diagonal peak pairs are from both clustered and separated anions. The cross/diagonal peak ratio represents not only how fast the energy exchange is, but also how many of the anions form clusters. A higher cross/diagonal peak ratio indicates a faster energy transfer and/or more clusters.

Quantitative analyses based on the above model indicate fewer and smaller clusters formed in a lower concentration, as shown in Table 4.1 [90]. The fraction of anions in clusters is unexpectedly large in all studied concentrations. In highly concentrated

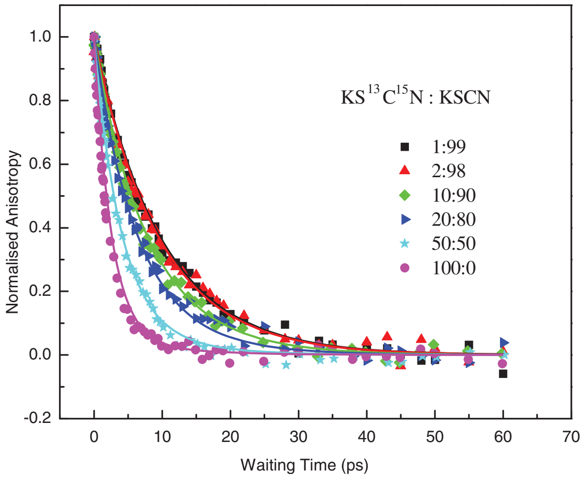

Figure 4.3. (Colour online) The anisotropy decay data (dots) and calculations of Equation (lines) of the ^{13}C^{15}N stretch of S^{13}C^{15}N^{-} in 10M salt aqueous solutions with different KS^{13}C^{15}N/KSCN ratios [90].

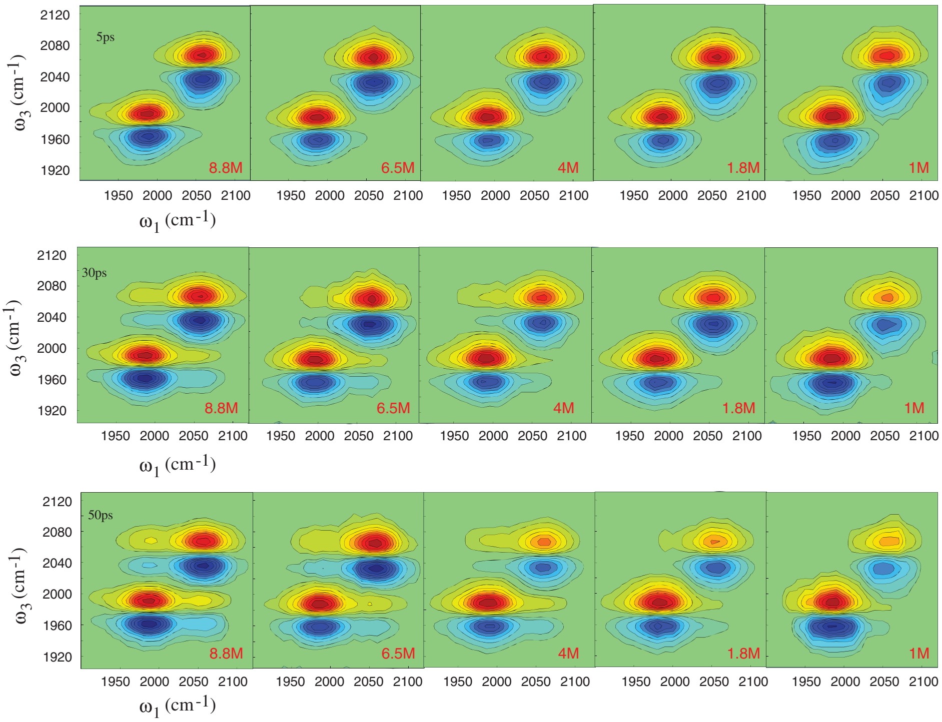

Figure 4.4. (Colour online) The concentration dependences of the 2D IR spectrum of 1:1 KSCN/KS^{13}C^{15}N aqueous solutions at different T_{ws} [90].

Table 4.1. Experimental cluster concentrations, the number of anions (n_{tot}) in an energy transfer unit, and the resonance one-donor-to-one-acceptor energy transfer time constant (τ) in varies of the solutions. [90].

	Percentage of clustered ions	n_{tot}	τ(ps)
KSCN (10 M)	$97 \pm 2\%$	18 ± 3	54 ± 8
KSCN (8.8 M)	$92 \pm 1\%$	13 ± 2	40 ± 8
KSCN (6.5 M)	$70 \pm 4\%$	9 ± 2	32 ± 6
KSCN (4 M)	$67 \pm 4\%$	5 ± 2	25 ± 6
KSCN (1.8 M)	$35 \pm 5\%$	4 ± 1	18 ± 5
KSCN (1 M)	$27 \pm 6\%$	3 ± 1	15 ± 4
LiSCN (4 M)	$50 \pm 4\%$	4 ± 1	10 ± 4
NaSCN (4 M)	$60 \pm 4\%$	5 ± 1	18 ± 5
CsSCN (4 M)	$70 \pm 4\%$	9 ± 2	45 ± 8

solutions (10 and 8.8M) almost all anions are in clusters ($>90\%$). Even for a relatively dilute solution (1M) whose salt/water ratio is only $\sim 1/50$, there still $\sim 27\%$ of anions are in clusters which contain three anions on average. MD simulations also gave very similar results on the ion cluster concentrations.

Moreover, the cation dependence of ion clustering was also studied. It has long been recognised that the size and charge density of a cation have profound effects on the properties of electrolyte solutions and their biological activities [155]. Theoretical calculations suggest that cations may affect the formation of ion pairs and clusters in aqueous solutions [164,168]. To explore cation specific effects, we performed energy transfer measurements on 4M (salt/water ratio = 1/10) aqueous solutions of LiSCN, NaSCN, KSCN and CsSCN. These experiments show that in solution, smaller cations form smaller and fewer clusters (see Table 4.1). In solution with the smallest cation Li^+ (LiSCN), $\sim 50\%$ of the anions form clusters which contain ~ 4 anions on average. In solution with the biggest cation Cs^+ (CsSCN), $\sim 70\%$ of the anions form clusters containing ~ 9 anions. This trend may be qualitatively understood with the theoretical description of "matching cation and anion sizes" for some electrolyte solutions [168,169]: small-small and large-large easily associate, while small-large readily dissociate. SCN^- is large and polarisable, and therefore, more readily associates with the large and polarisable Cs^+ than the small Li^+.

4.1.4. *Comparisons among aqueous solutions and crystals*

In the 10M potassium thiocyanate solution, the above result show that the ion clusters contain at least 18 anions. However, the rotational relaxation time of the anion in the cluster is only ~ 10 ps, three times slower than that of the free anion in the dilute solution. The rotation of the clustered ions is too fast if the Einstein–Stokes equation holds for the situation. Anisotropy measurements on the potassium crystal provide a plausible explanation for this observation: the anions in the crystal rotate with a time constant ~ 11ps, as fast as those in the saturated solution, as displayed in Figure 4.5.

We have presented that, the number of anions in an energy transfer unit in the saturated solution is the same as the number of the first shell SCN^- anions surrounding

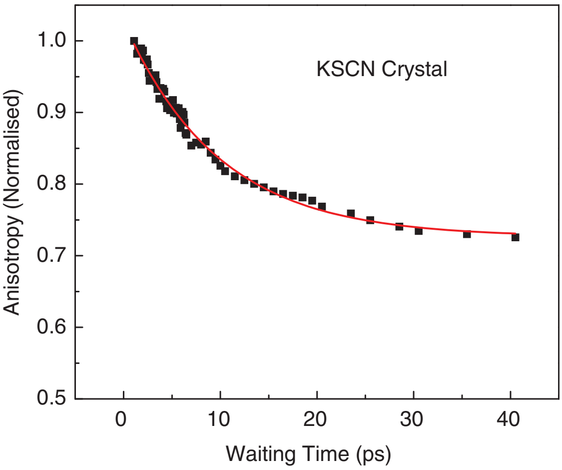

Figure 4.5. (Colour online) Rotational anisotropy decay of $S^{13}C^{15}N^-$ in a $KSCN/KS^{13}C^{15}N$=98/2 (wt) mixed crystal. The rotational time constant was determined to be 11 ± 1 ps. The rotation is hindered in the crystal. The rotational angle is calculated to be about 30^0 from the residual anisotropy.

one anion in the KSCN crystals [90]. In addition, according to Equation (3.6) and Equation (2.57), the anion distance in a cluster in the saturated solution was determined to be 0.4 nm, identical to the shortest anion distance in the KSCN crystal determined by XRD [90]. In the $KSCN/KS^{13}C^{15}N$ 1/1 mixed crystal at room temperature, the time constant of nonresonant energy transfer from SCN^- to $S^{13}C^{15}N^-$ is determined to be 111 ± 8 ps. Within experimental uncertainty this result is identical to that in the saturated solution. 2D IR spectra of the crystalline sample are displayed in Figure 4.6. The series of comparison experiments on the crystalline samples reveal many similarities between the anions in ion clusters in the KSCN saturated aqueous solution and the KSCN crystal. More experiments on the energy transfer kinetics and structural changes in the KSCN aqueous solutions, crystals and melt are still undergoing in our lab.

4.2. *Ion association in aqueous solutions*

We have demonstrated that substantial amounts of ions form ion clusters in the KSCN aqueous solutions of 2M ~10M. From the measured energy transfer kinetics, both the cluster size and the cluster concentration were derived. However, in these experiments, we did not have an internal calibration for the distance between two anions. In other words, we did not use the same method to directly compare the relative distances among the anion, cation, and water molecules in the same solutions to remove the systematic error of the method itself, mainly because the cation K^+ cannot provide any detectible vibrational signal in our experiments.

In this section, we will introduce further work to resolve this issue. We use NH_4^+ to replace K^+ and therefore we are able to measure energy transfers between the cation NH_4^+ and the anion SCN^- through the NH bending mode and the CN stretching mode, between the anion SCN^- and the water H_2O through the CN stretching mode and the OH bending

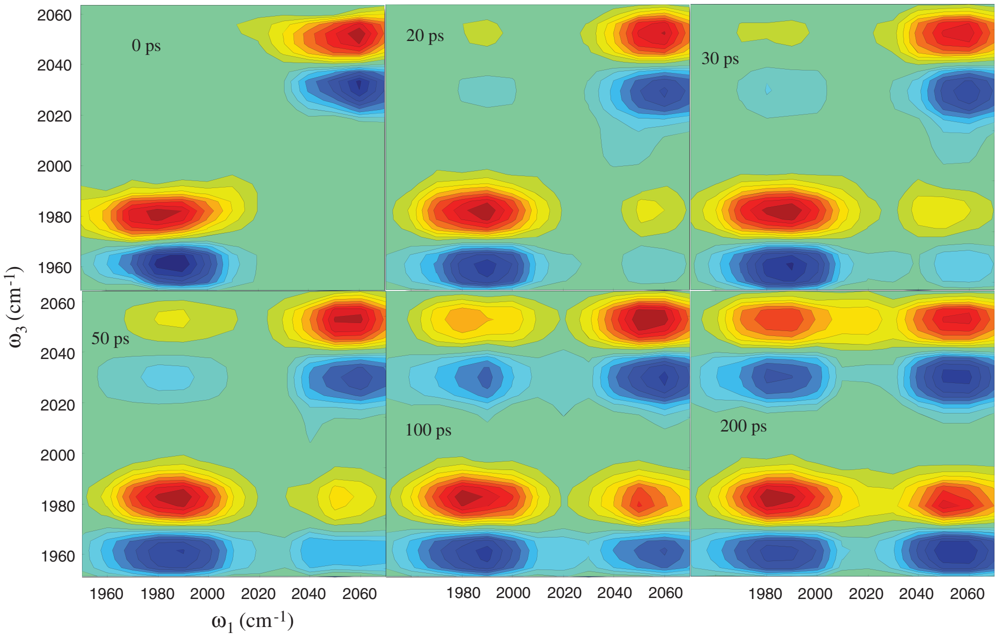

Figure 4.6. (Colour online) Time dependent 2D IR spectra of the KSCN/KS^{13}C^{15}N 1/1 mixed crystal at room temperature.

mode, and between the cation NH_4^+ and the water H_2O through the NH bending mode and the OH bending mode. By comparing the energy transfers among these species in a KSCN/H_2O (1/10 molar ratio) solution and a NH_4SCN/H_2O (1/10 molar ratio), we obtained clear evidence that ~60% of the SCN^- anions in the NH_4SCN/H_2O (1/10 molar ratio) solution have direct contacts with the NH_4^+ cations.

4.2.1. *Vibrational energy dynamics of the KSCN/H2O (1/10) solution*

Figure 4.7 displays the FTIR spectra of a KSCN/H_2O (1/10 molar ratio) solution, a KSCN/D_2O (1/10 molar ratio) solution and pure H_2O [170]. The peak at 2066 cm^{-1} is assigned to the CN stretching mode of SCN^-. The peak at 1636 cm^{-1} is assigned to the OH bending mode of H_2O. In the D_2O solution, the bending mode shifts to a lower frequency 1203 cm^{-1} because of the heavier mass of deuterium. The vibrational frequency differences between D_2O and H_2O have a dramatic effect on the vibrational dynamics of the CN stretch of SCN^- dissolved in them, e.g. our experiment results showed the lifetime of its 1st vibrational excited state drops from 23 ± 2 ps in the D_2O solution to only 2.8 ± 0.2 ps in the H_2O solution. The faster relaxation of the excited CN stretch in the H_2O solution indicates an efficient energy transfer from the CN stretch to the vibrational mode(s) of H_2O, which will be confirmed by the following 2D IR results.

Figure 4.8 displays the waiting time dependent 2D IR spectra of the KSCN/H_2O (1/10 molar ratio) solution [170]. The appearances of the peaks in the spectra are very similar to those vibrational energy transfer spectra investigated above. Briefly, at time zero, only the diagonal peak pairs show up, including the 0–1 transition (red peak 1) and 1–2 transition

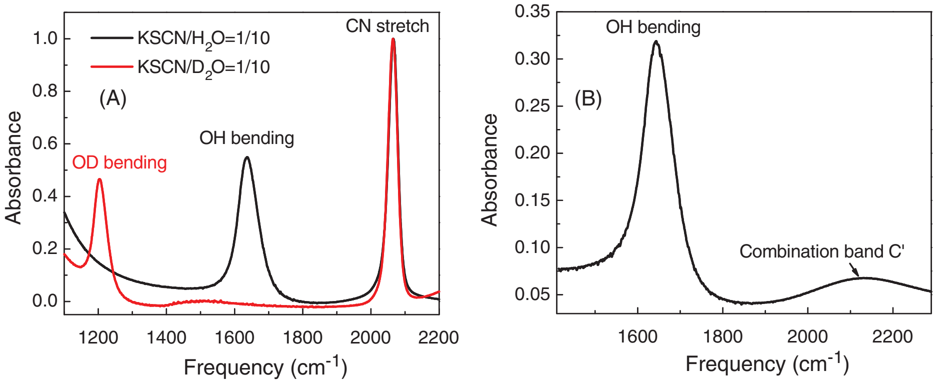

Figure 4.7. (Colour online) FTIR spectra of (A) KSCN/H$_2$O (1/10 molar ratio) and KSCN/D$_2$O (1/10) solutions, and (B) pure H$_2$O. Reprinted with permission from [170]. Copyright 2012 American Chemical Society.

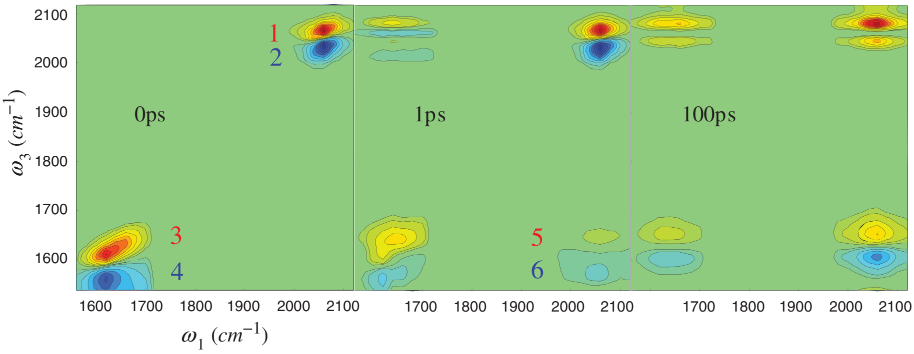

Figure 4.8. (Colour online) Waiting time dependent 2D IR spectra of the KSCN/H$_2$O (1/10 molar ratio) solution. Reprinted with permission from [170]. Copyright 2012 American Chemical Society.

(blue peak 2) of the CN stretch, as well as the 0–1 transition (red peak 3) and 1–2 transition (blue peak 4) of the OH bending. With the increase of waiting time to 1ps, vibrational energy begins to exchange. The energy transfer from the CN stretch down to the OH bending produces cross peak pairs 5 & 6. The rate of energy transfer from the OH bending up to the CN stretch is too slow to be experimentally observed, according to the detailed balance principle. The cross peaks in the frequency range of $\omega_1 = 1636\,\mathrm{cm}^{-1}, \omega_3 = 2030 \sim 2090\,\mathrm{cm}^{-1}$ in the 1ps spectrum as well as all the peaks in the 100 ps spectrum are mainly from heat induced absorption (blue) or bleaching (red), since most of the OH and CN vibrational excitations have relaxed into heat because of their short lifetimes (OH, 0.8ps; CN 2.8ps). The different frequencies between the heat induced peaks and the normal 0-1 and 1–2 transition allows the pure vibrational energy transfer from CN to OH and vibrational relaxation information to be extracted from the somewhat overlapped signals by removing the heat effect from the overall signals at the CN and OH 0–1 or 1–2 transition frequency.

$$\xleftarrow{k_{CN}} CN \underset{k_{OH\rightarrow CN}}{\overset{k_{CN\rightarrow OH}}{\rightleftarrows}} OH \xrightarrow{k_{OH}}$$

Scheme 4.2. Kinetic model of vibrational energy exchange between CN and OH.

To quantitatively analyse the energy transfer kinetics from the CN stretch to the OH bending, the vibrational energy exchange model is employed again. As shown in Scheme 4.2, the excitations of CN and OH can exchange, and both of them decay with their own vibrational lifetimes ($1/k_{OH}$ and $1/k_{CN}$) which were independently measured:

Based on the detailed balance principle (see Equation (3.2)), the energy transfer rate constant ratio was determined $k_{OH\rightarrow CN}/k_{CN\rightarrow OH} = 0.13$. Therefore, there is only one unknown parameter, the energy transfer rate constant $k_{CN\rightarrow OH}$, in the analysis. As a result, calculations yields $1/k_{CN\rightarrow OH} = 3.1 \pm 0.2$ ps with parameters $1/k_{OH} = 0.8$ ps and $1/k_{CN} = 30$ ps.

The apparent vibrational lifetime of the CN stretch in KSCN/H_2O (1/10 molar ratio) solution is determined to be 2.8 ± 0.2 ps, the energy transfer time constant of 3.1 ± 0.2 ps from the CN stretch to the OH bending indicates $\sim 90\%$ of the initial CN excitation transfers to the OH bending of the water molecule. Such an efficient energy transfer is somehow surprising with a very big donor/acceptor energy mismatch $429\,\text{cm}^{-1}$.

According to the vibrational energy transfer Equation (3.6), the frequency shift of the hydroxyl bending from $1636\,\text{cm}^{-1}$ (OH) to $1203\,\text{cm}^{-1}$ (OD) slows down the energy transfer time constant from the CN stretch to the OD bending to ~ 15 ps from the observed $1/k_{CN\rightarrow OH} = 3.1 \pm 0.2$ ps. Because the CN vibrational lifetime in D_2O is 23 ps, it is not likely for $1/k_{CN\rightarrow OD}$ to be faster than 23 ps. The above estimated 15 ps is too faster. Therefore, there must be another mechanism plays a role in the energy transfer process.

As shown in Figure 4.7(B), H_2O has a combination band C' at $\sim 2100\,\text{cm}^{-1}$. It is possible that the CN excitation can first quasi-resonantly transfer to the combination band C' through the dipole/dipole interaction mechanism. Then the excitation can be transferred intramolecularly from this combination band to the OH bending through mechanisms other than the dipole/dipole interaction, e.g. through bond or mechanical coupling or through decomposing into the fundamentals because of dephasing among the fundamentals composing the combination band. Based on Equation (3.6), the transfer rate from CN to the combination band C' (resonant) is about 30 times faster than that directly from CN to the OH bending, where we have assumed the only differences betweens these two transfers are the transition dipole moments ($(\mu_{OH}/\mu_{com})^2 = 10$) and the energy mismatches (0 and $429\,\text{cm}^{-1}$). D_2O doesn't have such a bridge mechanism because it doesn't have a combination band of which the frequency overlaps with that of the CN stretch. Therefore the CN stretch relaxes much slower in D_2O. In pure H_2O, the transfer of combination band C' excitation to the OH bending was not observed, probably because the transition dipole moment of combination C' is so weak that the energy transfer peak is too small to be observed.

4.2.2. *Vibrational energy dynamics of the NH4SCN/H2O (1/10) solution*

Figure 4.9 displays the FTIR spectrum of NH_4SCN/H_2O (1/10 molar ratio) solution [170]. Besides the energy accepting modes in H_2O molecules, both the combinational band C of NH_4^+ at $\sim 2060\,\text{cm}^{-1}$ (shown in the spectrum of NH_4Br) and NH bending at $1460\,\text{cm}^{-1}$

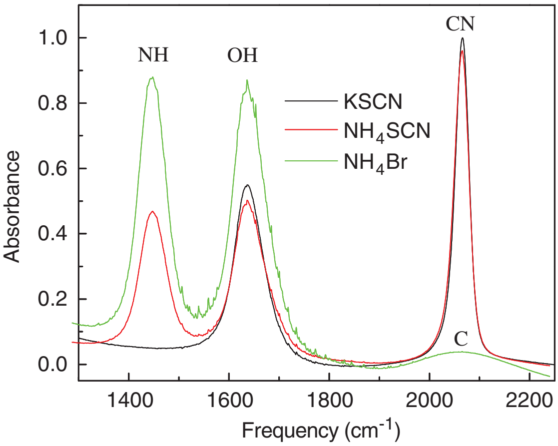

Figure 4.9. (Colour online) FTIR spectra of the NH_4SCN/H_2O (1/10 molar ratio) solution (red), the $KSCN/H_2O$ (1/10) solution (black) and a NH_4Br/H_2O solution (green). Reprinted with permission from [170]. Copyright 2012 American Chemical Society.

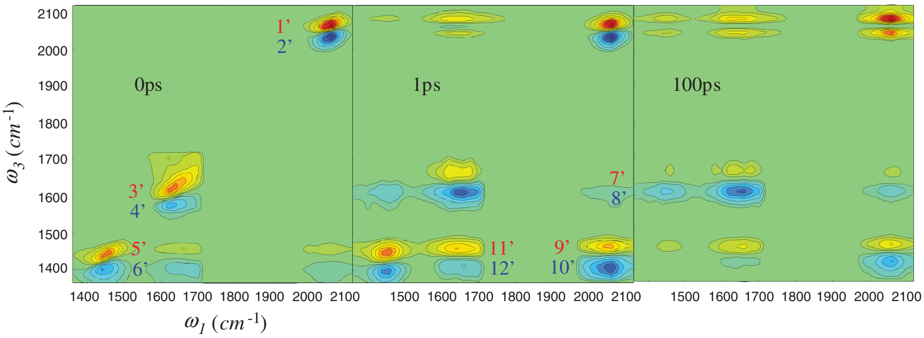

Figure 4.10. (Colour online) Waiting time dependent 2D IR spectra of the NH_4SCN/H_2O (1/10) solution. Reprinted with permission from [170]. Copyright 2012 American Chemical Society.

may provide additional energy acceptors for the excited CN stretch of SCN^-. Therefore, if the molecules in the solutions are randomly distributed and can fast switch their locations, the vibrational relaxation of the CN stretch would be expected to be faster in the NH_4SCN solution than in the KSCN solution for the more energy acceptors. However, as shown below, experimentally the vibrational relaxation (3.1ps) of CN stretch in the NH_4SCN solution is actually a little slower than that (2.8ps) in the KSCN solution, for the NH_4^+ competing with H_2O to bind to SCN^- and with a slower energy transfer rate.

Figure 4.10 displays the 2D IR spectra of the $KSCN/H_2O$ (1/10) solution [170]. Similar to Figure 4.8, the diagonal peak pairs $1'$&$2'$, $3'$&$4'$, $5'$&$6'$ belongs to the 0–1&1–2 transitions of the CN stretch, the OH bending, and the NH bending, respectively. Cross peak pairs $7'$&$8'$ are from the vibrational energy transfer from CN to OH, and the heat effect inducing OH bending absorption change. Cross peak pairs $9'$&$10'$ are from the vibrational coupling between CN and NH and between combination band C and NH, the vibrational energy transfer from CN to NH and from C to NH, and the heat effect inducing NH bending absorption change. Cross peak pairs 11′&12′ are from the vibrational coupling between NH and OH, the vibrational energy transfer from OH to NH, and the heat effect inducing NH bending absorption change. The energy transfer from C to NH produces peaks at the same frequencies as the transfer from CN to NH. In the CN/NH and CN/OH energy transfer kinetic analysis, we removed the possible contributions of C to NH and OH transfers by subtracting the signal of a NH_4Br/H_2O (1/10) solution from that of the NH_4SCN/H_2O solution of the same concentration and the same NH bending optical density.

Different from that in $KSCN/H_2O$ solution, the vibrational energy exchange model is a little complicate in the NH_4SCN aqueous solution. Two intermolecular acceptors, OH of H_2O and NH of NH_4^+, are competing for the CN excitation. In addition, the energy of OH and NH can also exchange. These dynamic processes are coupled to each other, which brings difficulties to the quantitative analysis. Fortunately, our experiment results showed that the lifetime of OH bending is ~0.8 ps, while the energy transfer time from OH to NH is 4ps, indicating only ~12% of the OH bending excitation will be transferred to the NH bending. Accordingly, the energy transfer rate from NH up to OH can be determined by detailed balance, which is about 10 ps, much slower than the lifetime of either the OH bending (0.8ps) or the NH bending (1.3ps). In other words, only a small portion of the OH or NH bending vibrational excitation can exchange between them, and omitting the energy exchange between the OH and NH bendings in processing the energy transfers from CN to OH and NH will not cause a big uncertainty. The kinetic equations are then simplified into two sets of independent equations: one is for CN to NH, and the other is for CN to OH. Each set is similar to that for the CN/OH transfer in the $KSCN/H_2O$ solution.

Based on the above analysis, solving the kinetic equations yields the energy transfer rate $1/k_{CN\to OH} = 6.3 \pm 0.5$ ps with parameters $1/k_{OH} = 0.8$ ps, and $1/k_{CN} = 5.5$ ps, and $1/k_{CN\to NH} = 7.0 \pm 0.5$ ps with parameters $1/k_{OH} = 1.3$ ps, and $1/k_{CN} = 5.2$ ps. Different $1/k_{CN}$ values were used in the calculations because the relaxation of CN includes three parts: (1) to NH, (2) to OH, and (3) to other modes (assumed to be 30ps). In calculating either the CN/NH or the CN/OH energy transfer rate constant, $1/k_{CN}$ is the sum of two contributions (to other modes + to OH or to NH). The results indicate that 47% of the CN excitation flows to the OH bending, and 43% flows to the NH bending.

The most obvious explanation for the above measurement is that, NH_4^+ directly competes with H_2O for binding to SCN^-. As a consequence, nearly one half of the H_2O molecules of the SCN^-/H_2O binding sites in the KSCN solution are replaced by the NH_4^+ cations in the NH_4SCN solution, and the CN/OH energy transfer efficiency drops for about one half (~47%) in NH_4SCN/H_2O (1/10) solution compared to that in $KSCN/H_2O$ (1/10) solution (~90%). Many concerns about this conclusion have been addressed carefully [170].The result indicates that the NH_4^+/SCN^- binding affinity is about 18 times stronger than that of H_2O/SCN^- binding in the aqueous solutions.

4.3. *Ion/protein-building-block molecular interactions in aqueous solutions*

The effects of salts on protein solubility and conformational stability have been of great research interest for decades. However, whether salts change protein properties primarily through direct interactions [171,172] or indirectly via modifying the water structure [173,174] is still in the debates. Recently, the direct ion-biological molecule interactions began to be recognised as a very important factor for the protein stability and solubility [171,175–179]. In the previous section, we demonstrated that there is a strong interaction between SCN^- and NH_4^+ in the NH_4SCN/H_2O solution, where the NH_4^+ can be seen as a model compound to represent the positively charged groups of proteins. By using the vibrational energy exchange method, we are able to determine the binding affinity between a series of model compounds representing the typical building blocks of a protein and a strong denaturant, SCN^- anion, in aqueous solutions, and hence obtain the relative priorities of these model compounds in interacting with the SCN^- anion.

4.3.1. *Interactions between SCN^- and amino acids*

We have used competing vibrational energy acceptors to determine the binding between SCN^- and NH_4^+ relative to that between SCN^- and H_2O. However, this method cannot be used in other organic model compounds representing the polar functional groups of a typical protein, because the severe spectral overlaps among the OH bending, the NH bending, the C=O stretch and other modes of these organic molecules. Therefore, another approach is required to investigate these molecules.

As introduced above, thiocyanate anions in the ion clusters of KSCN aqueous solutions can exchange vibrational energy. This phenomenon can be used to determine the relative interaction strength between a model compound and SCN^-: If there is no specific interaction between the ions and the model compound, the ion clusters would be expected to grow as a result of concentration reduction of water by additional model compound, leading to a faster observed vibrational energy transfer among the ions; If the ion clusters interact strongly with the model compound, then ions might be removed from the clusters or the model compound may insert into the ion cluster and increase the average distance among the SCN^- anions and also quench the SCN^- excitation. This will result in a slower observed vibrational energy transfer among the ions.

Figure 4.11(A) displays 2D IR spectra of 1:1 $KSCN/KS^{13}C^{15}N$ aqueous solutions with the addition of different amounts of proline [180]. As elaborated in the above sections, the cross peaks $5' \sim 8'$ are mainly from vibrational energy exchange between SCN^- and $S^{13}C^{15}N^-$ at relatively short waiting times. At longer times, heat effects grow in, which can affect peaks 5′, 7′&8′. Peak 6′ is hardly affected because of its lower detection frequency. Therefore, the intensity of peak 6′ can be regards as a criterion to determining the energy exchange rate between SCN^- and $S^{13}C^{15}N^-$.

The simple inspection of the intensity of peak 6′ in Figure 4.11(A) reveals that the vibrational energy exchange between SCN^- and $S^{13}C^{15}N^-$ slows down by $\sim 50\%$ with the addition of 4M proline. This result is a little similar to that in 4M NH_4SCN/H_2O solution as elaborated in the previous section, where more than 50% of the SCN^- anions are bound to NH_4^+. Proline has an R-NH_2^+ cation, which is expected to bind to SCN^- in a way similar to NH_4^+, and hence results in a slower observed vibrational energy transfer among the SCN^- anions. Moreover, as shown in Figure 4.11(B), the slowdown of energy transfer with the addition of Proline is not an exception. By adding 2M glycine, 2M cysteine or 2M lysine into $KSCN/KS^{13}C^{15}N$ aqueous solutions, the intensity of the vibrational energy transfer peak 6′ can also decrease dramatically in each case, indicating a slower energy transfer. Additional control experiments further demonstrated that it is thiocyanate/ammonium interaction not K^+/carboxylate anion interaction that is responsible for the observed slower energy transfer [180].

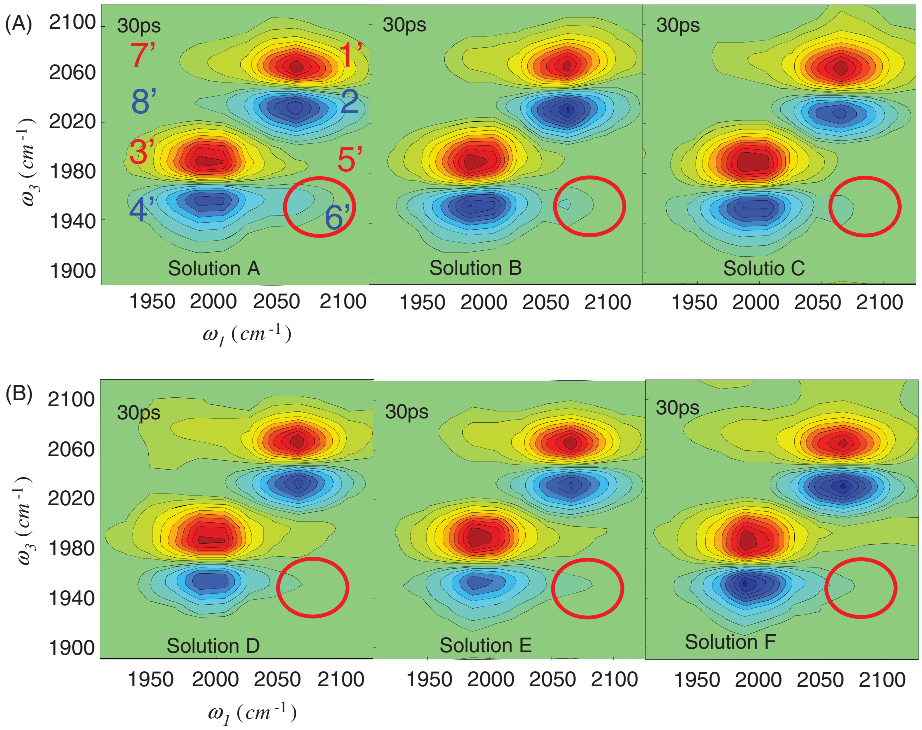

Figure 4.11. (Colour online) (A) The proline concentration dependence of 2D IR spectra at 30ps of solutions: **Solution A** (Pro:KSCN:KS^{13}C^{15}N:D$_2$O=0:1:1:20); **Solution B** (Pro:KSCN:KS^{13}C^{15}N:D$_2$O = 1:1:1:20); and **Solution C** (Pro:KSCN:KS^{13}C^{15}N:D$_2$O = 2:1:1:20). (B) 2D IR spectra at 30ps of solutions: **Solution D** (Gly:KSCN:KS^{13}C^{15}N:D$_2$O=1:1:1:20); **Solution E** (Cys:KSCN:KS^{13}C^{15}N:D$_2$O = 1:1:1:20); and **Solution F** (Lys:KSCN:KS^{13}C^{15}N:D$_2$O = 1:1:1:20). Red rings highlight Peak 6′. Reprinted with permission from [180]. Copyright 2012 American Chemical Society.

4.3.2. *Interactions between SCN$^-$ and N-H group in the backbone*

The salt/amide backbone interactions were also investigated with a similar strategy. As displayed in Figure 4.12(B) and (C) [180], adding 4M NMA (N-methylacetamide) into KSCN/KS^{13}C^{15}N aqueous solutions also slightly slows down the vibrational energy exchange.

NMA has three possible sites binding to thiocyanate: the carbonyl group, the amide bond and the N-H group. We first used acetone to represent the carbonyl group. As shown in Figure 4.12(D), adding 4M acetone into KSCN/KS^{13}C^{15}N aqueous solutions produces negligible change in the vibrational energy transfer rate among the thiocyanate anions, implying that the interactions between the carbonyl group and the ions are very weak. Adding 4M DMF (HCON(CH$_3$)$_2$, Figure 4.12(E)) has a similar but very slight effect. However, adding 4M formamide (HCONH$_2$, Figure 4.11(F)) produces a clear decrease in the intensity of peak 6′, indicating a stronger interaction between the ions and formamide. Formamide has two more N-Hs than DMF and one more N-H than NMA. The results in Figure 4.12(B), (E) and (F) imply that the N-H group plays an important role for the amide group binding to the ions. Because formamide is less electron-rich than the other

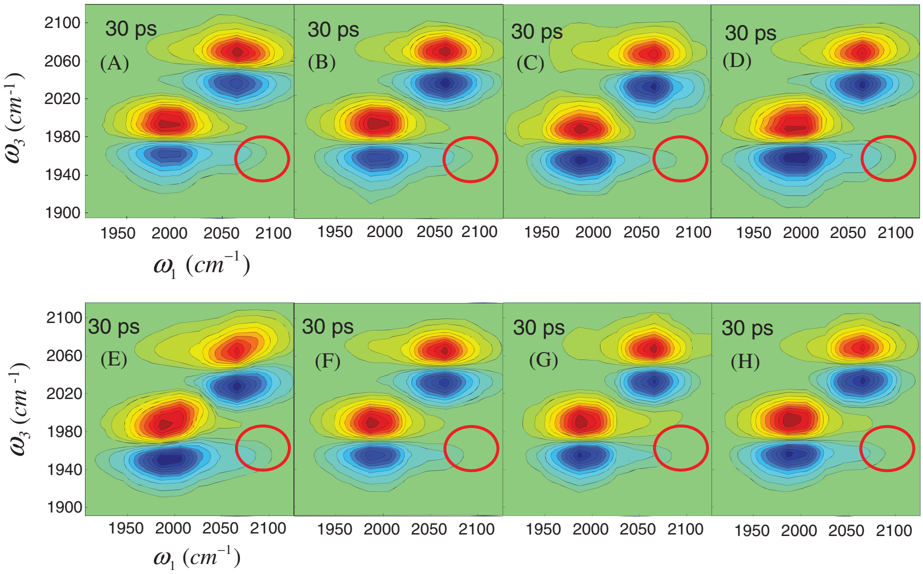

Figure 4.12. (Colour online) 2D IR spectra at 30ps of (A) **Solution A** (KSCN:KS^{13}C^{15}N:D$_2$O = 1:1:20); (B) **Solution J** (NMA:KSCN:KS^{13}C^{15}N:D$_2$O = 2:1:1:20); (C) **Solution K** (NMA: KSCN:KS^{13}C^{15}N:D$_2$O = 4:1:1:20); (D) **Solution L** (Acetone:KSCN: KS^{13}C^{15}N:D$_2$O = 2:1:1:20); (E) **Solution M** (DMF:KSCN:KS^{13}C^{15}N:D$_2$O = 2:1:1:20); (F) **Solution N** (HCONH$_2$:KSCN:KS^{13}C^{15}N:D$_2$O = 2:1:1:20); (G) **Solution O** ((C$_2$H$_5$)$_2$NH:KSCN: KS^{13}C^{15}N:D$_2$O = 2:1:1:20); and (H) **Solution P** ((C$_2$H$_5$)$_3$N:KSCN:KS^{13}C^{15}N:D$_2$O = 2:1:1:20). Reprinted with permission from [180]. Copyright 2012 American Chemical Society.

two molecules, the ions binding to its N-Hs are probably the thiocyanate anions (to H) rather than the K$^+$ cations (to the lone electron pair).

The conclusions are supported by further experiments. Adding 4M diethyl amine ((C$_2$H$_5$)$_2$NH, DEA) clearly reduces the intensity of Peak $6'$ (Figure 4.12(G)), indicating a strong interaction between the amine group and the ions, while adding 4M triethylamine ((C$_2$H$_5$)$_3$N) doesn't change the intensity of Peak $6'$ (Figure 4.12(H)) as much, indicating the insignificance of the interaction between the lone electron pair and K$^+$. The results also explain why the effect of lysine is bigger than proline (Figure 4.10(B)), probably because lysine has an extra amine group which is able to bind to thiocyanate. It is interesting to note that in solutions with amino acids (proline), NH$_4^+$, and NMA, the CN stretch 0–1 transition central frequency red shifts for about 2 cm^{-1} from FTIR measurements compared to that in the 4M KSCN solution. In contrast, adding 4M CH$_3$COOK or acetone doesn't cause such a frequency shift. The results show that the molecules with the positively charged groups or the amide groups probably have a bigger effect on the CN vibration of SCN$^-$ than the molecules without them in aqueous solutions.

To quantitatively analyse the vibrational energy exchange kinetics, a similar location-energy-exchange kinetic model as introduced in Section 4.1 is employed here. In the model, the solution was simplified to contain three different components: water-bound thiocyanate anions and model compounds-bound thiocyanate anions that cannot exchange vibrational energy, and clustered thiocyanate anions that can exchange vibrational energy. All of the thiocyanate anions contribute to the diagonal peak pairs in 2D IR measurements, but only the clustered anions contribute to the off-diagonal peak pairs. The vibrational excitations of the anions decay with their own lifetimes. Here, we have assumed that once a thiocyanate anion is bound to a model compound, it will not be able to exchange energy with other anions because the energy from this bound anion will probably transfer to the model compounds, similar to the situation in the NH_4SCN/H_2O solution.

Quantitative analyses on the data based on the kinetic model show that, corrected with the transition dipole moment and refractive index changes, the concentrations of thiocyanate clusters (the ratio of clustered over all thiocyanate) in **Solutions** with different compounds are 67% ± 2% (no additive), 44% ± 4% (2M Pro), 35% ± 5% (4M Pro), 44% ± 4% (2M Gly), 35% ± 5% (2M Cys), 32% ± 7% (2M Lys), 58% ± 4% (4M NMA), 52% ± 4% (4M FMA), and 62% ± 4% (4M Acetone) respectively. The results indicate that substantial portions (35 ~ 75%) of added amino acids have bound to the salt ions in the solutions.

Moreover, a simple inspection on the vibrational energy exchange 2D IR spectra can also provide us a qualitative picture about the relative binding strengths of different model compounds with thiocyanate in aqueous solutions. To quantitatively describe the relative binding affinity of the model compounds to the thiocyanate anions, we constructed an equilibrium model consistent with the kinetic model to analyse the vibrational energy exchange results [180]. In summary, quantitative analysis shows that the interaction strength between the thiocyanate anions and the charged amino acid residues is about 20 times bigger than that between the water molecules and the amino acids, and about 5 ~ 10 times larger than that between the anions and the neutral amide groups. The affinity ratios lead to an interesting scenario: if the measured affinities of the model compounds are similar to those of functional groups of proteins, the amide groups can bind to the SCN^- anions during protein denaturation with a similar or even larger probability than the positively charged groups if a large number of the amide groups can expose to the water phase during the denaturation.

5. Molecular conformations probed with MDVS

Fast molecular conformational fluctuations in condensed phases play critical roles in many important chemical and biological activities [40,181], e.g. chemical reactions, protein foldings, and molecular recognitions. Tremendous efforts have been devoted to develop tools to monitor the real time three-dimensional (3D) molecular conformations in these biological processes. Among many powerful techniques developed, the nuclear magnetic resonance (NMR) methods are the most successful so far. However, the low intrinsic temporal resolution of NMR provides only longtime average containing no information about faster structural fluctuations.

As introduced in the previous sections, MDVS methods have potential to determine 3D molecular conformations through determining the relative orientations (see Equation (2.54)) of the transition dipole moments of vibrations. In order to obtain the complete 3D conformations of a molecule, vibrations covering all chemical bonds of which the frequencies reside in a wide Mid-IR range must be simultaneously investigated. Information from one or a few modes can only provide partial knowledge about the structure of the molecule. Compared to NMR, MDVS methods have unique advantages for their sensibility to dynamics on timescales 6 to 10 orders of magnitude faster.

As introduced in Section 2.3, most current 2D IR methods lack sufficient pump power with tunable frequencies covering the whole mid-IR range, limiting their applications on investigating 3D molecular conformations. With our recently designed multiple-mode method which has sufficient power covering almost the entire mid-IR range, we are now positioned to explore this new territory. In this chapter, we will introduce some of our recent progresses on determining 3D molecular conformations in various systems with the new experimental setup.

5.1. *Conformation of 1-cyanovinyl acetate in CCl_4 solution*

1-cyanovinyl acetate [72] is the first molecule we chose to demonstrate the principle of determining molecular conformations with the multiple-mode multiple dimensional vibrational spectroscopy. The molecular formula and FTIR spectrum of 1-cyanovinyl acetate in CCl_4 is shown in Figure 5.1. This molecule has several advantages to serve as a model system for the purpose: (1) it is small enough that current ab initio calculations can relatively precisely predict many of its molecular properties; (2) it has several possible conformations; (3) it has many typical vibrational groups, e.g. $C = C - H$, $C - C - H$, $C \equiv N$, $C = C$, $C = O$, and $C - O$; (4) these vibrational groups cover all the molecular space, and therefore it is possible that the three-dimensional conformations of this molecule can be obtained by investigating the vibrations of these groups; and (5) as shown is Figure 5.1, these vibrational groups covers a big vibrational frequency range ($>2000\,cm^{-1}$) and a big vibrational spatial separation (more than three chemical bonds), which allows us to explore the sensitivity and potential of our approach.

5.1.1. *Possible conformations*

The structures of 1-cyanovinyl acetate were determined with density functional theory (DFT) calculations. The calculated conformations are displayed in Figure 5.2 [72].

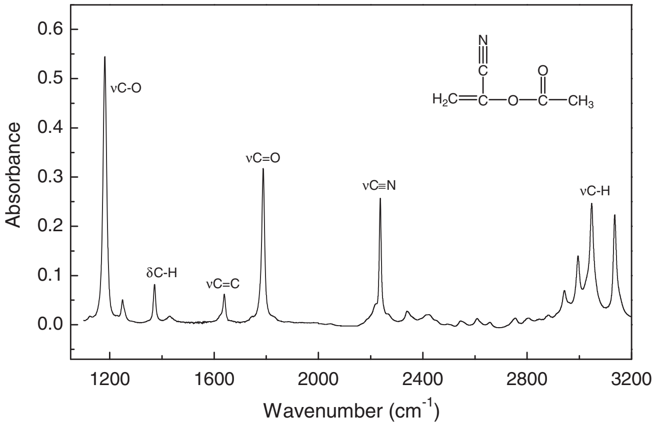

Figure 5.1. FTIR spectrum of 1-cyanovinyl acetate in CCl_4. Inset: molecular formula of 1-cyanovinyl acetate. The peak assignments: C=O ($1788\,cm^{-1}$), C=C ($1639\,cm^{-1}$), C≡N ($2236\,cm^{-1}$), C–H (2942, 2995, 3047 and $3135\,cm^{-1}$), C–O ($1180, 1248\,cm^{-1}$) stretches and the C–H bending (1372 and $1430\,cm^{-1}$). Reprinted with permission from [72]. Copyright 2011 American Chemical Society.

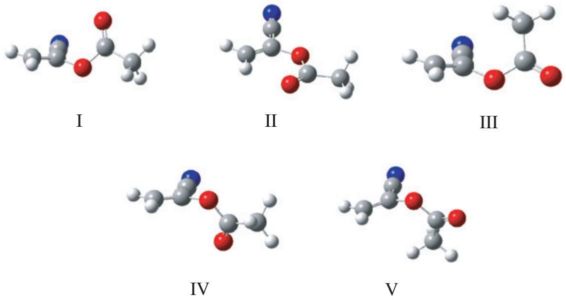

Figure 5.2. (Colour online) The B3LYP/6-311++G(d,p) optimised structures of the 1-cyanovinyl acetate in the CCl_4 phase using the CPCM model. Reprinted with permission from [72]. Copyright 2011 American Chemical Society.

Table 5.1. The calculated energies, bond lengths and dihedral angles (degree) for the five optimised conformers of 1-cyanovinyl acetate calculated at B3LYP 6-311++G(d,p) level in CCl_4 using SCRF-CPCM. Reprinted with permission from [72]. Copyright 2011 American Chemical Society.

Conformers	I	II	III	IV	V
ΔE/Kcal mol^{-1}	0.00	0.97	4.68	0.00	4.68
(C-C–O-C)/Deg.	66	−180	75	−66	−75
(C–O-C=O)/Deg.	3	0	−180	−3	180
Bond lengths/Å	C=C (1.33), C≡N (1.16), C–O (1.39), C=O (1.21), C-C(C≡N) (1.44), C-C (CH_3) (1.50), C–H (CH_2) (1.08), C–H (CH_3) (1.09)				

The calculation results show five possible conformers for 1-cyanovinyl acetate in CCl_4, which are the isomerisation results rotating around the two $C-O$ single bonds. Conformer I and conformer IV are mirror symmetric to each other. They are the most stable conformations. Conformer III and V have much higher energy than others (~5 kcal/mol). Based on the calculated energy values, they are negligible conformers at room temperature. Table 5.1 gives the calculated energies, bond lengths and key dihedral angles of the 1-cyanovinyl acetate molecule [72].

5.1.2. *Cross angles between different vibrational modes*

Different from the linear FTIR spectrum shown in Figure 5.1 where only the 0–1 transition frequencies of vibrational modes of the molecule are acquired, the multiple-mode 2D IR spectrum in Figure 5.3 provides much more molecular information [72]. Both 0–1 and 1–2 vibrational transition frequencies are obtained from the positions of the diagonal red and blue peaks. The vibrational coupling anharmonicities among vibrational modes are manifested by the positions of the off-diagonal peak pairs. The relative orientations of the vibrations are obtained from the polarisation-selective measurements of the off-diagonal peak intensities, which will be elaborated in follow.

We have introduced, when two vibrational modes are anharmonically coupled with each other and the coupling is sufficiently strong (e.g. $> 1\,\text{cm}^{-1}$), off-diagonal peak pairs

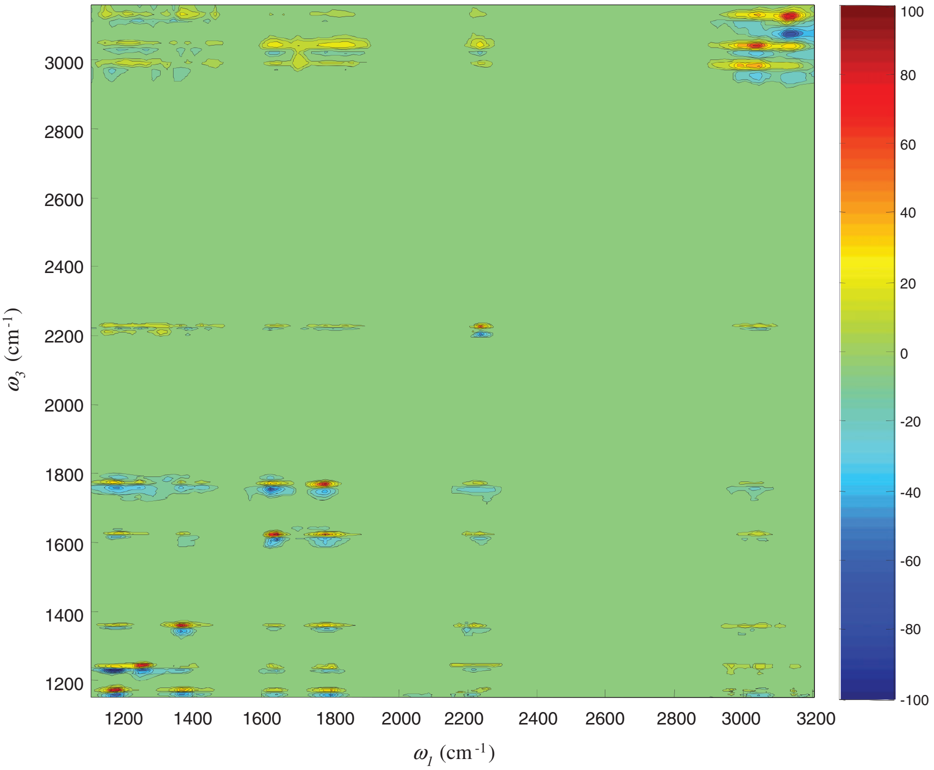

Figure 5.3. (Colour online) 2D-IR spectrum of 1-cyanovinyl acetate at waiting time 0.2ps. The relative intensities of peaks are adjusted to be comparable. Each contour represents 10% amplitude change. Reprinted with permission from [72]. Copyright 2011 American Chemical Society.

will appear in the 2D IR spectra, as demonstrated in Figure 5.4(a) (an enlarged part of Figure 5.3) for the C=C and C=O modes of 1-cyanovinyl acetate. The amplitudes of the off-diagonal peaks are dependent on the polarisations of the exciting and probing beams [8,13,182,183], as shown in Figure 5.4(b). This is because the transition dipole moments of the two coupled modes are aligned to each other with certain cross angle which is determined by the molecular conformation. As derived in Section 2.4, by changing the polarisations of the laser beams, the vibration cross angles θ can be straightforwardly determined by the polarisation-selective pump/probe signal based on Equation (2.54), which can be rewritten by the following form

$$\frac{P_{\perp}}{P_{\parallel}} = \frac{2 - \cos^2\theta}{1 + 2\cos^2\theta} \tag{5.1}$$

where $P_{\parallel}$ and $P_{\perp}$ are peak intensities from experiments with parallel and perpendicular pump/probe polarisations, respectively.

From the experimental measurements (Figure 5.4(b)), the averaged $P_{\perp}/P_{\parallel}$ intensity ratio is determined to be 1.4 ± 0.1. According to Equation (5.1), the angle between the transition dipole moments of C=C and C=O can be determined as $66 \pm 3°$. To verify the

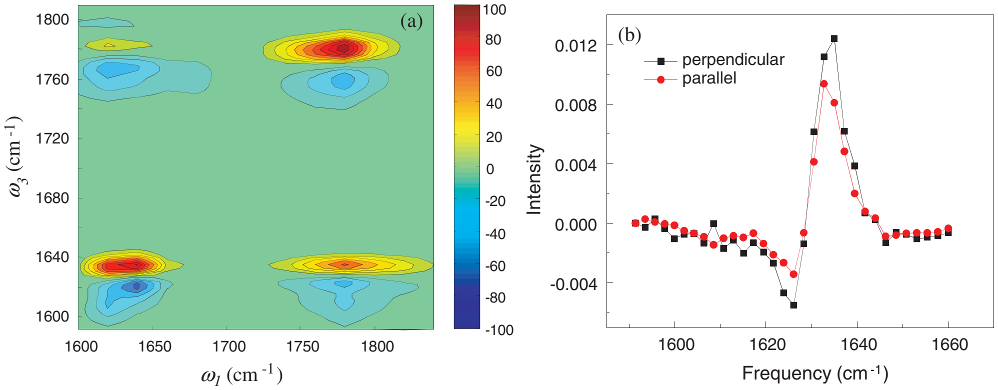

Figure 5.4. (Colour online) (a) Enlarged 2D-IR spectrum of 1-cyanovinyl acetate at waiting time of 0.2 ps in the C=C and C = O frequency range. The detection polarisation is in parallel with the pump. Each contour represents 10% amplitude change. (b) Off-diagonal pump-probe spectra with probe in the C=C region and pump at 1784 cm^{-1} (C = O) measured at the 0.2 ps delay. Both the parallel and perpendicular data are shown. Reprinted with permission from [72]. Copyright 2011 American Chemical Society.

Table 5.2. Transition dipole moment angles between coupled vibrational modes of the 1-cyanovinyl acetate molecule determined from the anisotropy measurement. The anisotropy data were obtained at waiting time of 0.2 ps. Reprinted with permission from [72]. Copyright 2011 American Chemical Society.

Pair number	Coupled modes	Relative angle (degree)	Pair number	Coupled modes	Relative angle (degree)
1	C=C/C=O	64 ± 3	10	C=O/CH$_2$(as)	58 ± 3
2	C=C/C≡N	43 ± 3	11	C=O/CH$_3$(as)	55 ± 3
3	C=C/C–O(as)	37 ± 5	12	C≡N/C–O(as)	69 ± 3
4	C=C/CH$_2$(as)	37 ± 5	13	C≡N/CH$_2$(as)	47 ± 5
5	C=C/CH$_2$(ss)	43 ± 5	14	C≡N/CH$_2$(ss)	37 ± 5
6	C=C/CH$_3$(as)	37 ± 5	15	C≡N/CH$_3$(as)	43 ± 5
7	C=O/C≡N	58 ± 3	16	C–O(as)/CH$_2$(as)	55 ± 3
8	C=O/C–O(as)	78 ± 3	17	C–O(as)/CH$_2$(ss)	51 ± 3
9	C=O/C–O(ss)	47 ± 5			

value that we obtained, the other off-diagonal blue peak (1639 cm^{-1}, 1776 cm^{-1}) was also measured. The averaged $I_\perp/I_\parallel$ intensity ratio is determined to be 1.3 ± 0.1. The angle between the transition dipole moments of C=O and C=C is determined to be 64 ± 3°, which is consistent with the above value. The red cross peaks and blue cross peaks give the same vibrational cross angle. However, the cross red peaks can come from many contributions as discussed in Section 2. In particular, the bleaching effect from the relaxation induced heat can change the anisotropy value of the red cross peaks. Therefore, for modes with relatively short vibrational lifetimes, blue peaks are recommended to be used rather than the red peaks in analyzing the anisotropy.

The transition dipole moment cross angles of other coupled modes were also obtained using the same procedure. The results are listed in Table 5.2 [72]. However, there is one question needed to be clarified. As shown before, the molecular rotation can also cause a change to the anisotropy. In the system studied here, the rotational time constant of 1-cyanovinyl acetate molecule was determined to be 4.0 ps by measuring the diagonal anisotropy. In our cross angle calculation procedures, the transition dipole moment angles of all the coupled modes are determined at waiting time 0.1 ~ 0.2 ps. In our experiments, the pump pulse is ~ 0.8 ps and the probe pulse is ~ 0.14 ps, the overlapping between them causes a temporal uncertainty of about 0.2 ~ 0.3 ps. Because the molecular rotation is relatively slow, this temporal uncertainty causes an uncertainty of ~ 10 degrees in the determined transition dipole moment angle.

5.1.3. *Translation from vibrational angles to molecular conformations*

One major difficulty in converting the vibrational cross angles into molecular structures is that the vector direction of transition dipole moment of a vibrational mode is different from that of the chemical bond which is mainly responsible for the vibration. Even for a highly localised mode, its direction is still slightly different from the bond orientation, because the observed modes are always normal modes. Therefore, the vibration cross angles determined can't be immediately translated into the relative orientations of the chemical bonds. However, on one hand, corresponding to a well-defined molecular conformation, there are one and only one set of spatially well-defined vibrations because the vibrational motions are purely determined by the bond orientations. On the other hand, corresponding to one set of spatially well-defined vibrations, there are one and only one set of chemical bond orientations of the molecule. Therefore, the translation of the vibration cross angles into relative bond orientations is more like converting data from one coordinate system to another, though the conversion of the coordinate systems (vibrational coordinates into atomic coordinates) is not very straightforward.

The commercial ab-initio calculation program Gaussian has such a function to translate atomic coordinates into vibrational coordinates. Specifically, the program in Gaussian can first optimise the molecular conformation, and then calculate all properties including the vibration angles based on the optimised structure. Such a calculating procedure determines that the translation of the experimental observables into the molecular conformations is more like a fitting procedure: instead of using the energy minimum (default) as the structural criterion, the experimental vibrational cross angles will serve as the criterion to determine which calculated conformations have vibrational cross angles closest to that experimentally observed. The general calculation procedure is to preset all possible conformations based on the chemical bond rotational degrees of freedom, and then calculate their vibrational cross angles until the closest values to the experimental results are found.

For 1-cyanovinyl acetate, the major degree of freedom to generate different conformations is the rotations around the two $C-O$ single bonds. We therefore optimised the molecular conformations at different C–C/C–O (of the acid group) dihedral angles, and calculated their minimum energy and vibrational cross angles of the 17 pairs of normal modes experimentally investigated. The energy minima and the deviation *Ers* between the calculated and experimental vibrational cross angles are shown in Figure 5.5 [72], where *Er* is defined in the following equation

$$Er = \frac{\sum_{i=1}^{m} |A_i^C - A_i^E|}{m}, \tag{5.2}$$

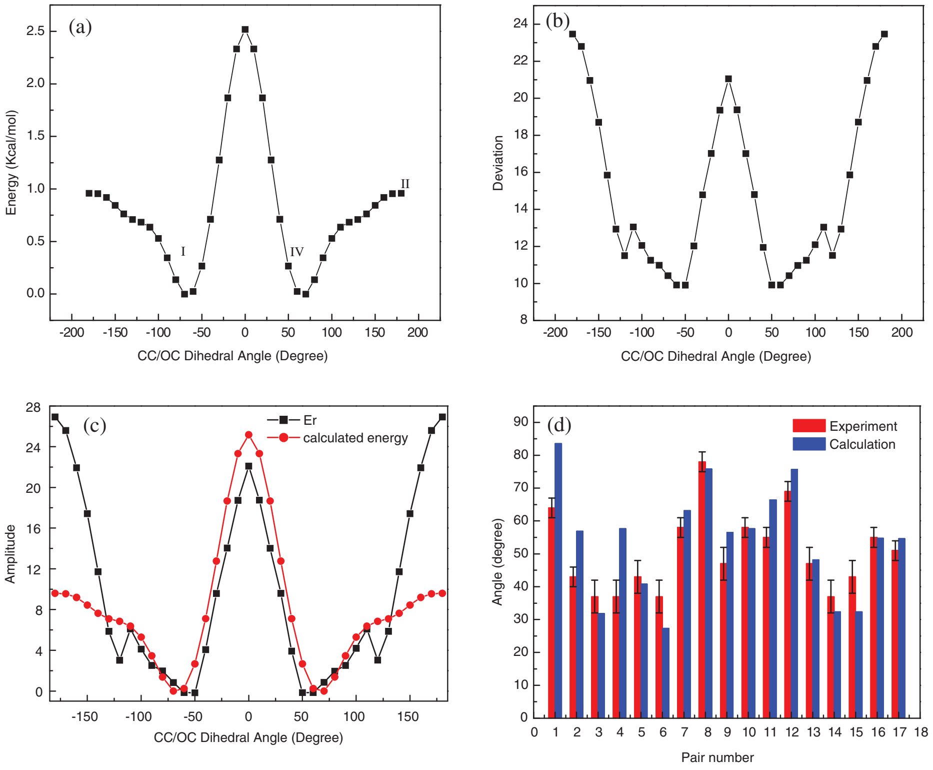

Figure 5.5. (Colour online) (a) Calculated potential energy surface (PES) of the 1-cyanovinyl acetate in CCl_4. (b) Deviation *Er* vs the CC/OC dihedral angle. (c) Rescaled PES and *Er*. (d) Calculated and experimental average vibrational cross angles of the 17 coupling pairs. Reprinted with permission from [72]. Copyright 2011 American Chemical Society.

where A_i^C is the calculated vibrational cross angles of ith pair of normal modes. A_i^E is the experimental value listed in Table 5.2. m is the number of the coupling pairs, which is 17 in this study.

As shown in Figure 5.5(c), it is amazing that calculations based on both the energy minimum and experimental vibrational cross angles criteria give almost the same most probable conformations. For the most probable conformations (almost the energy minima), the calculated vibrational cross angles are about 10 degrees different from the experimental results on average. To further analyse the calculated and experimental vibrational cross angles, we define another parameter to account for the distribution of conformations, the averaged angle $\overline{A}$ as

$$\overline{A} = \frac{\sum_{i=1}^{n} A_i \cdot \rho_i}{\sum_{i=1}^{n} \rho_i}, \quad \rho_i = \exp\left(-\frac{E_i - E_0}{kT}\right), \tag{5.3}$$

where E_i is the calculated energy of conformation i. E_0 is the lowest energy. ρ_i is the Boltzmann distribution. The calculated $\overline{A}$ and experimental vibrational cross angles are plotted in Figure 5.5(d). For most coupling pairs, the difference between calculated and experimental results is only a few degrees. Within experimental uncertainty (~10 degrees), the consistency between the calculated and experimental results is excellent.

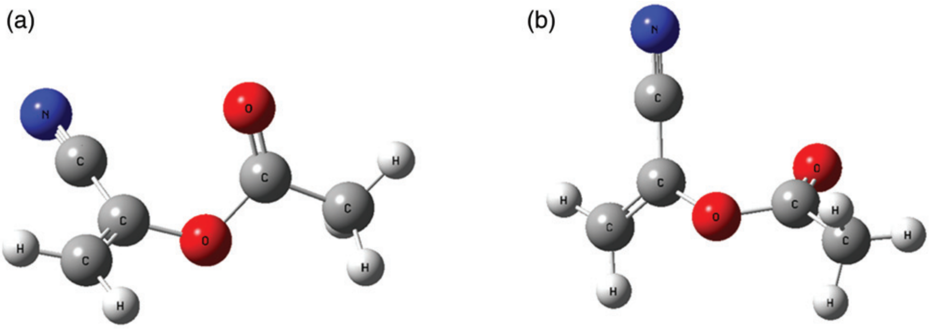

Figure 5.6. (Colour online) The most probable molecular conformations determined by the experimental vibrational angles. (a) is with a C–C/C–O (of the acid group) dihedral angle ∼50 degree and (b) is the mirror symmetric conformation of (a). Within experimental and calculated uncertainties, we consider these two conformations are identical to I and IV in figure 5.2. Reprinted with permission from [72]. Copyright 2011 American Chemical Society.

Based on the above analysis, the most probable molecular conformations experimentally determined are two conformations (in Figure 5.6 [72]) with the dihedral angles of C−C/C−O (of the acid group) around 50 degrees and −50 degrees, respectively. However, the energy difference between these two conformations and I and IV in Figure 5.1 is smaller than 0.1 kcal/mol. Within experimental and calculation uncertainties, we would consider that the experimentally most probable conformations are also the calculated most stable conformations.

In addition, we also explored the molecular conformation dependence of the vibrational and coupling anharmonicities [72]. In principle, these two types of anharmonicities are also correlated to the molecular conformations and vibrational spatial separations. Different from the vibrational angle results in Figure 5.5, no clear correlation between molecular conformations and anharmonicities was found. From these observations, it seems that without further theoretical developments, it is difficult to predict molecular conformations based on vibrational anharmonicities (at least for the molecule studied here). For ultimately utilising the vibrational anharmonicitiy information to help determine molecular conformations, we believe that in addition to the advances of theory, the accumulation of database about correlations among well-defined chemical bond distances and orientations and the vibrational anharmonicities and couplings are also very important, which will be pursued in the near future.

5.2. *Molecular conformations and dynamics on surfaces of gold nanoparticles*

Metallic nanoparticles have been intensively investigated over the past three decades for their potential applications on catalysis, biological processes, to nano-photoelectronics [184–191]. Knowledge about molecular conformations and energy dynamics of adsorbed molecules on surfaces of these nanoparticles is critical for many applications [189,192,193]. In general, such molecular information is difficult to be determined by traditional methods, e.g. XRD, NMR or SFG [91]. However, as will be introduced in this section, valuable information of this sort can be successfully determined by MDVS [91].

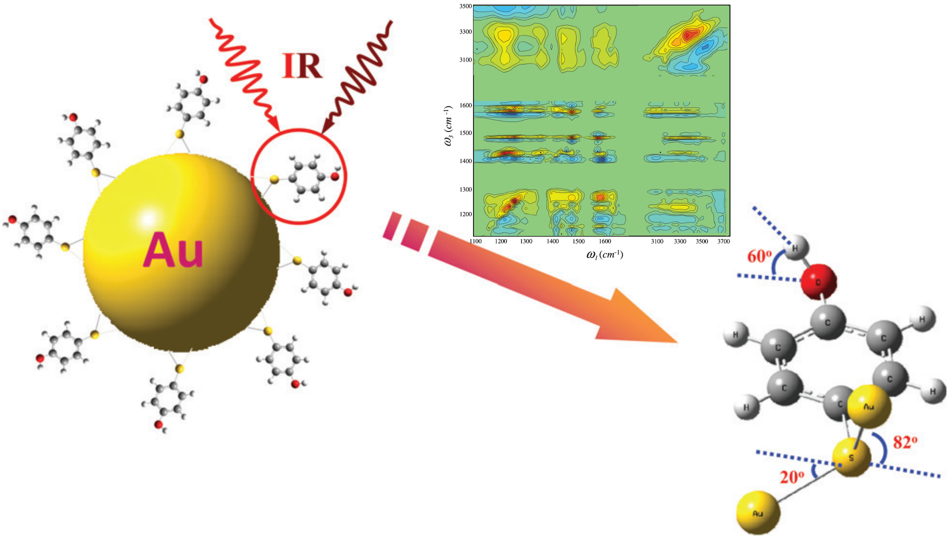

Figure 5.7. (Colour online) Molecular conformation and vibrational dynamics of 4-mercaptophenol on the 3.5 nm gold nanoparticle surface probed with multiple-mode multiple-dimensional infrared spectroscopy. Reprinted with permission from [91]. Copyright 2012 American Chemical Society.

The model system is 4-mercaptophenol (p-HO-C_6H_4-SH) on the surface of 3.5 nm gold nanoparticles. The molecule, 4-mercaptophenol, can form a surface monolayer through strong S-Au bonds with the particle substrate. This system is a prototype of molecular electronics in that this molecule has been considered as one of the best candidates for connecting a molecular wire to an electrode [194]. The theme of this work is illustrated in Figure 5.7 [91].

5.2.1. *Surface non-adiabatic electron/vibration coupling*

Figure 5.8(A) and (B) display the TEM image and the FTIR spectrum of the 3.5 ± 1 nm Au nanoparticles coated with 4-mercaptophenol [91]. The absence of the S-H vibrational mode ($2560\,cm^{-1}$) in the FTIR spectrum indicates that the ligand molecules have bound to the nanoparticles through the S-Au bonds [195,196]. The broad OH stretch peak ($3000 \sim 3600\,cm^{-1}$) indicates that the OH groups of surface molecules form hydrogen bonds with each other. However, further structural information, e.g. molecular conformations of the surface molecules is difficult to obtain from the peak positions in the FTIR spectrum, mainly because of Fermi resonances [65].

Figure 5.8(C) displays multiple-mode 2D IR spectra of 4-mercaptophenol on the surfaces of 3.5 nm Au nanoparticles. As introduced in previous section, the three-dimensional molecular conformations can be determined by measuring the angle between the transition electric dipoles of two vibrations through determining the off-diagonal peak intensities from experiments with parallel and perpendicular pump/probe polarisations (Figure 5.8(D)). By mapping a sufficiently big number of normal modes which cover the complete molecular space, the 3D molecular conformations can then be constructed by translating the measured vibrational angles into the cross angles among the chemical

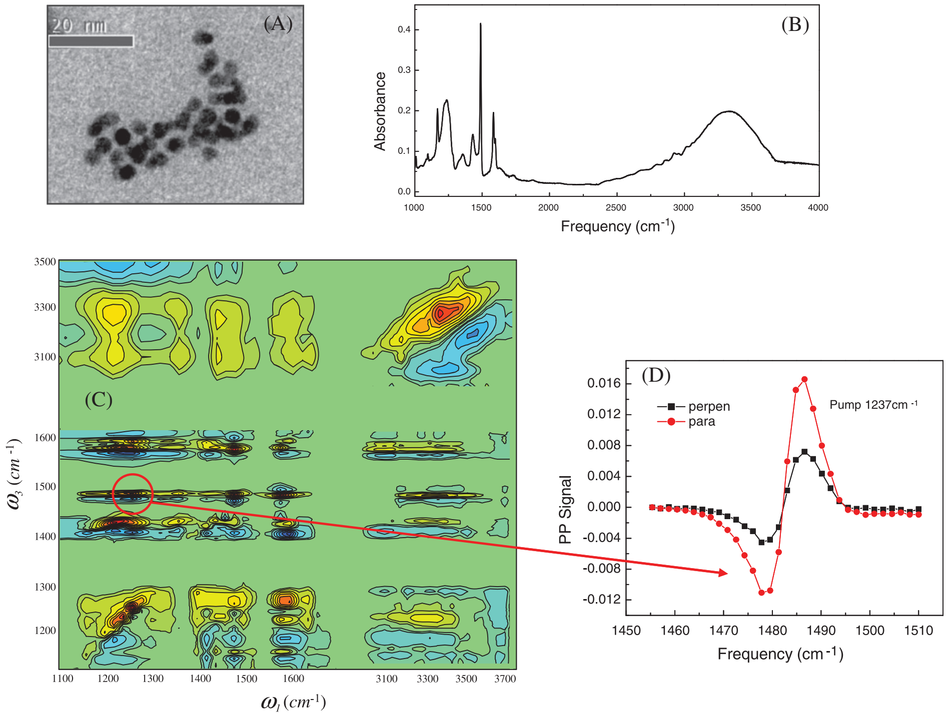

Figure 5.8. (Colour online) (A) TEM image of 3.5 ± 1 nm gold particles. (B) FTIR spectrum of 4-mercaptophenol on the Au nanoparticle surface. (C) Multiple-mode 2D IR spectra of 4-mercaptophenol on the surfaces of 3.5 nm Au nanoparticles. The relative intensities of peaks are adjusted to be comparable. (D) Perpendicular and parallel pump/probe data of a peak pumped at 1237 cm^{-1} and probed at 1450 ~ 1510 cm^{-1}. Reprinted with permission from [91]. Copyright 2012 American Chemical Society.

bonds with theoretical tools. However, the procedure described above can't be immediately applied to metal nanoparticles. The main reason is that it is too time-consuming and challenging to reliably calculate the 3.5 nm gold nanoparticles. A way to bypass this difficulty could be to reduce the number of gold atoms in the calculations if the vibrational properties of the surface molecules are not significantly affected by the surface electrons of the gold particles. However, this approach can fail if the assumption it is based on is invalid. In other words, the surface non-adiabatic electron/vibration coupling on the 3.5 nm Au nanoparticle surface can be very strong.

According to literature, 3.5 nm Au nanoparticles are already metallic [197–199]. There has been accumulating evidence that on some clean metal surfaces the metal surface electrons can be strongly coupled to the vibrations of surface molecules leading to the breakdown of the Born–Oppenheimer approximation (BOA) [200–202]. It is conceivable that a similar mechanism can also occur on surfaces of metallic nanoparticles. As a consequence, the electron-hole pair transitions between the continuum electronic levels in the conduction band can be strongly coupled to the nuclear motions of an adsorbate molecule and provide a relaxation mechanism for energy transfer from an adsorbate

Table 5.3. Vibrational lifetimes of major vibrational modes of 4-mercaptophenol in different environments. ** In CCl_4 solution, the central peak frequency is at $1280\,cm^{-1}$. In crystal and on nanoparticles, the frequency is at $1237\,cm^{-1}$. It is conceivable that the redshift is caused by an accidental degeneracy which also shortens the lifetime. Reprinted with permission from [91]. Copyright 2012 American Chemical Society.

Vibrational Mode	Nanoparticles	Crystal	In CCl_4
O–H stretch ($3340\,cm^{-1}$)	1.4 ± 0.3ps	1.8 ± 0.3ps	1.5 ± 0.2ps
C=C stretch ($1584\,cm^{-1}$)	4.2 ± 0.6ps	4.6 ± 0.6ps	4.2 ± 0.3ps
C–H bending ($1488\,cm^{-1}$)	2.6 ± 0.4ps	2.7 ± 0.4ps	2.4 ± 0.3ps
C–O stretch** ($1237\,cm^{-1}$)	1.0 ± 0.2ps	1.0 ± 0.2ps	4.0 ± 0.2ps
O–H bending ($1169\,cm^{-1}$)	1.3 ± 0.2ps	1.0 ± 0.2ps	1.4 ± 0.2ps

molecule and even call into question the applicability of the concept of motion evolving on a potential energy surface.

However, if the non-adiabatic electron/vibrational couplings are much weaker compared to the intramolecular vibrational couplings, it is then acceptable not to consider the non-adiabatic electron/vibrational couplings in the calculations, which means the calculations of converting the experimental vibrational angles into bond angles can be simplified by reducing the number of gold atoms.

To address this issue, we measured the vibrational lifetimes (the 1st vibrational excited state) of the O–H stretch, the O–H bending, the C=C stretch, the C–H bending, and the C–O stretch (surface distance > 3 Angstrom) on the 3.5 nm Au nanoparticle surface, in the pure 4-mercaptophenol crystal and in a 4-mercaptophenol/CCl_4 solution. As shown in Table 5.3 [91], except for the C–O stretch with the same, but substantially shortened (probably because of a Fermi resonance), lifetimes in the crystal and on the surface, the vibrational relaxations of those major vibrational modes of 4-mercaptophenol are actually the same for the three different cases.

These results show that about 3 Angstrom away from the particle surface, the surface non-adiabatic electron/vibration coupling, which can be an important channel for energy dissipations on metal surfaces, does not play a significant role in the vibrational relaxation of high frequency modes ($> 1000\,cm^{-1}$), i.e. the Born–Oppenheimer approximation holds for this circumstance. The conclusion is probably general, because most intramolecular vibrational relaxation occurs within a few or tens of ps and the transition dipole moment of a typical vibrational mode is similar to those of the modes measured here [101]. Furthermore, theoretical calculations show that the vibrational relaxation (hundreds of ps) induced by the surface non-adiabatic electron/vibration coupling is about two orders of magnitude slower than the measured values [91]. These results also suggest that it is acceptable to use BOA (omit the surface non-adiabatic electron/vibration couplings) in calculations to obtain the molecular conformations of 4-mercaptophenol on surfaces of the 3.5 nm Au nanoparticles.

5.2.2. *Translation from vibrational angles to molecular conformations*

On the surfaces of gold nanoparticles, the ligand thiol molecules are known to form covalent S-Au bonds with the particles [195,196]. In particular, the ligand molecules on a gold nanoparticle was recently found to be closely packed on the surface with coverage

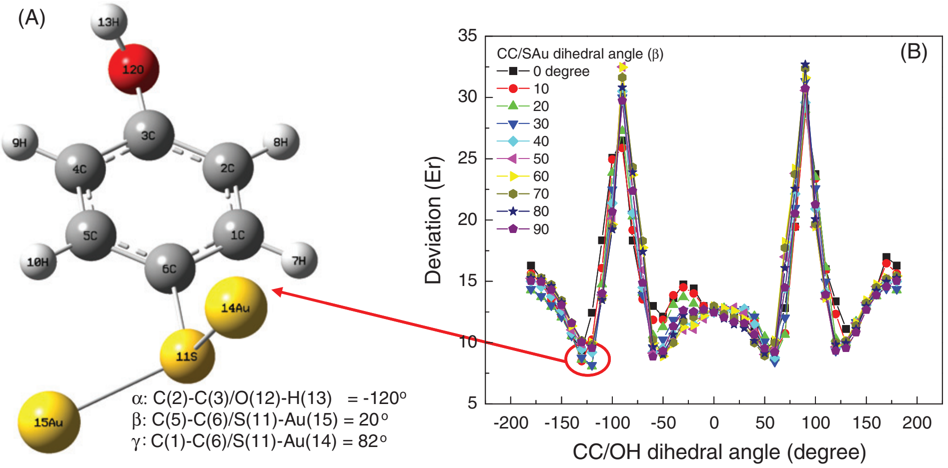

Figure 5.9. (Colour online) (A) The most probable conformation of HOC_6H_4-S$(Au)_2$ on the surface of 3.5 nm Au nanoparticle determined by experiments. α, β and γ are the dihedral angles as defined. (B) Experimental and calculated vibrational cross angle deviation E_r (defined in Equation(5.2)) vs the CC/OH dihedral angle C(2)-C(3)/O(12)-H(13) at different dihedral angles of C(5)-C(6)/S(11)-Au(15) (β) from 0 to 90 degrees. The calculation level used for the gold atom is B3LYP/LanL2DZ, and B3LYP/6-311++G(d,p) is for other atoms. E_r reaches the global minimum when $\alpha = -120^\circ$ and $\beta = 20^\circ$. Reprinted with permission from [91]. Copyright 2012 American Chemical Society.

around 70%, and all thiol molecules actually form two S-Au bonds with the particles in the bridge form [196], which inevitably impose geometric constraints on the intermolecular interactions of the ligand molecules and therefore affect their conformations. According to the above conclusions, we can simplify the calculations for vibrational cross angles by reducing the number of gold atoms of the nanoparticles into a cluster of two Au atoms.

The system HOC_6H_4-S$(Au)_2$ has two degrees of freedom to achieve the optimised structures, corresponding to the intermolecular interactions and surface bonding, respectively: (1) its O–H group can rotate to be in or out of the benzene plane; and (2) its C–S–$(Au)_2$ can also rotate to be in or out of the benzene ring. Experimentally we were able to determine both angles. We measured the vibrational cross angles among 16 pairs of normal modes of the surface 4-mercaptophenol molecules. These angles were then translated into molecular conformations with the same procedure as described above. The results (Figure 5.9) show that, on the nanoparticle surfaces the OH group is about 50 ~ 60 degrees out of the benzene plane, and one S–Au bond is ~ 20 degrees out of the benzene ring. The Au–S–Au angle was determined to be 110 degrees. With these angles determined, the most probable average three dimensional molecular conformation of 4-mercaptophenol on the 3.5 nm Au nanoparticles is readily constructed, shown in Figure 5.9(A) [91].

For comparisons, the molecular conformations of 4-mercaptophenol in a dilute CCl_4 solution and in its pure crystal were determined in a similar manner. In the dilute CCl_4 solution, the 4-mercaptophenol molecules are well separated from each other, indicated by a sharp free OH stretch peak (3610 cm^{-1}) in FTIR spectrum. Similar to the phenol molecule [203], the OH group of 4-mercaptophenol of the most stable conformation is expected to be coplanar to the benzene ring because of conjugation, as predicted by DFT

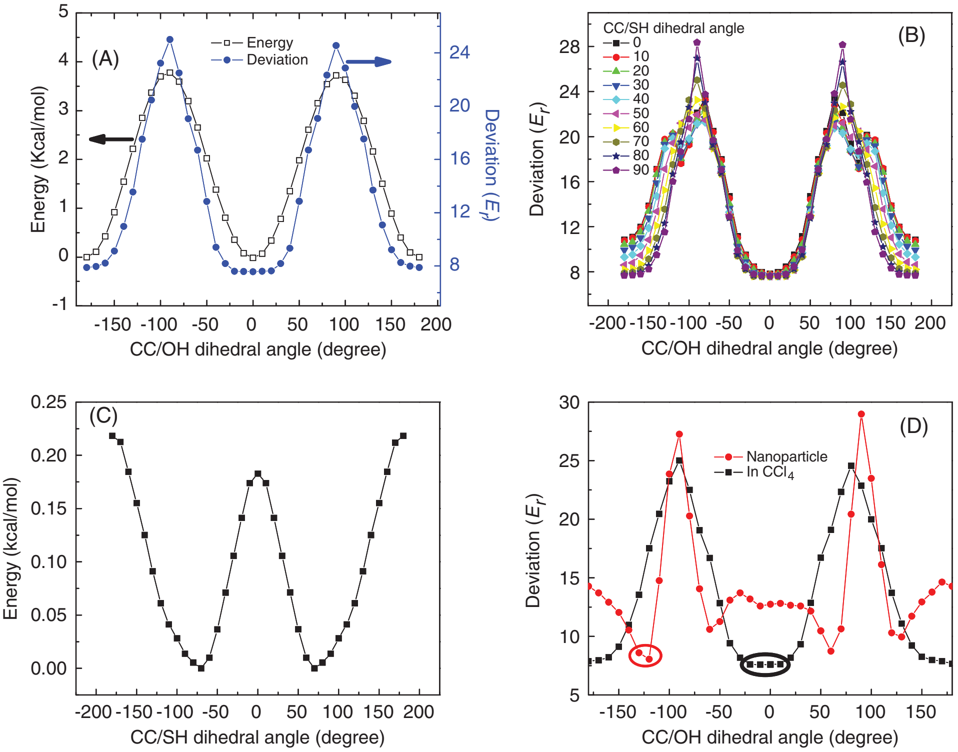

Figure 5.10. (Colour online) (A) Calculated potential energy surface of 4-mercaptophenol in CCl_4 (black) and the deviation between calculated and experimental vibrational cross angles E_r vs the CC/OH dihedral angle (blue), with a fixed dihedral angle of CC/SH at -72 degree (the calculated optimal angle). (B) Vibrational cross angle deviation E_r vs the CC/OH dihedral angle at different dihedral angles of CC/SH from 0 to 90 degrees. (C) The potential surface Vs the C–C/S–H dihedral angle at a fixed C–C/O–H dihedral angle 0 degree. (D) Vibrational cross angle deviations E_r vs the CC/OH dihedral angle of the CCl_4 solution sample and the nanoparticle sample with the optimised angles $\beta = 20^\circ$ and $\gamma = 82^\circ$. The circles highlight the optimised CC/OH dihedral angles. The DFT calculations for the liquid sample were performed using the CPCM model in CCl_4 with B3LYP/6-311++G(d,p). Reprinted with permission from [91]. Copyright 2012 American Chemical Society.

calculations in Figure 5.10(A) [91], which is very different from that on the Au nanoparticle surface. This theoretical anticipation is consistent with our experimental results from measuring the cross angles among 16 pairs of its vibrational modes in the solution (the E_r curve in Figure 5.10(A)). In the crystalline solid, the 4-mercaptophenol molecules are close to each other. Their OH groups are able to form hydrogen bonds with neighbor molecules, which distort the molecular conformation by dragging the OH group out of the benzene plane for only a few degrees, as XRD data of crystalline phenol show that the hydrogen bonds among phenol molecules on average distort the OH group ~5 degrees away from the benzene plane [204]. Our experimental results on the solid sample are also consistent with these results [91].

The distortion of the OH group about 50~60 degrees away from the conjugation plane of 4-mercaptophenol on the particle surface (Figure 5.10(D)) is attributed to the competing result of the surface geometric constraint, pi-pi stacking, and hydrophobic interactions on the formation of hydrogen bonds among the surface OH groups [72].

In an isolated 4-mercaptophenol in the CCl_4 solution, DFT calculations predict that the energy barrier for the S-H group rotating along the C-S bond is only ~ 0.22 kcal/mol (Figure 5.10(C)), indicating that the probability of the S-H group assuming any angle relative to the benzene ring is comparable at room temperature. Experimental data also support this prediction. As displayed in Figure 5.10(B), S-H rotating along the C-S for 90 degrees produces negligible change in E_r. Moreover, at any C-C/S-H dihedral angle, the O-H group is always coplanar to the benzene ring.

As demonstrated by the above experimental results and the analyses, it is feasible that 3D molecular structures and dynamics on the surfaces of nanomaterials, and in solids and liquids can be determined by the multiple-mode multiple-dimensional vibrational technique. Although the method is not interface specific, it can be utilised to analyse molecular structures and orientations on many buried interfaces or metal nanoparticles which are in general not accessible by the SFG method. The only requirement of the new approach, aside from enough transparency at the excitation and probe wavelengths to reach the interface, is that some interface specific physical properties must be able to influence the vibrations of molecules on the interface.

6. Concluding remarks and perspectives

MDVS is an emerging cutting-edge technique, which can provide chemical bond specific structural resolution as well as femtosecond temporal resolution to study structures and dynamics of various molecular systems. The basic concepts, experimental setups and applications of various MDVS methods are briefly introduced in this review. Some of the recent progresses achieved by our latest developed high power fs/ps hybridisation MDVS setup are introduced in more details.

Through mode-specific intermolecular vibrational energy transfer studies, we were able to develop an analytical Equation (3.6) to mathematically connect energy transfer kinetics with the average vibrational coupling strength and other molecular structural parameters. Combining the dipole/dipole interaction equation with Equation (3.6), we demonstrated that it is possible to determine molecular distances by measuring vibrational energy transfer kinetics. The vibrational energy transfer method was then applied to the studies of ion clustering, ion pairing, and ion/molecular interactions in strong electrolyte aqueous solutions.

Through measuring cross angles among vibrational modes covering the entire molecular space of a molecule, we demonstrated that 3D molecular conformations in liquids, solids and on interfaces can be determined by our method.

The work introduced in this review reveals the potential of our multiple-mode approach in resolving 3D molecular conformations with absolute chemical bond lengths. However, it is still a long way from this initial demonstration to the ultimate goal of a sophisticated yet routine analytic tool for determining molecular structures for chemists and researchers who are not laser specialists. In the way to this goal are many obstacles in both engineering and scientific aspects of the method. On the engineering side, due to the limits of IR detectors and the probe light frequency range, the acquisition of a multiple-dimensional full spectrum can be very slow. It can take days to obtain data like that shown in Figure 5.3 for a polyatomic molecule. In addition, it is difficult to cover frequencies below 400 cm^{-1} where many molecular conformation related vibration-rotational modes reside in. On the scientific side, many principles correlating molecular structures and experimental observables are still waiting for clarifications, e.g. how do vibrational excitations change the directions of vibrationally coupled transition dipole moments? How are intramolecular vibrational energy transfer rates dependent on the vibrational couplings, energy mismatches, and environments? How are vibrational couplings and energy dynamics corrected to the relative vibrational distances and orientations if the mechanism is other than the dipole/dipole interaction? What will be the theoretical basis and methods to reliably translate the experimentally determined vibrational coordinates into atomic coordinates under various conditions? We believe that with the progress of research, these issues will be resolved gradually.

Acknowledgements

This material is based upon work supported by the Air Force Office of Scientific Research under AFOSR Award No. FA9550-11-1-0070, and the Welch foundation under Award No. C-1752. J. R. Zheng also thanks the David and Lucile Packard Foundation for a Packard fellowship.

References

[1] P. Hamm, M. Lim, W. F. Degrado, and R. M. Hochstrasser, J. Chem. Phys. **112**, 1907 (2000).
[2] V. Cervetto, J. Helbing, J. Bredenbeck, and P. Hamm, J. Chem. Phys. **121**, 5935 (2004).
[3] S. Woutersen, Y. Mu, G. Stock, and P. Hamm, Chem. Phys. **266**, 137 (2001).
[4] J. Bredenbeck, J. Helbing, and P. Hamm, J. Am. Chem. Soc. **126**, 990 (2004).
[5] J. Bredenbeck, A. Ghosh, M. Smits, and M. Bonn, J. Am. Chem. Soc. **130**, 2152 (2008).
[6] C. Kolano, J. Helbing, M. Kozinski, W. Sander, and P. Hamm, Nature **444**, 469 (2006).
[7] Z. Ganim, H. S. Chung, A. W. Smith, L. P. Deflores, K. C. Jones, and A. Tokmakoff, Acc. Chem. Res. **41**, 432 (2008).
[8] M. Khalil, N. Demirdoven, and A. Tokmakoff, J. Phys. Chem. A. **107**, 5258 (2003).
[9] M. Khalil, N. Demirdoven, and A. Tokmakoff, Phys. Rev. Lett. **90**, 047401(4) (2003).
[10] O. Golonzka, M. Khalil, N. Demirdoven, and A. Tokmakoff, Phys. Rev. Lett. **86**, 2154 (2001).
[11] J. P. Wang, J. X. Chen, and R. M. Hochstrasser, J. Phys. Chem. B **110**, 7545 (2006).
[12] I. V. Rubtsov, K. Kumar, and R. M. Hochstrasser, Chem. Phys. Lett. **402**, 439 (2005).
[13] M. T. Zanni, S. Gnanakaran, J. Stenger, and R. M. Hochstrasser, J. Phys. Chem. B **105**, 6520 (2001).
[14] Y. S. Kim and R. M. Hochstrasser, Proc. Natl. Acad. Sci. **102**, 11185 (2005).
[15] M. C. Asplund, M. T. Zanni, and R. M. Hochstrasser, Proc. Natl. Acad. Sci. USA **97**, 8219 (2000).
[16] S. Mukamel, *Principles of Nonlinear Optical Spectroscopy* (Oxford University Press, New York, 1995).
[17] F. Sanda and S. Mukamel, J. Chem. Phys. **125**, 014507 (2006).
[18] Y. Tanimura and S. Mukamel, J. Chem. Phys. **99**, 9496 (1993).
[19] J. F. Cahoon, K. R. Sawyer, J. P. Schlegel, and C. B. Harris, Science **319**, 1820 (2008).
[20] H. Maekawa, F. Formaggio, C. Toniolo, and N. H. Ge, J. Am. Chem. Soc. **130**, 6556 (2008).
[21] J. Bredenbeck, J. Helbing, C. Kolano, and P. Hamm, Chem. Phys. Chem. **8**, 1747 (2007).
[22] S. H. Shim, D. B. Strasfeld, Y. L. Ling, and M. T. Zanni, Proc. Natl. Acad. Sci. U. S. A. **104**, 14197 (2007).

[23] M. L. Cowan, B. D. Bruner, N. Huse, J. R. Dwyer, B. Chugh, E. T. J. Nibbering, T. Elsaesser, and R. J. D. Miller, Nature **434**, 199 (2005).
[24] P. Mukherjee, I. Kass, I. Arkin, and M. T. Zanni, Proc. Natl. Acad. Sci. U. S. A. **103**, 3528 (2006).
[25] H. Maekawa, C. Toniolo, A. Moretto, Q. B. Broxterman, and N. H. Ge, J. Phys. Chem. B **110**, 5834 (2006).
[26] S. R. G. Naraharisetty, V. M. Kasyanenko, and I. V. Rubtsov, J. Chem. Phys. **128**, 104502 (2008).
[27] M. J. Nee, C. R. Baiz, J. M. Anna, R. McCanne, and K. J. Kubarych, J. Chem. Phys. **129**, 11 (2008).
[28] C. R. Baiz, M. J. Nee, R. McCanne, and K. J. Kubarych, Opt. Lett. **33**, 2533 (2008).
[29] L. W. Barbour, M. Hegadorn, and J. B. Asbury, J. Am. Chem. Soc. **129**, 15884 (2007).
[30] J. B. Asbury, T. Steinel, C. Stromberg, K. J. Gaffney, I. R. Piletic, A. Goun, and M. D. Fayer, Phys. Rev. Lett. **91**, 237402 (2003).
[31] J. Zheng, K. Kwak, and M. D. Fayer, Acc. Chem. Res. **40**, 75 (2007).
[32] J. R. Zheng and M. D. Fayer, J. Am. Chem. Soc **129**, 4328 (2007).
[33] J. Zheng, K. Kwac, J. Xie, and M. D. Fayer, Science **313**, 1951 (2006).
[34] J. Zheng, K. Kwak, J. B. Asbury, X. Chen, I. Piletic, and M. D. Fayer, Science **309**, 1338 (2005).
[35] W. Zhao and J. C. Wright, Phys. Rev. Lett. **84**, 1411 (2000).
[36] J. C. Wright, Int. Rev. Phys. Chem. **21**, 185 (2002).
[37] A. V. Pakoulev, M. A. Rickard, K. A. Meyer, K. Kornau, N. A. Mathew, D. E. Thompson, and J. C. Wright, J. Phys. Chem. A **110**, 3352 (2006).
[38] V. Cervetto, P. Hamm, and J. Helbing, J. Phys. Chem. B **112**, 8398 (2008).
[39] M. Kozinski, S. Garrett-Roe, and P. Hamm, J. Phys. Chem. B **112**, 7645 (2008).
[40] I. J. Finkelstein, J. R. Zheng, H. Ishikawa, S. Kim, K. Kwak, and M. D. Fayer, Phys. Chem. Chem. Phys. **9**, 1533 (2007).
[41] I. J. Finkelstein, H. Ishikawa, S. Kim, A. M. Massari, and M. D. Fayer, Proc. Natl. Acad. Sci. U. S. A. **104**, 2637 (2007).
[42] J. Treuffet, K. J. Kubarych, J. C. Lambry, E. Pilet, J. B. Masson, J. L. Martin, M. H. Vos, M. Joffre, and A. Alexandrou, Proc. Natl. Acad. Sci. U. S. A. **104**, 15705 (2007).
[43] H. Ishikawa, K. Kwak, J. K. Chung, S. Kim, and M. D. Fayer, Proc. Natl. Acad. Sci. U. S. A. **105**, 8619 (2008).
[44] M. F. DeCamp, L. DeFlores, J. M. McCracken, A. Tokmakoff, K. Kwac, and M. Cho, J. Phys. Chem. B. **109**, 11016 (2005).
[45] C. Fang, J. D. Bauman, K. Das, A. Remorino, E. Arnold, and R. M. Hochstrasser, Proc. Natl. Acad. Sci. U. S. A. **105**, 1472 (2008).
[46] P. Mukherjee, I. Kass, I. T. Arkin, and M. T. Zanni, J. Phys. Chem. B **110**, 24740 (2006).
[47] L. W. Barbour, M. Hegadorn, and J. B. Asbury, J. Phys. Chem. B **110**, 24281 (2006).
[48] M. Khalil, N. Demirdoven, and A. Tokmakoff, J. Chem. Phys. **121**, 362 (2004).
[49] J. Zheng, K. Kwak, T. Steinel, J. B. Asbury, X. Chen, J. Xie, and M. D. Fayer, J. Chem. Phys. **123**, 164301 (2005).
[50] S. R. G. Naraharisetty, V. M. Kasyanenko, and I. V. Rubtsov, J. Chem. Phys. **128**, 7 (2008).
[51] S. R. G. Naraharisetty, D. V. Kurochkin, and I. V. Rubtsov, Chem. Phys. Lett. **437**, 262 (2007).
[52] D. E. Moilanen, D. Wong, D. E. Rosenfeld, E. E. Fenn, and M. D. Fayer, Proc. Natl. Acad. Sci. U. S. A. **106**, 375 (2009).
[53] J. B. Asbury, T. Steinel, C. Stromberg, S. A. Corcelli, C. P. Lawrence, J. L. Skinner, and M. D. Fayer, J. Phys.Chem. A **108**, 1107 (2004).
[54] T. Steinel, J. B. Asbury, S. A. Corcelli, C. P. Lawrence, J. L. Skinner, and M. D. Fayer, Chem. Phys. Lett. **386**, 295 (2004).
[55] J. J. Loparo, S. T. Roberts, R. A. Nicodemus, and A. Tokmakoff, Chem. Phys. **341**, 218 (2007).
[56] J. J. Loparo, S. T. Roberts, and A. Tokmakoff, J. Chem. Phys. **125**, 12 (2006).

[57] C. J. Fecko, J. D. Eaves, J. J. Loparo, A. Tokmakoff, and P. L. Geissler, Science **301**, 1698 (2003).

[58] J. Zheng, K. Kwak, X. Chen, J. B. Asbury, and M. D. Fayer, J. Am. Chem. Soc **128**, 2977 (2006).

[59] J. Zheng and M. D. Fayer, J. Phys. Chem. B. **112**, 10221 (2008).

[60] Y. R. Shen, *The Principles of Nonlinear Optics* (John Wiley nd Sons, New York, 1984).

[61] P. Butcher and D. Cotter, The Elements of Nonlinear Optics, Vol. 9 of Cambridge Studies in Modern Optics (Cambridge University Press, Cambridge, UK, 1990).

[62] P. Hamm and M. Zanni, *Concepts and methods of 2D infrared spectroscopy* (Cambridge Univ Pr, Cambridge, UK, 2011).

[63] P. Hamm, *Principles of Nonlinear Optical Spectroscopy: A Practical Approach or: Mukamel for Dummies* (University of Zurich, Zurich, Switzerland, 2005).

[64] C. Lawrence and J. Skinner, The Journal of chemical physics **117**, 8847 (2002).

[65] E. B. Wilson Jr, J. C. Decius, and P. C. Cross, *Molecular Vibrations: The Theory of Infrared and Raman Vibrational Spectra* (McGraw-Hill, New York, 1955).

[66] H. J. Bakker and J. L. Skinner, Chem. Rev. **110**, 1498 (2010).

[67] P. Kukura, D. W. McCamant, S. Yoon, D. B. Wandschneider, and R. A. Mathies, Science **310**, 1006 (2005).

[68] Z. H. Wang, J. A. Carter, A. Lagutchev, Y. K. Koh, N. H. Seong, D. G. Cahill, and D. D. Dlott, Science **317**, 787 (2007).

[69] R. R. Ernst, G. Bodenhausen, and A. Wokaun, *Nuclear Magnetic Resonance in One and Two Dimensions* (Oxford University Press, Oxford, 1987).

[70] H. Bian, J. Li, X. Wen, and J. R. Zheng, J. Chem. Phys. **132**, 184505 (2010).

[71] P. Hamm, M. Lim, and R. M. Hochstrasser, J. Phys. Chem. B. **102**, 6123 (1998).

[72] H. Bian, J. Li, X. Wen, Z. Sun, J. Song, W. Zhuang, and J. Zheng, J. Phys. Chem. A **115**, 3357 (2011).

[73] M. C. Thielges and M. D. Fayer, J. Phys. Chem. A **115**, 9714 (2011).

[74] I. J. Finkelstein, B. L. McClain, and M. Fayer, The Journal of chemical physics **121**, 877 (2004).

[75] N. A. Mathew, L. A. Yurs, S. B. Block, A. V. Pakoulev, K. M. Kornau, E. L. Sibert III, and J. C. Wright, The Journal of Physical Chemistry A **114**, 817 (2009).

[76] N. A. Mathew, S. B. Block, L. A. Yurs, K. M. Kornau, A. V. Pakoulev, and J. C. Wright, The Journal of Physical Chemistry A **113**, 13562 (2009).

[77] S. Garrett-Roe and P. Hamm, J. Chem. Phys. **130**, 164510 (2009).

[78] W. Xiong, J. E. Laaser, R. D. Mehlenbacher, and M. T. Zanni, Proc. Natl. Acad. Sci. **108**, 20902 (2011).

[79] A. V. Pakoulev, M. A. Rickard, N. A. Mathew, K. M. Kornau, and J. C. Wright, J. Phys. Chem. A **112**, 6320 (2008).

[80] M. Richard, A. Pakoulev, K. Kornau, N. Mathew, and J. Wright, J. Phys. Chem. A. **110**, 11384 (2006).

[81] J. Zheng, *Ultrafast Chemical Exchange Spectroscopy* (VDM Verlag, Saarbrücken, Germany, 2008).

[82] J. B. Asbury, T. Steinel, and M. D. Fayer, J. Luminescence **107**, 271 (2004).

[83] J. Zheng, *Chemistry* (Stanford University, Stanford, 2007).

[84] J. D. Hybl, A. A. Ferro, and D. M. Jonas, J. Chem. Phys. **115**, 6606 (2001).

[85] L. P. DeFlores, R. A. Nicodemus, and A. Tokmakoff, Opt. Lett. **32**, 2966 (2007).

[86] S. H. Shim, D. B. Strasfeld, and M. T. Zanni, Opt. Express **14**, 13120 (2006).

[87] S. H. Shim, D. B. Strasfeld, E. C. Fulmer, and M. T. Zanni, Opt. Lett. **31**, 838 (2006).

[88] S. H. Shim and M. T. Zanni, Phys. Chem. Chem. Phys. **11**, 748 (2009).

[89] W. Xiong and M. T. Zanni, Opt. Lett. **33**, 1371 (2008).

[90] H. Bian, X. Wen, J. Li, H. Chen, S. Han, X. Sun, J. Song, W. Zhuang, and J. Zheng, Proc. Natl. Acad. Sci. **108**, 4737 (2011).

[91] H. Bian, J. Li, H. Chen, K. Yuan, X. Wen, Y. Li, Z. Sun, and J. Zheng, J. Phys. Chem. C **116**, 7913 (2012).

[92] J. B. Asbury, T. Steinel, and M. D. Fayer, Chem. Phys. Lett. **381**, 139 (2003).

[93] K. Kumar, L. E. Sinks, J. P. Wang, Y. S. Kim, and R. M. Hochstrasser, Chem. Phys. Lett. **432**, 122 (2006).

[94] O. Golonzka, M. Khalil, N. Demirdoven, and A. Tokmakoff, J. Chem. Phys. **115**, 10814 (2001).

[95] N. E. Levinger, P. H. Davis, P. Behera, D. J. Myers, C. Stromberg, and M. D. Fayer, J. Chem. Phys. **118**, 1312 (2003).

[96] H. T. Bian, X. W. Wen, J. B. Li, and J. R. Zheng, J. Chem. Phys. **133**, 034505 (2010).

[97] H. Bian, H. Chen, J. Li, X. Wen, and J. Zheng, J. Phys. Chem. A **115**, 11657 (2011).

[98] H. T. Bian, W. Zhao, and J. R. Zheng, J. Chem. Phys. **131**, 124501 (2009).

[99] H. J. Bakker, P. C. M. Planken, and A. Lagendijk, Nature **347**, 745 (1990).

[100] I. V. Rubtsov, Acc. Chem. Res. **42**, 1385 (2009).

[101] D. D. Dlott, Chem. Phys. **266**, 149 (2001).

[102] T. Steinel, J. B. Asbury, J. R. Zheng, and M. D. Fayer, J. Phys. Chem. A **108**, 10957 (2004).

[103] J. Lawkowicz, *Principles of Fluorescence Spectroscopy*, 3rd ed. (Springer, New York, 2006).

[104] V. Bernard, Molecular Fluorescence: Principles and Applications. (Wiley-VCH, Weinheim, Germany, 2002).

[105] R. Walser, B. Hess, A. E. Mark, and W. F. van Gunsteren, Chem. Phys. Lett. **334**, 337 (2001).

[106] S. Woutersen and H. J. Bakker, Nature **402**, 507 (1999).

[107] K. J. Gaffney, I. R. Piletic, and M. D. Fayer, J. Chem. Phys. **118**, 2270 (2003).

[108] T. Förster, Ann. Phys. Leipzig **2**, 55 (1948).

[109] C. B. Harris, D. E. Smith, and D. J. Russell, Chem. Rev. **90**, 481 (1990).

[110] A. H. Zewail, J. Phys. Chem. A **104**, 5660 (2000).

[111] C. G. Elles and F. F. Crim, Annu. Rev. Phys. Chem. **57**, 273 (2006).

[112] L. K. Iwaki and D. D. Dlott, J. Phys. Chem. A **104**, 9101 (2000).

[113] F. F. Crim, Proc. Natl. Acad. Sci. U. S. A. **105**, 12654 (2008).

[114] Z. H. Wang, A. Pakoulev, and D. D. Dlott, Science **296**, 2201 (2002).

[115] J. C. Deak, Y. Pang, T. D. Sechler, Z. Wang, and D. D. Dlott, Science **306**, 473 (2004).

[116] V. M. Kenkre, A. Tokmakoff, and M. D. Fayer, J. Chem. Phys. **101**, 10618 (1994).

[117] E. J. Heilweil, M. P. Casassa, R. R. Cavanagh, and J. C. Stephenson, J. Chem. Phys. **85**, 5004 (1986).

[118] E. J. Heilweil, R. R. Cavanagh, and J. C. Sephenson, J. Chem. Phys. **89**, 230 (1988).

[119] D. W. Miller and S. A. Adelman, Int. Rev. Phys. Chem. **13**, 359 (1994).

[120] A. Tokmakoff, B. Sauter, and M. D. Fayer, J. Chem. Phys. **100**, 9035 (1994).

[121] J. C. Deak, L. K. Iwaki, S. T. Rhea, and D. D. Dlott, J. Raman Spectrosc. **31**, 263 (2000).

[122] A. Ma and R. M. Stratt, J. Chem. Phys. **121**, 11217 (2004).

[123] P. B. Graham, K. J. M. Matus, and R. M. Stratt, J. Chem. Phys. **121**, 5348 (2004).

[124] H. Graener, R. Zurl, and M. Hofmann, J. Phys. Chem. B **101**, 1745 (1997).

[125] R. Rey and J. T. Hynes, J. Chem. Phys. **104**, 2356 (1996).

[126] G. Seifert, R. Zurl, T. Patzlaff, and H. Graener, J. Chem. Phys. **112**, 6349 (2000).

[127] M. Tuckerman and B. J. Berne, J. Chem. Phys. **98**, 7301 (1993).

[128] E. L. Sibert and R. Rey, J. Chem. Phys. **116**, 237 (2002).

[129] H. Fujisaki, K. Yagi, J. E. Straub, and G. Stock, Int. J. Quantum Chem. **109**, 2047 (2009).

[130] D. M. Leitner, Annu. Rev. Phys. Chem. **59**, 233 (2008).

[131] G. Hanna and E. Geva, J. Phys. Chem. B **112**, 15793 (2008).

[132] S. G. Ramesh and E. L. Sibert, J. Chem. Phys. **125**, 8 (2006).

[133] I. V. Rubtsov and R. M. Hochstrasser, J. Phys. Chem. B **106**, 9165 (2002).

[134] M. Schade, A. Moretto, M. Crisma, C. Toniolo, and P. Hamm, J. Phys. Chem. B **113**, 13393 (2009).

[135] V. M. Kasyanenko, Z. W. Lin, G. I. Rubtsov, J. P. Donahue, and I. V. Rubtsov, J. Chem. Phys. **131**, 12 (2009).

[136] D. V. Kurochkin, S. R. G. Naraharisetty, and I. V. Rubtsov, Proc. Natl. Acad. Sci. U. S. A. **104**, 14209 (2007).

[137] S. A. Adelman and R. H. Stote, J. Chem. Phys. **88**, 4397 (1988).

[138] S. A. Egorov and J. L. Skinner, J. Chem. Phys. **105**, 7047 (1996).

[139] P. Rogers, D. C. Montague, J. P. Frank, S. C. Tyler, and F. S. Rowland, Chem. Phys. Lett. **89**, 9 (1982).

[140] S. P. Wrigley and B. S. Rabinovitch, Chem. Phys. Lett. **98**, 386 (1983).

[141] R. A. Marcus, Faraday Discuss. **75**, 103 (1983).

[142] S. M. Arrivo and E. J. Heilweil, J. Phys. Chem. **100**, 11975 (1996).

[143] V. Lenchenkov, C. X. She, and T. Q. Lian, J. Phys. Chem. B **110**, 19990 (2006).

[144] M. J. Nee, R. McCanne, K. J. Kubarych, and M. Joffre, Opt. Lett. **32**, 713 (2007).

[145] R. M. Whitnell, K. R. Wilson, and J. T. Hynes, J. Chem. Phys. **96**, 5354 (1992).

[146] R. Rey and J. T. Hynes, J. Chem. Phys. **108**, 142 (1998).

[147] D. W. Oxtoby, Annu. Rev. Phys. Chem. **32**, 77 (1981).

[148] S. Z. Li, J. R. Schmidt, and J. L. Skinner, J. Chem. Phys. **125**, 8 (2006).

[149] S. Z. Li, J. R. Schmidt, S. A. Corcelli, C. P. Lawrence, and J. L. Skinner, J. Chem. Phys. **124**, 11 (2006).

[150] D. W. Oxtoby, Adv. Chem. Phys. **47**, 487 (1981).

[151] E. Merzbacher, *Quantum Mechanics*, 3rd ed. (John Wiley&Sons, Inc., New York, 1998).

[152] S. T. Roberts, J. J. Loparo, and A. Tokmakoff, J. Chem. Phys. **125**, 8 (2006).

[153] M. D. Fayer, *Ultrafast Infrared and Raman Spectroscopy* (Marcel Dekker, Inc, New York, Basel, 2001), Vol. 26.

[154] R. W. Gurney, *Ionic Processes in Solutions* (McGraw-Hill Book Company, Inc., New York, Toronto, London, 1953), International Chemical Series.

[155] B. E. Conway, *Ionic Hydration in Chemistry and Biophysics* (Elsevier Scientific Publishing Company, Amsterdam, Oxford, New York, 1981).

[156] R. M. Pytkowicz, *Activity Coefficients in Electrolyte Solutions* (CRC Press, Inc., Boca Raton, Florida, 1979), Vol. 1.

[157] J. M. G. Barthel, H. Krienke, and W. Kunz, Physical Chemistry of Electrolyte Solutions: Modern Aspects (Springer, New York, 1998), Vol. 5.

[158] D. Laage and J. T. Hynes, J. Phys. Chem. B **112**, 7697 (2008).

[159] A. C. Moskun, A. E. Jailaubekov, S. E. Bradforth, G. H. Tao, and R. M. Stratt, Science **311**, 1907 (2006).

[160] S. T. Roberts, P. B. Petersen, K. Ramasesha, A. Tokmakoff, I. S. Ufimtsev, and T. J. Martinez, Proc. Natl. Acad. Sci. U. S. A. **106**, 15154 (2009).

[161] Y. S. Lin, B. M. Auer, and J. L. Skinner, J. Chem. Phys. **131**, 144511 (2009).

[162] P. Debye and E. Huckel, Physikalische Zeitschrift **24**, 185 (1923).

[163] S. A. Hassan, J. Phys. Chem. B **112**, 10573 (2008).

[164] A. A. Chen and R. V. Pappu, J. Phys. Chem. B **111**, 6469 (2007).

[165] S. Petrucci, *Ionic Interactions from dilute solutions to fused salts* (Academic Press, New York and London, 1971), Vol. 1.

[166] W. J. Hamer, *The Structure of Electrolytic Solutions* (John Wiley & Sons, Inc., New York, 1959).

[167] P. W. Atkins, *Physical Chemistry*, 5th ed. (W.H. Freeman, New York, 1994).

[168] C. J. Fennell, A. Bizjak, V. Vlachy, and K. A. Dill, J. Phys. Chem. B **113**, 6782 (2009).

[169] M. Lund, B. Jagoda-Cwiklik, C. E. Woodward, R. Vacha, and P. Jungwirth, J. Phys. Chem. Lett. **1**, 300 (2010).

[170] J. Li, H. Bian, H. Chen, X. Wen, B. Hoang, and J. Zheng, J. Phys. Chem. B, accepted (2012).

[171] Y. J. Zhang and P. S. Cremer, Curr. Opin. Chem. Biol. **10**, 658 (2006).
[172] D. R. Robinson and W. P. Jencks, J. Am. Chem. Soc. **87**, 2470 (1965).
[173] J. N. Scott, N. V. Nucci, and J. M. Vanderkooi, J. Phys. Chem. A **112**, 10939 (2008).
[174] P. H. V. Hippel and K. Y. Wong, Biochemistry **1**, 664 (1962).
[175] C. Hamiaux, T. Prange, M. Ries-Kautt, A. Ducruix, S. Lafont, J. P. Astier, and S. Veesler, Acta Crystallogr. Sect. D-Biol. Crystallogr. **55**, 103 (1999).
[176] M. C. Vaney, I. Broutin, P. Retailleau, A. Douangamath, S. Lafont, C. Hamiaux, T. Prange, A. Ducruix, and M. Ries-Kautt, Acta Crystallogr. Sect. D-Biol. Crystallogr. **57**, 929 (2001).
[177] P. Chakrabarti, J. Mol. Biol. **234**, 463 (1993).
[178] W. L. Jorgensen, E. M. Duffy, and J. Tiradorives, Philos. Trans. R. Soc. Lond. Ser. A-Math. Phys. Eng. Sci. **345**, 87 (1993).
[179] P. E. Mason, J. W. Brady, G. W. Neilson, and C. E. Dempsey, Biophys. J. **93**, L4 (2007).
[180] J. Li, H. Bian, X. Wen, H. Chen, K. Yuan, and J. Zheng, J. Phys. Chem. B, accepted (2012).
[181] L. P. DeFlores, Z. Ganim, R. A. Nicodemus, and A. Tokmakoff, J. Am. Chem. Soc. **131**, 3385 (2009).
[182] S. Woutersen and P. Hamm, J. Phys. Chem. B **104**, 11316 (2000).
[183] S. Hahn, H. Lee, and M. Cho, J. Chem. Phys. **121**, 1849 (2004).
[184] C. B. Murray, C. R. Kagan, and M. G. Bawendi, Ann. Rev. Materials Sci. **30**, 545 (2000).
[185] S. G. Penn, L. He, and M. J. Natan, Curr. Opin. Chem. Biol. **7**, 609 (2003).
[186] A. T. Bell, Science **299**, 1688 (2003).
[187] S. J. Park, T. A. Taton, and C. A. Mirkin, Science **295**, 1503 (2002).
[188] R. A. Sperling, P. Rivera gil, F. Zhang, M. Zanella, and W. J. Parak, Chem. Soc. Rev. **37**, 1896 (2008).
[189] D. J. Maxwell, J. R. Taylor, and S. M. Nie, J. Am. Chem. Soc. **124**, 9606 (2002).
[190] P. Ghosh, G. Han, M. De, C. K. Kim, and V. M. Rotello, Adv. Drug Deliv. Rev. **60**, 1307 (2008).
[191] X. H. Huang, P. K. Jain, I. H. El-Sayed, and M. A. El-Sayed, Nanomedicine **2**, 681 (2007).
[192] N. Shukla, M. A. Bartel, and A. J. Gellman, J. Am. Chem. Soc. **132**, 8575 (2010).
[193] D. Pissuwan, S. M. Valenzuela, and M. B. Cortie, Trends Biotechnol. **24**, 62 (2006).
[194] Q. Jin, J. A. Rodriguez, C. Z. Li, Y. Darici, and N. J. Tao, Surf. Sci. **425**, 101 (1999).
[195] M. Brust, J. Fink, D. Bethell, D. J. Schiffrin, and C. Kiely, J. Chem. Soc.-Chem. Commun. 1655 (1995).
[196] P. D. Jadzinsky, G. Calero, C. J. Ackerson, D. A. Bushnell, and R. D. Kornberg, Science **318**, 430 (2007).
[197] M. C. Daniel and D. Astruc, Chem. Rev. **104**, 293 (2004).
[198] M. Valden, X. Lai, and D. W. Goodman, Science (Washington, D. C.) **281**, 1647 (1998).
[199] P. M. Paulus, A. Goossens, R. C. Thiel, A. M. van der Kraan, G. Schmid, and L. J. de Jongh, Physical Review B **64**, 18 (2001).
[200] N. H. Nahler, J. D. White, J. Larue, D. J. Auerbach, and A. M. Wodtke, Science **321**, 1191 (2008).
[201] A. M. Wodtke, D. Matsiev, and D. J. Auerbach, Prog. Surf. Sci. **83**, 167 (2008).
[202] S. Andersson and J. B. Pendry, Phys. Rev. Lett. **43**, 363 (1979).
[203] T. Pedersen, N. W. Larsen, and L. Nygaard, J. Mol. Struct. **4**, 59 (1969).
[204] V. E. Zavodnik, V. K. Belskii, and P. M. Zorkii, J. Struct. Chem. **28**, 793 (1987).